Internship at
The University of Texas at Arlington

31th July – 30th September 2017, Final Report

SUPERVISOR:

Dr. Prof. Luca Maddalena

UNIVERSITY OF TEXAS AT ARLINGTON

STUDENT:

Pasquale Walter Agostinelli

POLITECNICO DI MILANO

Acknowledgments

Index

Abstract

This report deals with the work done during the internship at the Aerodynamics Research Center of The University of Texas at Arlington. During this period three have been the main topics of research: the Filtered Rayleigh Scattering tool, the design of an emergency flange and the design of the test chamber windows for the new 1.6 MW Hypersonic Plasma Wind Tunnel, a two millions dollar facility at the moment under construction. First, each of the three topics is carefully described and a proper literature review is carried out. The studying of the Filtered Rayleigh Scattering led to several experiments that have been carried out for visualizing the supersonic mixing of vortices downstream the vorTX scramjet injector, developed at the Aerodynamics Research Center. For the other topics, instead, we present our proposed final design with the corresponding FEM analysis of the structures.

1.   Introduction

The Aerodynamics Research Center of The University of Texas at Arlington has an exceptional number of facilities to simulate and study a wide portion of flow conditions from subsonic to hypersonic velocities: a Low Speed Wind Tunnel, a Transonic Wind Tunnel, a Supersonic Wind Tunnel and a Hypersonic Shock Tunnel [1]. In addition to these, a new Hypersonic Plasma Wind Tunnel has been recently designed by the research group of Prof. Luca Maddalena and is under manufacturing process. This two million dollar project is supported by DARPA and it consist in a huge update of the actual 1.6 MW arcjet facility: no other public universities in the world has a hypersonic wind tunnel comparable to this in terms of dimensions and energy level, and it will be the only university-based, arc-heated, hypersonic-testing facility for thermal protection systems [2] (see Figure 1).
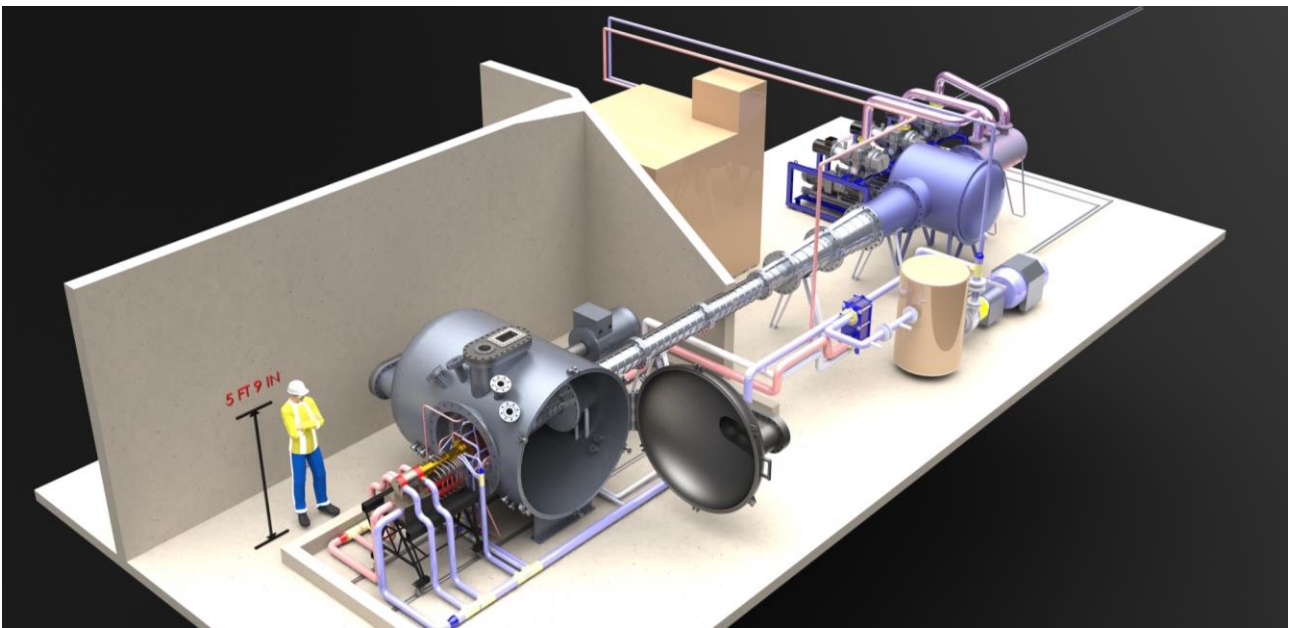

Figure 1: Rendering for the new arc-heated, hypersonic-testing facility for thermal protection systems from [2]

During the internship at the Aerodynamics Research Center (i.e. ARC) I have worked in the group of Prof. Luca Maddalena and I have been involved in some experiments using the Supersonic Wind Tunnel and in the last part of the design of the new Hypersonic Wind Tunnel.

The Supersonic Wind Tunnel at ARC is a blowdown type tunnel equipped with a variable Mach number nozzle with a current achievable Mach number from 1.5 to 4 and Reynolds numbers between 60 and 140 million per meter (Figure 2, left). The high pressure needed to run this facility is provided by a 5-stage Clark compressor (Figure 3, right) that was donated to UT Arlington from the NASA Ames Research Center and that provides a pressure of 2000 psi (i.e. 136 atm). The most common used configuration of the nozzle at Mach 2.5 allows a 45 seconds experiment with a total pressure in the plenum of about 320 psi.

This facility is actually used for doing experiments for studying the vortices mixing downstream of the scramjet injector developed at ARC and called VorTX. The scramjet (i.e supersonic combusting ramjet) is a variant of a ramjet airbreathing jet engine but, instead of decelerating the air to subsonic velocities before combustion, the airflow in a scramjet is supersonic throughout the entire engine, allowing the scramjet to operate efficiently at extremely high speeds. Design this kind of engine is highly challenging since, in the supersonic regime, the flow velocity is extremely high and it doesn't allow a stable combustion process to

exist: the solution to this problem is to create vortices in such a way to allow an efficient mixing of air and fuel in the engine. To study this process the scramjet injector is placed inside of the supersonic wind tunnel test section which has been designed with three large windows for optical access.

Figure 2: Supersonic Wind Tunnel (left) and Compressor (right) from [3, 4]

The two tools used at UTA (i.e. University of Texas at Arlington) to study the vortices mixing are the Filtered Rayleigh Scattering and the Particle Image Velocimetry that allow to visualize the flow field downstream the injector [4]. After a detailed literature review of the use of the Filtered Rayleigh Scattering technique and a studying of the LabView operation for the control of the facilities, I have been involved in the preparation and execution of this kind of experiments and in the processing of the obtained data.

The other task that I had was to design an emergency flange for the new Hypersonic Plasma Wind Tunnel. It will be a facility to simulate the conditions encountered by space vehicles re-entering the atmosphere and it has the classical structure of a plasma wind tunnel (Figure 3). Its characteristics are particularly suited to tests within development, selection and qualification projects of materials for high temperatures, new sensors and, generally, diagnostic techniques in the field of high temperatures. As a matter of fact, the hot flow is generated in a segmented arc heater and then the subsonic plasma flows to the convergent-divergent nozzle and it is accelerated to hypersonic speed to perform the experimental tests. Downstream the nozzle there is the test chamber and the plasma jet axis is transversal and displaced respect to the longitudinal axis of the chamber. After the interaction between the flow and the model surface, the plasma is then directed to the diffuser pick-up, that is a convergent duct connected to the test chamber through a large flange. The gas mixture flows into the diffuser throat and it ends its compression in the diffuser divergent. This last part has the same diameter of the heat exchanger which is downstream and allows to reduce the high temperature of the flow to lower values compatible with the vacuum system. The latter provides the proper suction power during the facility operation which is essential to ensure supersonic flow conditions at the nozzle exit.
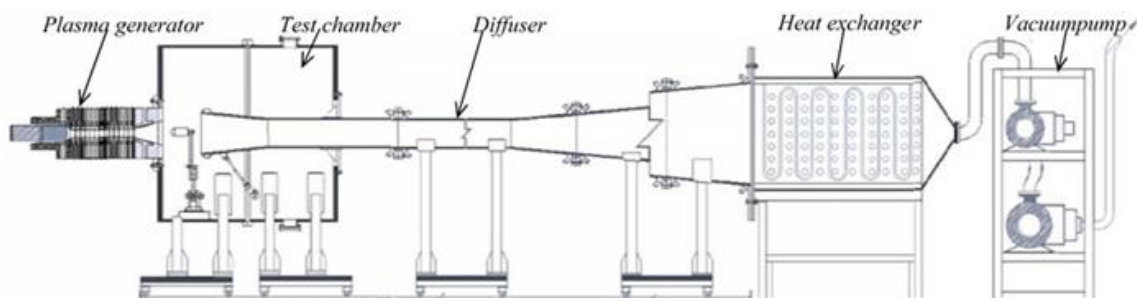

Figure 3: Scheme of a classic hypersonic plasma wind tunnel

The flange that I had to design is basically an emergency flange for water injection which has to be placed after the diffuser and before the heat exchanger. In practice, if it happens that the heat exchanger does not work properly we want to lower the temperature of the flow before it reaches the delicate and expensive vacuum system. The idea is to inject the right quantity of cold water in order to mix it with the flow and lower in such a way its temperature. As it will be presented, the design of such a flange is not straightforward at it may seem since we are injecting high pressure water in a very low ambient pressure with and we want good mixing properties with the incoming flow which has a temperature of thousands of degrees Celsius and a velocity of thousands of meters per second.

The last but not least objective that has been achieved is the design of the test chamber windows for the same hypersonic facility. This task is particularly problematic due to the material selection that we have to make in terms of used glass. In fact, we have not only strict requirements for what regarding the optical properties of the windows since we want to do different kind of measurements (from ultraviolet to infrared), but at the same time we have very challenging environmental properties, namely the high vacuum inside the test chamber (mechanical stress) and the hot air flowing in it which causes (temperature stress and chemical corrosive environment).

2.   Filtered Rayleigh Scattering

2.1.   Literature Review: theory

Before starting with the experimental staff, the first point was to deeply study the literature on the Laser Rayleigh Scattering [6] and its application as Filtered Rayleigh Scattering experiments for mixing studies [7, 8] and in particular for scramjet injectors [5].

This tool has been largely used by many scientists to determine density measurement (and Temperature if Pressure is known) of flow field by using the Intensity of the Rayleigh scattering (Dyer et al, 1979) or by using the spectrum of the Rayleigh scattering (e.g. atmospheric studies by Shimizu et al, 1983).

There exist other many tools to study complex flow field, such as the Particle Image Velocimetry (i.e. PIV) [9] and the Laser Doppler Velocimetry (i.e. LDV) [10]. The first one is an optical method of flow visualization used to obtain instantaneous velocity measurements and related properties in fluids. The fluid is seeded with tracer particles which, for sufficiently small particles, are assumed to faithfully follow the flow dynamics (the degree to which the particles faithfully follow the flow is represented by the Stokes number). The fluid with entrained particles is illuminated so that particles are visible. The motion of the seeding particles is used to calculate speed and direction (the velocity field) of the flow being studied. The scattered light from the particles is dominated by Mie scattering and so is also proportional to the square of the particles' diameters. Thus, the particle size needs to be balanced to scatter enough light to accurately visualize all particles within the laser sheet plane, but small enough to accurately follow the flow. The second one, instead, is the technique of using the Doppler shift in a laser beam to measure the velocity in transparent or semi-transparent fluid flows.

The key question now could be: why have we choose exactly the FRS to study this flow field properties and not one of the many other tools available?

The answer is hidden inside the so-called observer effect. This effect describes the fact that simply observing a situation or phenomenon necessarily changes that phenomenon. This is often the result of instruments that, by necessity, alter the state of what they measure in some manner. Historically, it has been confused with the uncertainty principle of Heisenberg, which notes that measurements of certain systems cannot be made without affecting the systems, that is, without changing something in a system. The confusion starts from the use of Heisenberg of such an observer effect at the quantum level as a physical "explanation" of quantum uncertainty for his uncertainty principle [11]. However, for what regards our previous question, the key fact is, at the end, that in PIV for example we are introducing some seeding particles which will certainly disturb the flow field somehow. In practice we are disturbing the flow properties that we want to measure while, with the FRS technique we can measure these properties without introducing any kind of disturbance in the flow field.

The theory behind the Filtered Rayleigh Scattering consist of the scattering properties of the particles. What happens when the atoms are illuminated by an electromagnetic wave with a wavelength much bigger than the atoms themselves is that the electrons of the atoms radiate like dipole antennas when they are forced to oscillate by the applied electromagnetic field (see Figure 4): the whole process is theoretically elastic. If the wavelength of the electromagnetic wave is of the same order of the atom or particle we are talking about Mie Scattering (used in PIV). The fact that the induced dipole moment is established almost instantaneously is then a very positive point because the response of the atoms is also instantons and we can get in this way instantaneous measurements of what is going on in our field.

Even if the mechanism associated with the scattering, induced electric dipole radiation, is conceptually straightforward, the features of the scattering are complex because of the anisotropy of molecules, collective

scattering from many molecules and inelastic scattering associated with rotational and vibrational transitions. These effects cause the scattered signal to be depolarized and to have spectral features that reflect the pressure, temperature and internal energy states of the gas [6].
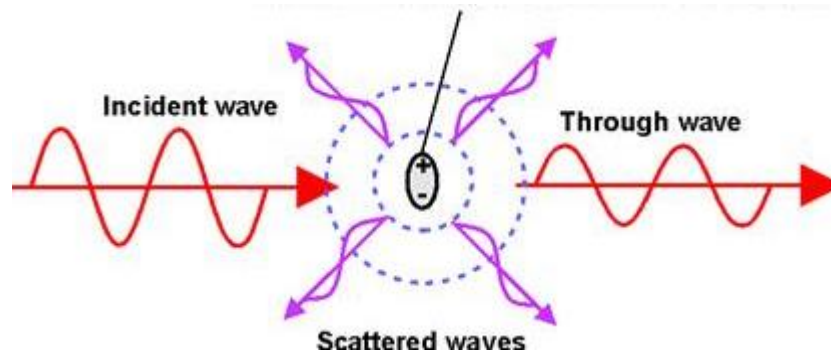

Figure 4: Scheme of the Rayleigh Scattering phenomenon

The properties of this radiation are simple if we assume in a stationary case a very high density of sources with uniform distribution (i.e. continuum assumption). In this case the radiation adds coherently in the forward direction and cancels in the others and what we get is the simply Ewald-Oseen solution which has as result that what we can actually see is only a change of the refracting index n for the propagating wave.

Instead, if we allow molecules to move we would have microscopic density fluctuations and what happens is that the radiation adds coherently in the forward direction and incoherently in the others: however, in the forward direction coherence is maintained since there is no momentum transfer. In reality, we have always some inelastic components in the process: the so called inelastic Raman scattering causes the Rayleigh scattering to be depolarized and partially dephased even in the forward direction.

We can have a better understanding of the components of the scattering by observing Figure 5 taken from [6] where we can see the frequency spectrum of the scattering components from laser illumination of N_2 molecules. At the top we can see the Vibrational Raman components which are associated to the change in the vibrational state of the molecules and in general are weak and very far from the central signal and usually we can simply neglect them (i.e. they represent the 0.1% of the total signal).

At the center we can see the Rotational Raman components which are associated to the change in the rotational state of the molecules: their disposition in the spectrum depends on the molecular mass that we are considering and, since each molecule has different bands, from these we can extract therefore the composition of the flow.

The last part is the Cabannes part which is very close to the central frequency that corresponds to the illuminating laser frequency: this part represents the elastic part of the phenomenon while the other two are inelastic components. It is composed by acoustic sidebands of Lorentzian shape (important in collision dominated conditions), by the Gaussian profile (thermally dominated) and by the elastic component of the rotational bands which is called Rotational Q-branch.

In order to model this complex phenomenon, we can rely, for a first approximation, on a spherically symmetric model. In fact, if the molecules are spherical, such as is the case for helium, argon and other noble gases, then there is no rotational Raman scattering, and at this point it's easy to calculate the Electromagnetic field of the scattering in terms of amplitude and intensity as in Figure 6 where ω is the oscillation frequency and p is the magnitude of the oscillating dipole moment (charge times displacement) induced by the incident field.
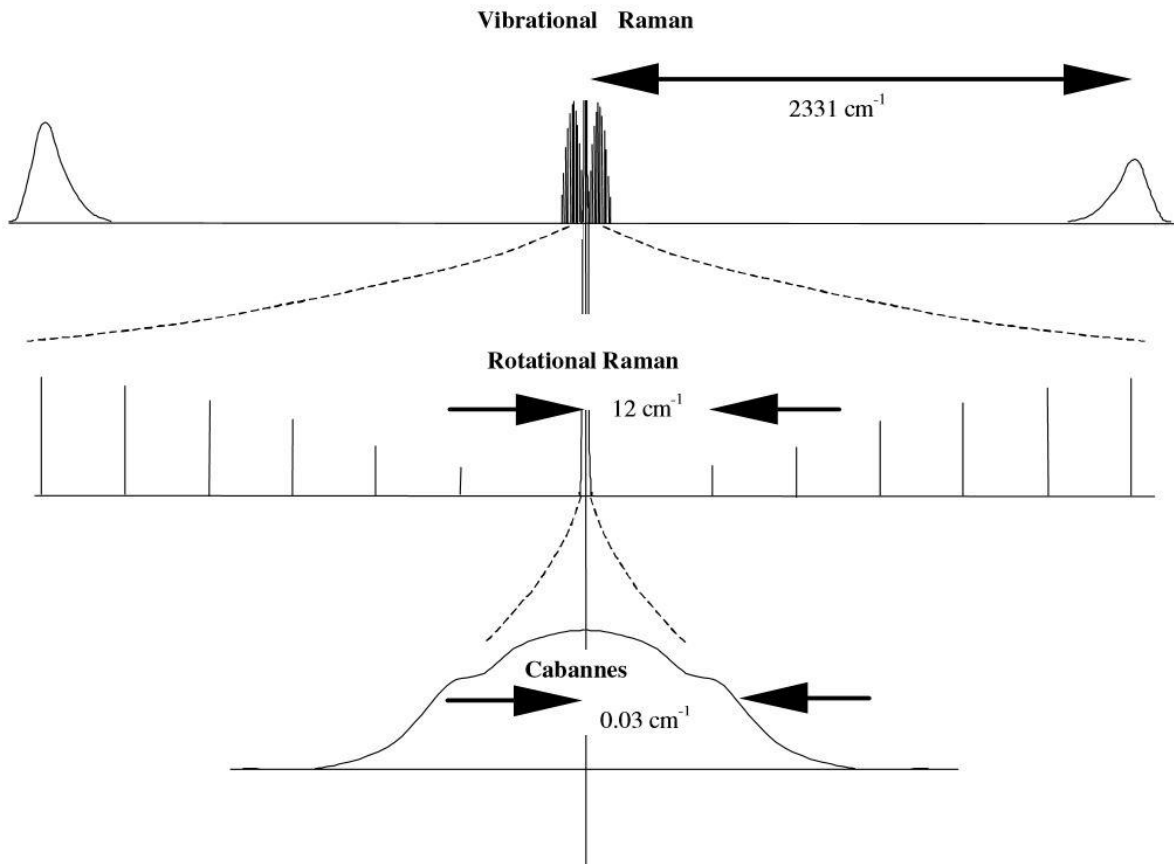
Vibrational Raman

2331 cm^{-1}

Rotational Raman

12 cm^{-1}

Cabannes

0.03 cm^{-1}

Figure 5: Scattering components from laser illumination of N2, frequency spectrum representation [6]

$$|\vec{E}_s(r, \phi)| = \frac{\omega^2 p \sin \phi}{4\pi r \varepsilon_0 c^2}$$

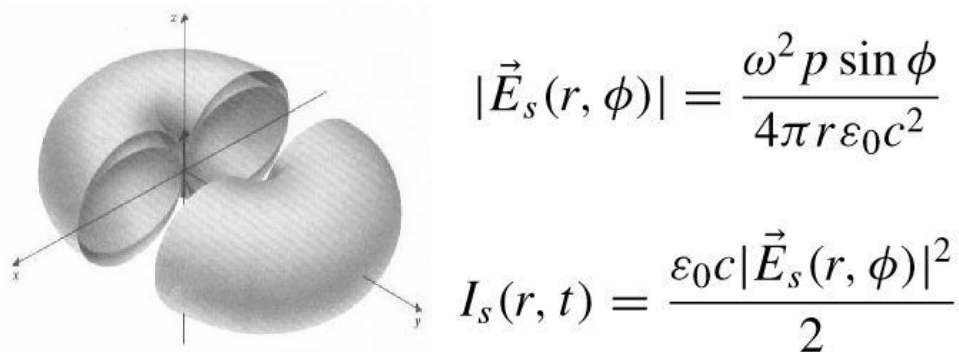$$I_s(r, t) = \frac{\varepsilon_0 c |\vec{E}_s(r, \phi)|^2}{2}$$

Figure 6: Polar diagram of electric (outer surface) and intensity (inner surface) field patterns around a dipole aligned with the z-axis (left) and expression for the amplitude and intensity of the (right) from [6]

The scattering geometry is shown in figure 7, where the dipole p is at an angle β to the vertical z-axis and φ is the angle of observation with respect to that dipole vector. The scattered electric field vector, E$_s$(r,φ), is perpendicular to the scattering propagation vector and lies in the plane of the dipole vector and the scattering propagation vector.
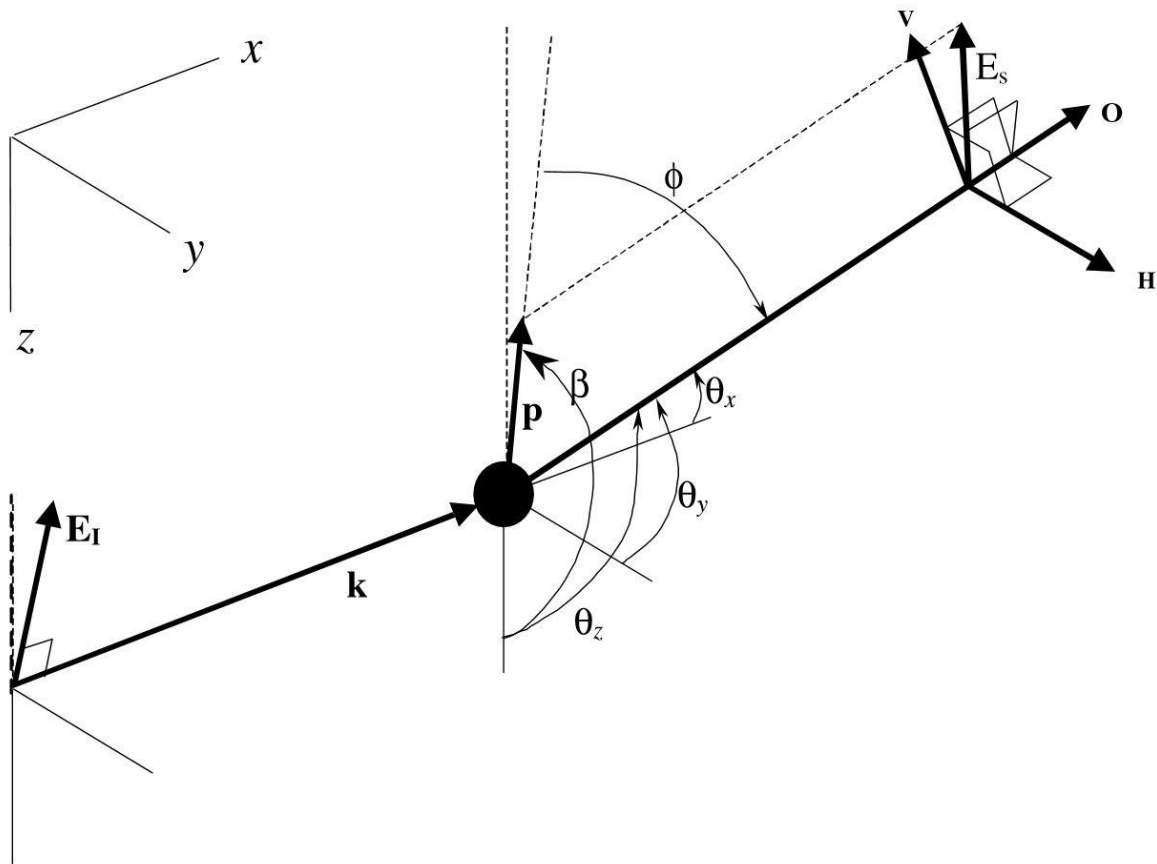
Figure 7: Rayleigh scattering geometry [6]

At this point, is interesting to combine the two equations if Figure 6 to obtain the expression of the scattering intensity as follows:

$$I_s = \frac{\pi^2 c p^2 \sin^2 \phi}{2\varepsilon_0 \lambda^4 r^2}$$

(1)

From equation 1 it's evident that the intensity of radiation of the scattering light is inversely proportional to the 4th power of the wavelength of the incident light. This is visible to us everyday since it is the reason for the blue color of the sky. The light coming from the sun isn't scattering by the atmosphere in the same way but the blue light (i.e. the visible light with shorter wavelength) is scattered more than the red light (i.e. visible light with longer wavelength) and this gives to the sky the classic blue color.

At this point, if we can express the dipole p through means the polarizability α as:

$$\vec{p} = \alpha \vec{E}_I$$

(2)

And if we express the polarizability as function of the index of refraction n (Lorentz-Lorenz equation) and if we integrate the intensity of radiation on a spherical surface we can obtain an expression for the total scattering power.

We can introduce the so called differential scattering cross section as:

$$I_s = \frac{\partial \sigma_{ss}}{\partial \Omega} \frac{1}{r^2} I_I$$

(3)

we obtain the following expression:

$$\frac{\partial \sigma_{ss}}{\partial \Omega} = \frac{\pi^2 \alpha^2}{\varepsilon_0^2 \lambda^4} \sin^2 \phi.$$

(4)

Let's define now the scattering cross section as the ratio between this total scattering power and the intensity of incident radiation:

$$\sigma_{ss} = \frac{P}{I_I}$$

(5)

this scattering cross section can be calculated as:

$$\sigma_{ss} = \frac{24\pi^3}{\lambda^4 N^2} \left(\frac{n^2 - 1}{n^2 + 2} \right)^2$$

(6)

This quantity is generally very small and therefore the scattering power is much smaller than the power of the incident light. This means that, if we want to measure this scattering light, we need both very sensible instruments and high-power incident light (i.e. laser). Again, we can see that this cross section varies with the 4th power of the wavelength of the incident light as we have discussed for the intensity of scattering radiation.

It's possible now to calculate the total power collected by considering each single molecule. For a single molecule we can express the scattering power as function of the differential scattering cross section:

$$\partial P = \frac{\partial \sigma_{ss}}{\partial \Omega} I_I \partial \Omega$$

(7)

In [6] the authors at this point simply calculate the total power collected by the optics by integrating the single scattering power of each molecule over the collection solid angle and summing together the contributes without explain the strong assumptions behind this simple passage. We pass from equation 7 to 8 by simply integrating over the collection solid angle $\Delta\Omega$ and by summing the different contributions: N is the number density of the molecule and V is the volume, while η is the efficiency of the optics.

$$P_{DET} = \eta I_I N V \int_{\Delta\Omega} \frac{\partial \sigma_{ss}}{\partial \Omega} \mathrm{d}\Omega.$$

(8)

Great effort has been posed during the internship to analyze this simple passage: it turned out that this is true only if all the molecules receive the same radiation I_I from the laser. The latter is theoretically not true: what happens if a molecule is hidden by another? And what happens if we consider the interference of the electric fields scattered by several molecules?

What we figured out is that usually the absorption coefficient of the flow is negligible and the laser passes through the molecules without being affected since only a small portion of that energy is «used» for the Rayleigh Scattering and is removed from the laser. This so-called single scattering assumption is acceptable until the optical depth of the medium is less than 0.1: if this is not true we may have the influence of the multiple scattering, for which each molecule feels the light scattered by the other molecules [12]. Then, the probability for a molecule to be hidden by another is very less and, in practice, it never happens that do molecules are aligned to the laser beam. Finally, the motion of the molecules randomizes the interference of the electric fields scattered from each individual molecule so that, when seen from afar, these coherent effects cancel and the total scattering becomes the sum of the individual intensities scattered from each molecule.

The case of diatomic molecules is more complex because the Raman rotational bands are now present, the Rayleigh scattering is therefore slightly depolarized and we need to apply an averaging for the random orientation of the molecules. As a matter of fact, what happens is that the dipole of the molecule is no more aligned with the incident electric field (i.e. the polarizability is not a simple scalar) but the polarizability becomes a tensor as in equation 9:

$$\bar{p} = \bar{\bar{\alpha}} \, \bar{E}_I \tag{9}$$

In practice we have dipole components along the three axes:

$$
\begin{aligned}
p_x &= \alpha_{xy} E_{Iy} + \alpha_{xz} E_{Iz} \\
p_y &= \alpha_{yy} E_{Iy} + \alpha_{yz} E_{Iz} \\
p_z &= \alpha_{zy} E_{Iy} + \alpha_{zz} E_{Iz}.
\end{aligned} \tag{10}
$$

Then, we can express the orientationally averaged polarizabilities in terms of the invariants of the polarizability tensor, namely the mean polarizability a and the anisotropy γ.

$$
\begin{aligned}
a^2 &= \tfrac{1}{9}(\alpha_{\underline{xx}} + \alpha_{\underline{yy}} + \alpha_{\underline{zz}})^2 \\
\gamma^2 &= \tfrac{1}{2}\{(\alpha_{\underline{xx}} - \alpha_{\underline{yy}})^2 + (\alpha_{\underline{yy}} - \alpha_{\underline{zz}})^2 + (\alpha_{\underline{zz}} - \alpha_{\underline{xx}})^2 \\
&\quad + 6(\alpha_{\underline{xy}}^2 + \alpha_{\underline{yz}}^2 + \alpha_{\underline{zx}}^2)\}
\end{aligned} \tag{11}
$$

The definition showed in equation 11 can be simplified in the case of diatomic and linear molecules for which there is for example cylindrical symmetry around the X axis. In this case it happens that the polarizability is the same with respect the Y and Z axes and the mean polarizability and the anisotropy become:

$$
\begin{aligned}
a^2 &= \tfrac{1}{9}(\alpha_{\underline{XX}} + 2\alpha_{\underline{YY}})^2 \\
\gamma^2 &= (\alpha_{\underline{XX}} - \alpha_{\underline{YY}})^2
\end{aligned} \tag{12}
$$

For what regarding the calculation of the total scattering cross section we expect to have the effect of these components. In fact, both if we consider a linearly polarized laser illumination (at an angle β) or if we consider an unpolarized incident light (averaging for the angle β from 0 to π) we get the expression for the total scattering cross section, as in equation 13.

$$\sigma = \left(\frac{8\pi^3}{3\varepsilon_0^2\lambda^4}\right)\left(\frac{45a^2 + 10\gamma^2}{45}\right) \tag{13}$$

As we were expecting, there is the anisotropy factor γ arising from the rotational Raman components. If we have again a spherically symmetric model (i.e. single atom) it is sufficient to set the γ equal to zero and, applying the Lorentz-Lorenz equation, we get exactly the same expression for the total scattering cross section that we have presented in equation 6.

If we let the diatomic molecules free to we get in the differential scattering cross section term of the form $\cos[2\pi(2\nu_R t)]$ where ν_R is the rotation frequency and we get the famous Rotational Raman scattering (incoherent). As we have shortly presented, this portion of the scattering can be divided in two parts on the base of the elasticity of the process. The elastic part of this rotational bands is the Q-branch which is unshifted in frequency since there isn't a change in the rotational state but only a reorientation of the molecule (i.e. elastic process). This Q-branch is the incoherent part of the Cabannes line (see Figure 5) while the coherent part is called Placzek trace scattering. The depolarization of the Cabannes line due to this Q-branch

component can be used to detect molecular concentrations in the presence of atomic species such as for measurements of molecules in plasmas. The inelastic part are the Stokes and anti-Stokes rotational branches spectrally shifted (central part of Figure 5). The frequency of diffused light is different from the incident; The frequency difference between incident and diffused light is the same as that associated with a rotational transition. An electronically diffused photon by a molecule can gain energy and therefore be diffused at a frequency higher than the original frequency (anti-Stokes), or it can lose energy and be diffused at a lower frequency (Stokes). In Figure 8 we schematize this difference.
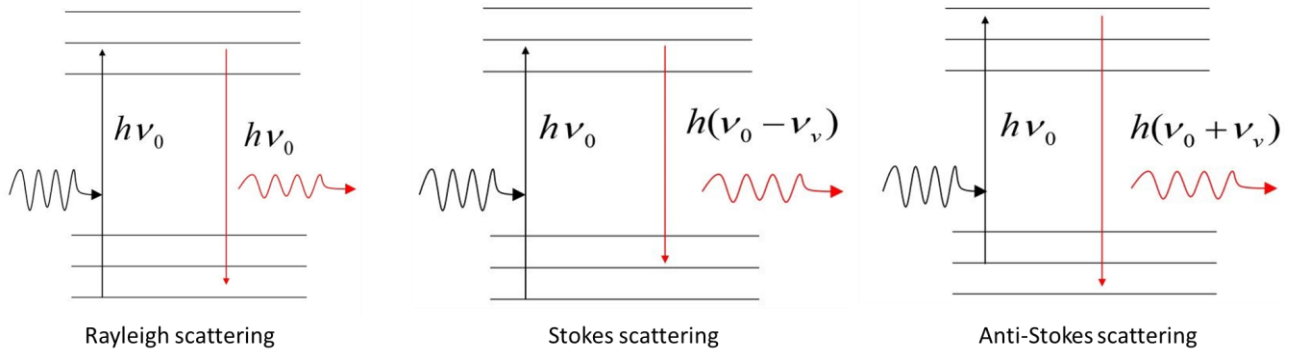

Figure 8: Scheme of the energy exchange for the elastic Rayleigh scattering and the Raman scattering (Stokes and anti-Stokes)

The frequency spectrum of the molecule scattering is then modified by the Doppler effect due to molecular motions. Non-moving molecules have a scattering frequency component at the same frequency as the incident laser and these two single frequency waves generate a stationary interference pattern (see Figure 9) with a spatial frequency in the direction of K given by:

$$\lambda_s = \frac{\lambda_L}{2} \frac{1}{\sin \theta / 2} \tag{14}$$

The results is that any stationary molecules or any molecules moving orthogonal to the K vector will scatter monochromatic light at the same frequency as the incident laser since there is no relative velocity along the K vector. Moreover, by analyzing the frequency spectrum one can extract a signal which is proportional to the number of molecules moving in each velocity interval (velocity parallel to K), see equation 15.

$$\Delta \nu = \frac{2v}{\lambda} \cos(\delta) \sin\left(\frac{\theta}{2}\right) \tag{15}$$
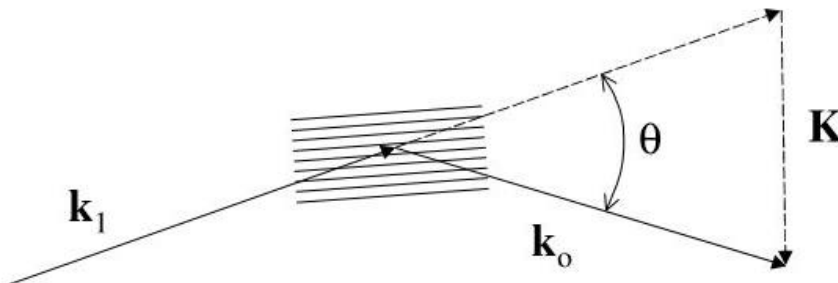

Figure 9: Scattering vector diagram. The incident wave vector is k_1 and the scattered wave vector propagating to the observer is k_0. These two vectors define an interference vector in the direction $K = k_0 - k_1$.

The spatial wavelength λ_s of the interference pattern is extremely important since it imposes a spatial scale on the scattering volume. If spatial structures of density variations in the sample volume are on the same

scale then they strongly contribute to the detected signal. The lineshape of the Cabannes line is therefore strongly affected by the value of this spatial scale and we can identify three main conditions:

- If the mean free path d is much larger than λ_s (i.e. the density is low and the temperature is high), we have a Symmetric Gaussian distribution and the scattering just reflects the motion of the molecules in the so-called Knudsen regime and we talk about Thermally broadened Rayleigh line.
- If the mean free path is of the same order of magnitude of λ_s, then the density fluctuations begin to contribute and the primary origin are the acoustic waves travelling in the gas. The density flucuations move at the speed of sound and acoustic sidebands appear: we talk about Brillouin-Mandel'shtam scattering.
- If the mean free path is much smaller than λ_s we are achieving the hydrodynamic limit (i.e. very high pressure) in which collision between molecules is the main process. We would have three peaks with Lorentzian shape: two acoustic side bands located at the frequency shift associated with the speed of sound and central peak associated with the thermal diffusion rate (ratio between central peak and other two is $\gamma-1$).

For what regarding the turbulent density fluctuations usually we are not able to see them because in optical regime the typical λs is too short compared to turbulence scale. However, in the infrared, particularly at small angles, the wavelengths can be much larger than the Kolmogorov scale, and turbulent density fluctuations can be primary contributors to the signal.

From the above discussion it's evident therefore that the main parameter that determines the lineshape of the Cabannes line (and therefore the frequency spectrum of the Rayleigh scattering) is the Knudsen number. For example, in the S6 Model by Tenti for diatomic gases, the determinant parameter is the y-parameter which is nothing else that the inverse of the Knudsen number as in equation 16.

$$ y \equiv \frac{\lambda_s}{2\pi \ell_m} \cong \frac{NkT}{\sqrt{2}|K|v_0\eta} \tag{16} $$

Using the Sutherland law for the viscosity [13] and the expression of the molecules velocity as function of the temperature, we can express this parameter as only function of the temperature, as in equation 17.

$$ y = 0.230 \left[\frac{T\,(\mathrm{K}) + 111}{T^2\,(\mathrm{K})} \right] \left[\frac{P\,(\mathrm{atm})\lambda\,(\mathrm{nm})}{\sin\theta/2} \right] \tag{17} $$

The application of the S6 Model by Tenti is showed in Figure 10, in which we plot the shape of the Cabannes part (Rayleigh–Brillouin) for different values of the y-parameter.

Notice that y <<1 means thermal regime Gaussian shape), while y >> 1 means hydrodynamic regime (two acoustic side and central peak associated with the thermal diffusion rate).
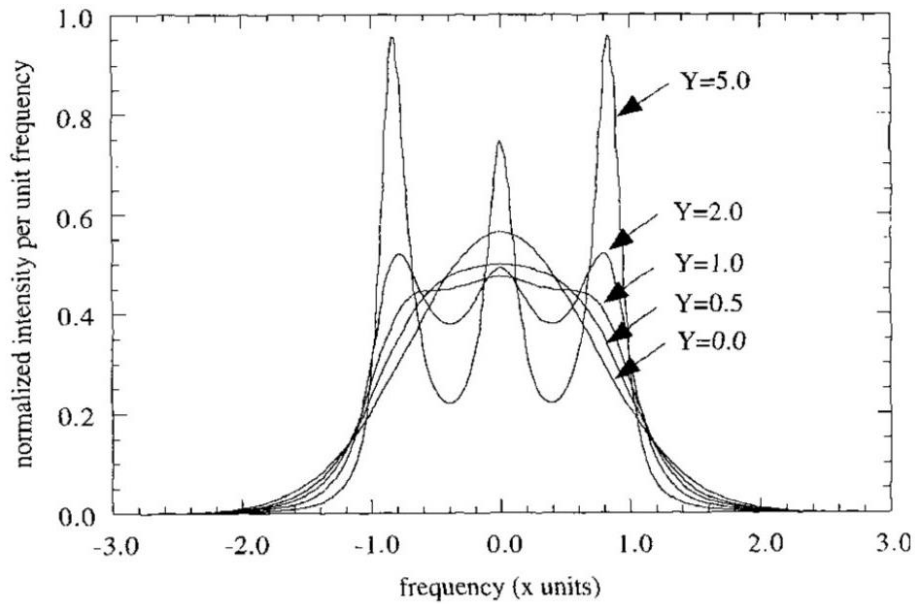
Figure 10: S6 Model; Rayleigh–Brillouin profiles for y-parameters ranging from 0 to 5.x is a normalized frequency parameter. The curves range from the kinetic regime (Boltzmann curve) to the hydrodynamic regime (triple peaked curve) [6]

2.2.   Applications in Literature

From the scattering signal we can get many flow properties; for example, it's easy to get density measurements in molecular gases. As a matter of fact, the signal is linearly proportional to the number of scatterers (i.e. the molecules). Usually we use Freon or ultraviolet laser to increase the scattering cross section (remember the inverse proportion between the intensity of scattered light and λ^4 of the incident light). An example of this measurement is showed in Figure 11 from [6].

Figure 11: Ultraviolet Rayleigh images of an overexpanded supersonic nitrogen jet. The left image is time averaged and the right image is instanteous. [6]

A common used technique is the spectral filtering of the Rayleigh light. The to main purposes of this technique are to eliminate the background light and to analyze the spectral properties to extract temperature and velocity information to identify the different spectral components of the signal. The velocity information can be taken from the frequency shift but it is usually small for molecules with respect to the thermal effect (i.e. for air 2.66 MHz/(ms) and the thermal line broadening is 1.83GHz). Therefore, to get velocity we need

the scattering light from nanoparticles since, in this case, the thermal line broadening is much smaller (i.e. they have higher mass). For the temperature information we look instead at the spectral linewidth.

Two main tools capable of GHz or better resolution for resolving the spectrum and they can be based on:

- Resonance features associated with atoms or molecules
- Interferance phenomena (Fabry – Perot etalon)

The first one requires the use of Atomic and molecular filters (as we did at UTA): a cell is filled with an atomic or molecular gas with a pressure, temperature and cell length chosen so very strong absorption occurs at an atomic or molecular resonance to suppress background scattering.

The second one uses the Fabry-Perot interferometer showed in Figure 12. In practice, light passes if d is an integral number of half wavelength (normal component) and, in this way, only the light from the selected frequency forms the image on the image plane.
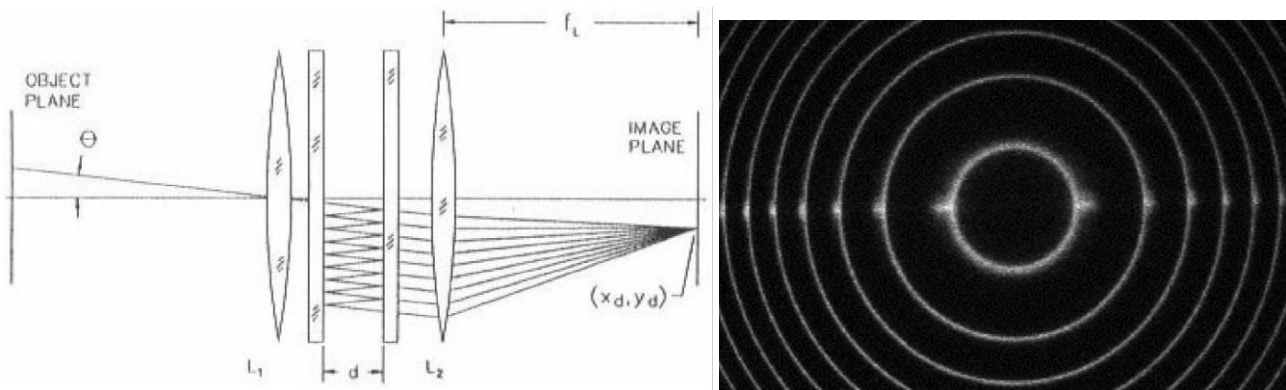

Figure 12: Scheme of the Fabry-Perot interferometer (left) and planar image of a supersonic jet (right) from [6]

An example of application of this interferometer is showed in Figure 12 right. The thickness of the rings can be used to derive the Temperature while if there is an average velocity the local position of the ring on the image is shifted.

Another important application is the use of nanoparticles to get especially, as we have said, velocity information. The polarizability of this particles is dependent on the volume of the particle itself. Therefore, the differential scattering cross section would be dependent on the second power of the volume, that is the six power of the radius (see equation 18).

$$\frac{\partial \sigma}{\partial \Omega} = \frac{9\pi^2 V^2}{\lambda^4} \left(\frac{n^2 - 1}{n^2 + 2} \right)^2 \sin^2 \phi \qquad (18)$$

This extremely high dependence on the particle radius can be a vantage or also a drawback, for example if part of the gas that we want to study condenses, the scattering from these particles can easily obscure the scattering from molecules.

This effect of the condensation can be used also to visualize the shockwaves, as for example in Figure 13. There we present Rayleigh images from [6] of shock wave boundary layer interactions taken in a Mach 2.5 flow. Flow is from left to right and the scattering is from 10 nm scale CO_2 clusters, which condense in the cold portion of the flow, but not in the warmer portions corresponding to the boundary layers and behind strong shocks.
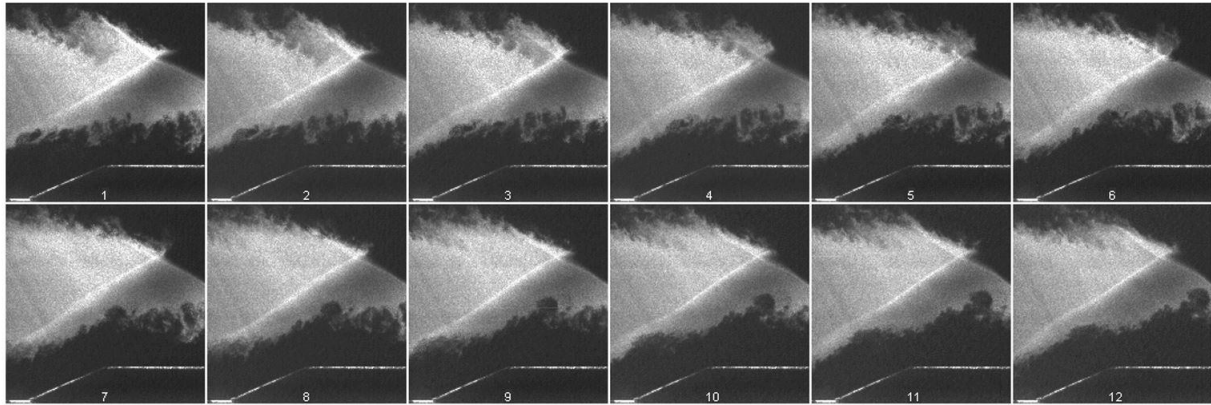
Figure 13: Rayleigh images of shock wave boundary layer interactions taken in a Mach 2.5 from [6]

The principal property of the scattering from nanoparticles is that, since their mass is much higher if compared to the molecules, the thermal motion of the particles is substantially reduced, and this allows us to extract velocity information from the Rayleigh scattering since the particles do travel with the flow. Instead the temperature cannot be measured as it can be with molecules since the mass of the individual particles is not known with sufficient accuracy.

The higher mass of the particles gives also another important characteristic: the light scattered from the particles is significantly more coherent than that scattered from molecules, and this gives interference phenomena, or speckle, at the image plane. The coherence time is in fact inversely proportional to the thermal linewidth: for the molecules the thermal linewidth is of the order of GHz (i.e. coherence time of ns), while for the particles the thermal linewidth is of the order of MHz, leading to a coherence time of 100 ns. This time is sufficiently high to lead the interference pattern to not average out during the laser pulse time: speckle is observed.
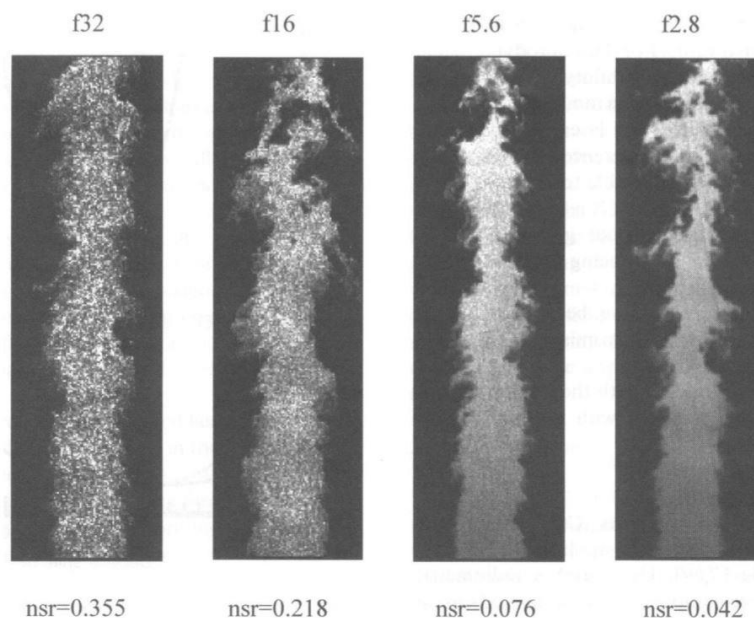

Figure 14: Image of Rayleigh scattering from water and CO_2 particles condensed in a Mach 1.36 air jet showing speckle effects for different camera f-stop settings from [6]

In Figure 14 we can appreciate how the spatial frequency of the speckle pattern changes by changing the focal ratio of the camera: with high f we have small collection aperture and we have extremely speckled

image (left), with low f (i.e. increasing the collection aperture) we are reducing the spatial frequency of the speckle pattern and it becomes too small for the resolution scale (right).

Another important application is the so called Planar Doppler velocimetry which uses the Rayleigh scattering from condensed particles and molecular filter to measure the velocity. In a supersonic flow in fact, the temperature drops rapidly through the expansion nozzle and these seed gases at concentrations on the order of 1% condense into nanoscale particulate fogs, which are observed as they pass through the test section. In Figure 15 there is an example of the application of this procedure which show the velocity field near the trailing edge of a a 70◦ swept delta wing at a 23◦ angle of attack.
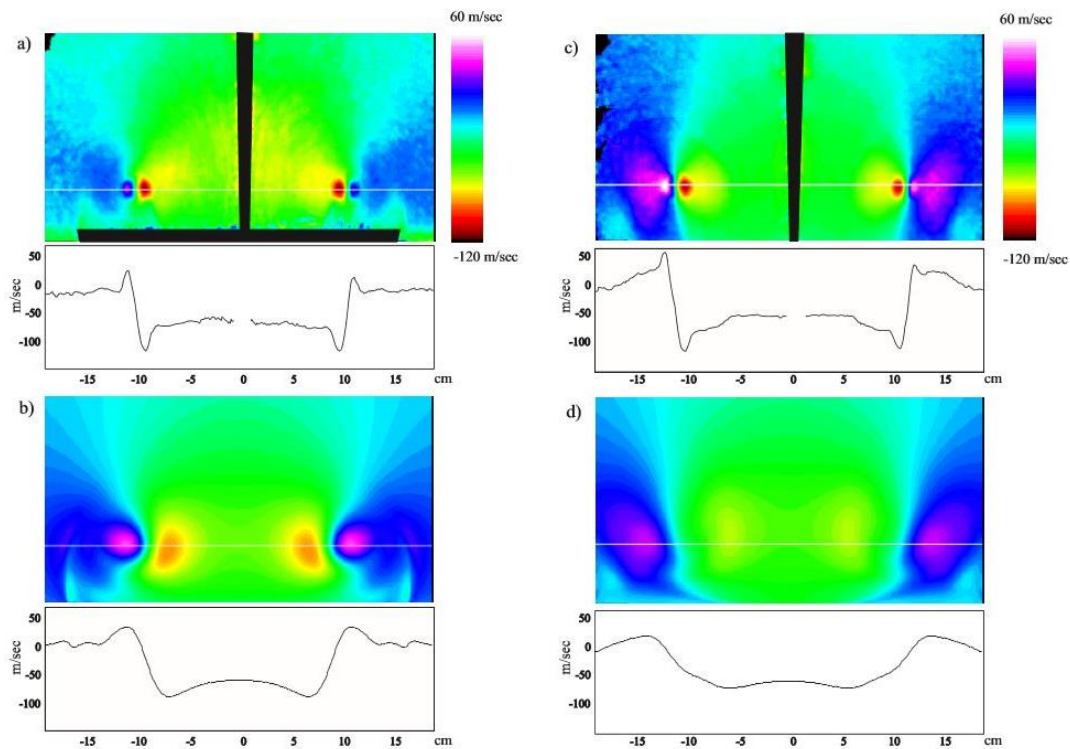
Figure 15: Measured velocity field (upper images) over a delta wing at 97% of root chord (a) and 114% of the root chord (b) compared to computed results (lower images) from [6]

2.3. Preparing to experiments: LabView

After the detailed literature review summed up in the previous paragraphs, and before getting involved in the real experiments, I had to do some trains in using the LabVIEW program [14]. Laboratory Virtual Instrument Engineering Workbench (LabVIEW) is a system-design platform and development environment for a visual programming language from National Instruments. It is commonly used for data acquisition and instrument control: it provides the "link" between the sensors and the actuators and the control computers. The principal feature of this platform is the graphical programming: we can set up the link between the sensors/actuators and the computer by simply create graphically our program, i.e. painting the arrows, link the different blocks and so on. A simple example of the way in which the graphical programming is performed in LabView is showed in Figure 16. Here we have done a program that transform the temperature in Fahrenheit scale (blue bar) in Celsius scale (red bar). On the right there is the block diagram which is the ambient in which the program is built.
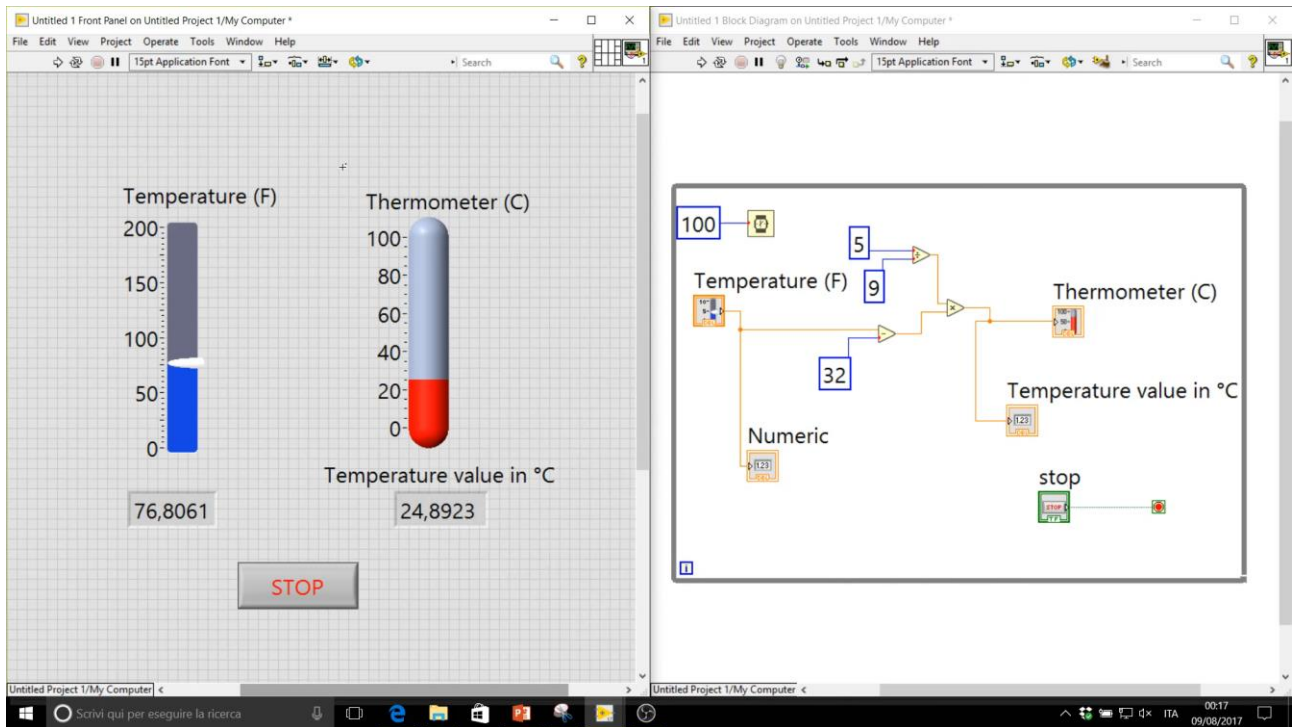
Figure 16: Example of graphical programming in LabView

The next step in using the LabView ambient is the acquisition of data from instruments. We have performed the acquisition of two types of data: the temperature and the pressure data.

In order to acquire the temperature data, we have used a Thermocouple type T and a NI – USB 6009. The first one is a classical thermocouple with copper and copper–nickel alloy [15]. It uses the Seebeck effect for which in a circuit formed by two types of conductors, if there is a temperature gradient, a potential difference is formed. From the type of metal used and from the potential difference which is formed, it's possible to derive the temperature value. The NI-USB 6009 is a multifunction DAQ (Data Acquisition) device that provides basic functionality for applications such as simple data logging, portable measurements, and academic lab experiments [16].

In Figure 17 we show the measurement done with these instruments: we can see how the measured data are quite noisy, i.e. we have a lot of oscillations around the average value. This issue can be caused in principle by the interference with the electric system of the building (which runs at 60 Hz) or because of the poor quality of the DAQ device used. To check these hypothesis, we may perform a spectral analysis of the received signal and check if the signal has a peak at 60 Hz.

In Figure 18, we present the spectral analysis applied at the acquired temperature data. It's easily visible how the oscillations seen are caused by white noise (i.e. uniform noise for all the frequencies). This demonstrates how the NI-USB 6009 device used is only an "academic" device and do not allow to perform sensible and accurate measurements, at least with this type of thermocouple.

In order to acquire the pressure data, we have used instead the same NI – USB 6009 DAQ device with an Omega PX603 Transducer [15]. This type of transducer needs to be alimented by a power supply and provides a voltage measurement which corresponds to a gauge pressure. In theory the output voltage is linearly linked to the pressure difference and the slope of the line is given in the manual of the transducer. In Figure 19 we present the measurement of the pressure that we have obtained. This instrument appears to be very precise and noiseless if compared to the temperature data that we have obtained before.
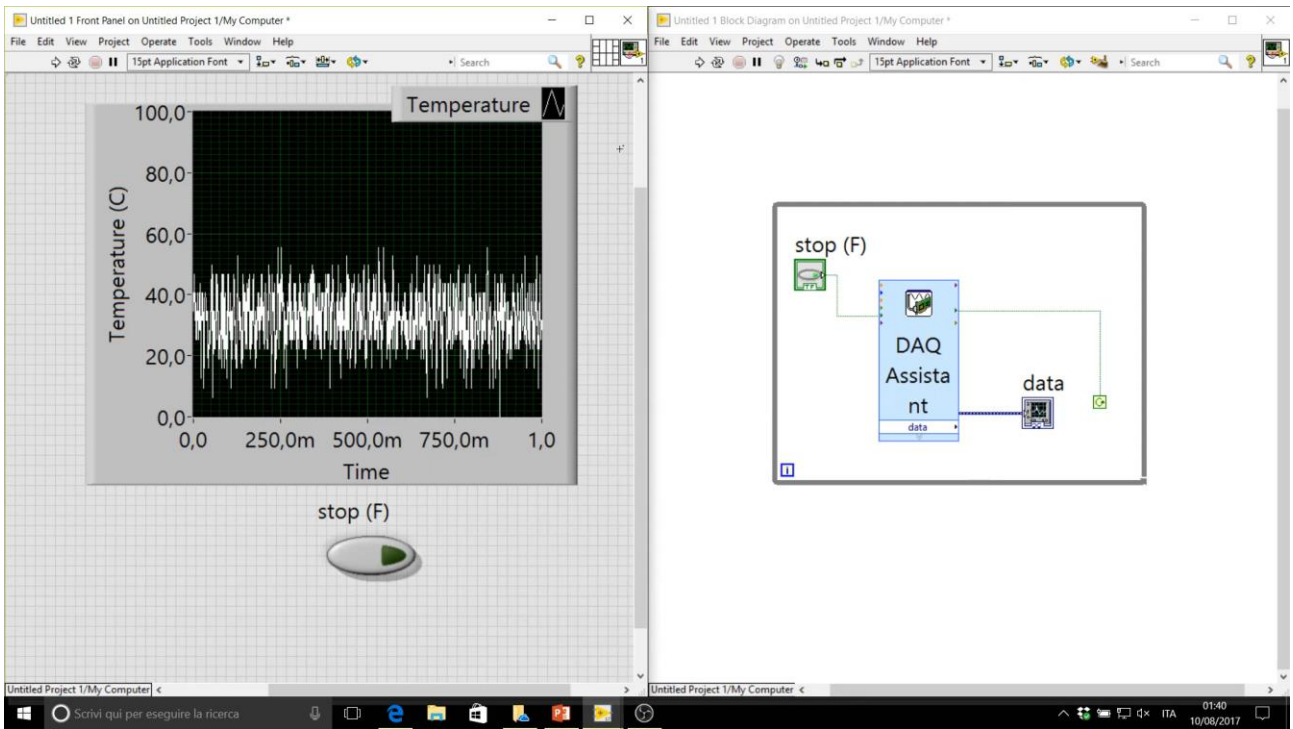
Figure 17: Temperature data acquisition using a T-Thermocouple and the NI-USB 6009 DAQ device.
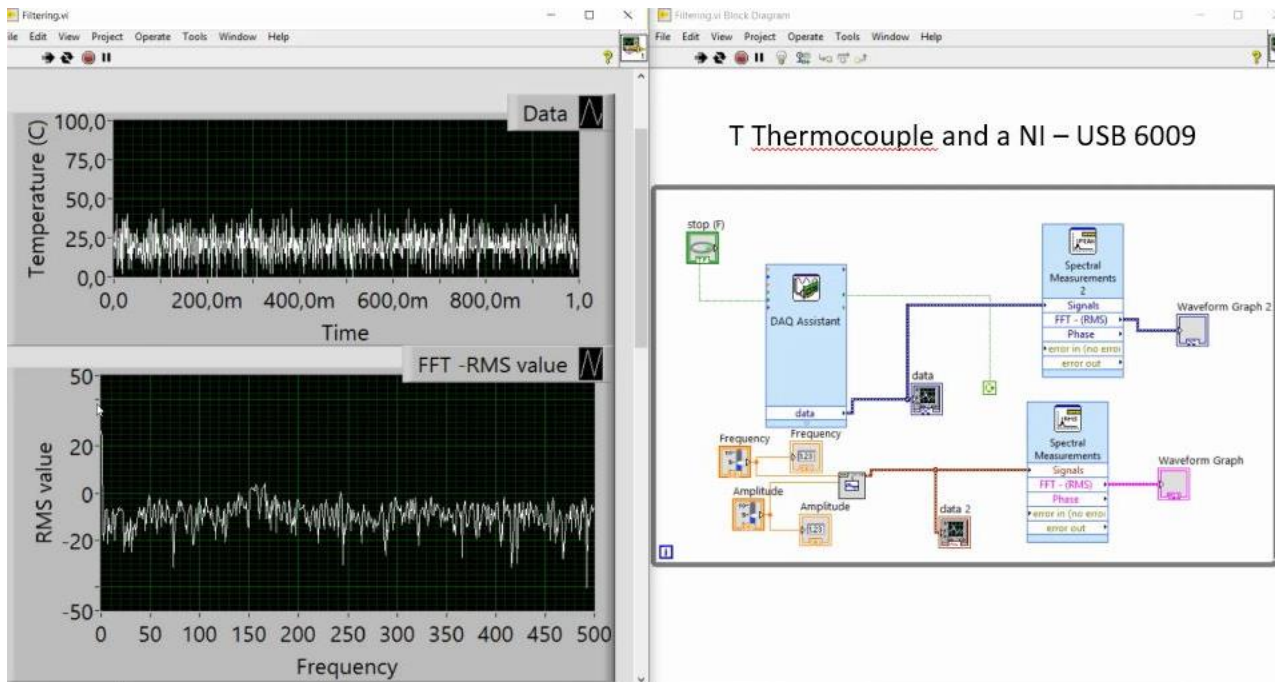

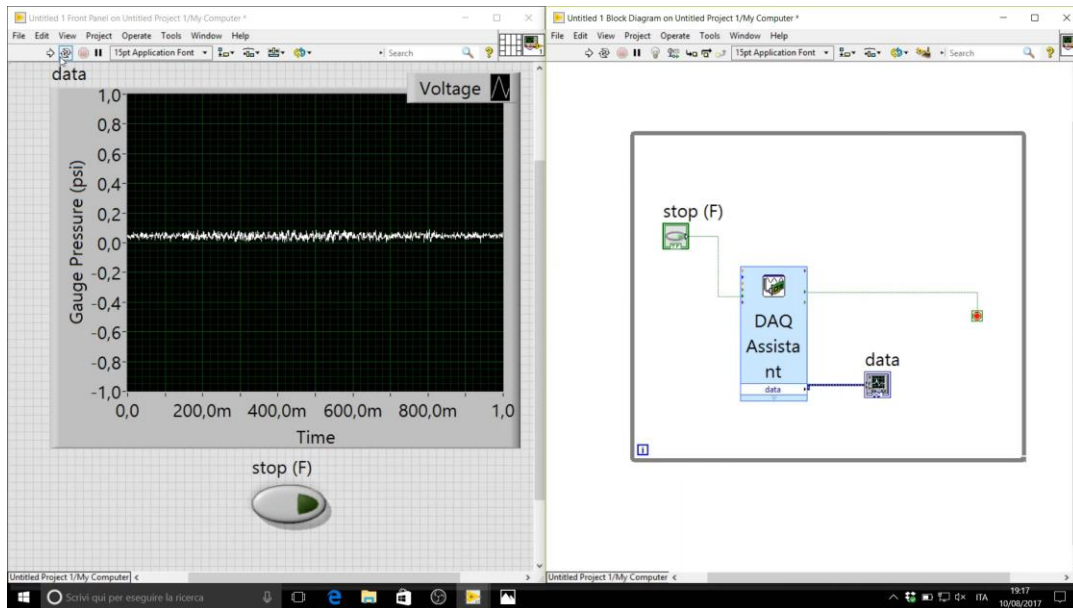*Figure 18: Spectral Analysis of the acquired temperature data*

Figure 19: Pressure data acquisition using a PX603 Transducer and the NI-USB 6009 DAQ device

This practical with the LabView ambient is of fundamental importance because almost all the instruments used in the Industries and in the University Laboratories are linked to the computers and managed by this software, which is, in practice, a standard. At the Aerodynamics Research Center of the UTA this software is used to acquire the data from the pressure transducers and the thermocouples and also to command the aperture of the pressure valve, for example to run the wind tunnels. The Supersonic Wind Tunnel for example, which is used to perform the experiments on the scramjet injectors, is totally commanded by using the LabView program. In Figure 20 we show a picture of the computer by which we can run the tunnel (i.e. open the control valve) and at the same time acquire the pressure data and the temperature data from the several sensors placed in the critical point of the wind tunnel (i.e. plenum, test section and so on).

Figure 20: LabView program for the data acquisition and control of the Supersonic Wind Tunnel at UTA

2.4.   Experiments

Once we have acquired a certain knowledge about the Rayleigh scattering and its application and about the use of the LabView program, we are now ready to perform our experiments.

The goal of the experiments is to measure the flow field density downstream the scramjet injector developed by the Aerodynamic Research Center, in order to study the mixing of the vortices. The experiments have been carried out, together with Phd student Vijay Gopal, in the same way as in the work performed by Prof. Luca Maddalena and Cody Ground in [5]. The high-quality experiments setup to perform the measurement of the Rayleigh scattering is showed in Figures 21 and 22.
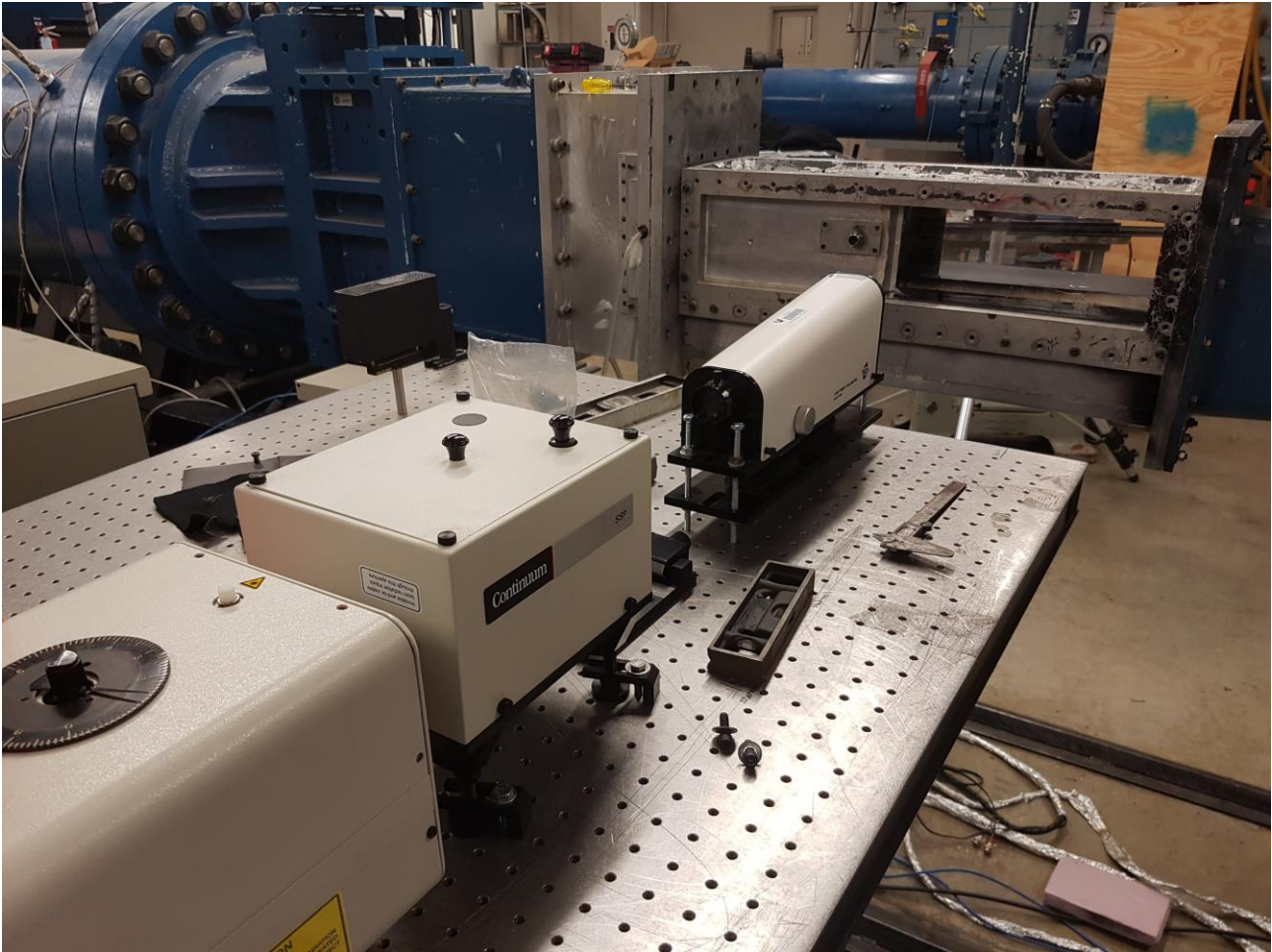

Figure 21: Setup for Filtered Rayleigh Scattering experiments at ARC, laser side

In Figure 21 we can see the laser side: there are visible the laser, the collimator and the test section with the windows to allow the measurements. The laser provides a light beam of around 0.4 J at a frequency of 532 nm (green light). The collimator, using some lenses, transform the laser beam into a laser sheet in order to illuminate the flow with a laser plane.

In Figure 22 there is the camera side: there are visible the camera, the molecular filter in front of the camera and the temperature controller of the filter. The molecular filter is of fundamental importance and it is a iodine cell filter which is able to remove the 532 nm light (which corresponds to the laser one) and, in this way, we can register with the camera only the Rayleigh scattering which is not at 532 nm because we have a high velocity flow and the Doppler effect will change the frequency of emission of the scattering light. It's important to maintain the temperature of the filter at 80 °C because the properties of the filter change with temperature (and also with pressure).
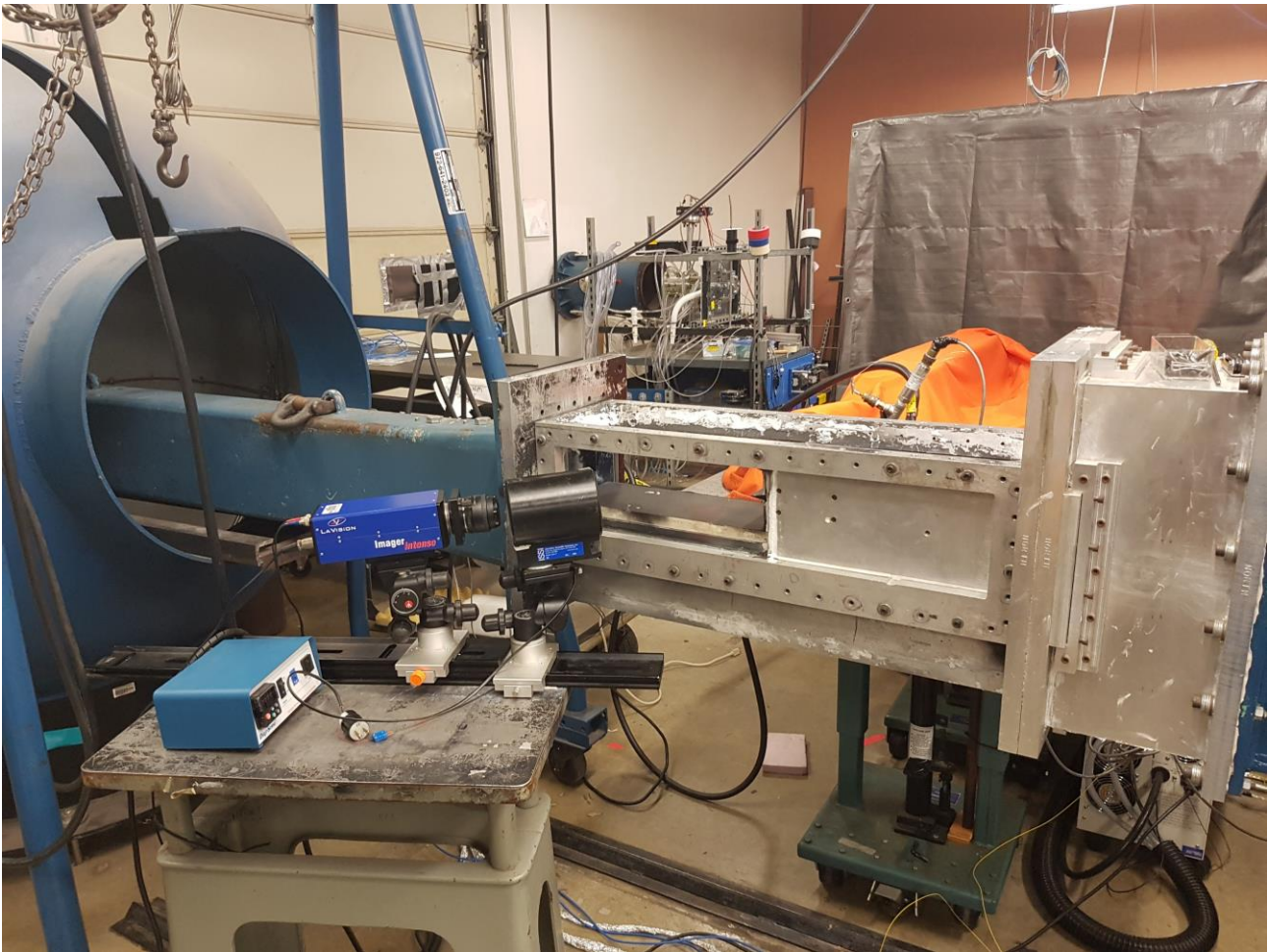
Figure 22: Setup for Filtered Rayleigh Scattering experiments at ARC, camera side

An example of transmission curve for the molecular filter is shown in Figure 23 in which we present a Iodine filter transmission profile as function of nitrogen-buffered gas pressure, which can be used to modify the shape of the transmission line (for example in the Planar Doppler velocimetry). In our case we change the property of the laser more than change the transmission line of the iodine cell.
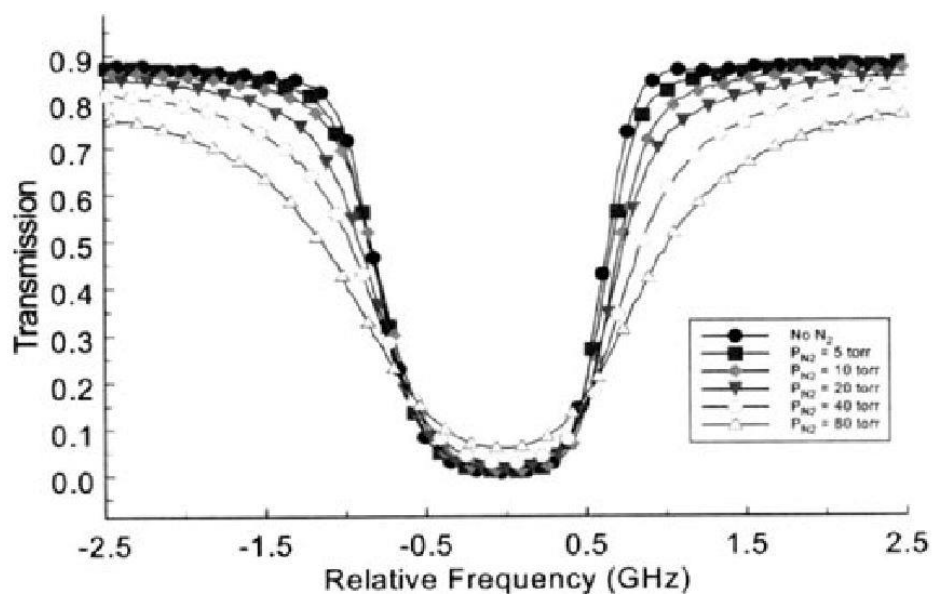

Figure 23: Iodine filter transmission profile as function of nitrogen-buffered gas pressure from [6]

The preparation for the experiment is composed by some fundamental steps which can be summarized as follows:

- Alignment of the camera and the laser
- Calibration of the camera
- Filling the plenum at a pressure of 320 Psi.
- Checking the mass flow rate of Helium and Air
- Measuring the energy of the laser beam
- Changing the input voltage for the seeder (i.e. the frequency of the laser beam)

The first step is to align the camera and the laser to the position downstream the injector at which we want to measure our flow properties. During the internship, we have performed several experiments at two different downstream positions: the 13h and the 20h, where h is a characteristic length of the problem (i.e. the height of the ramp of the injector). The alignment process consists in putting the calibration plate at the right distance from the injector and in moving the laser table and the camera in order to have the laser sheet perfectly aligned with the plate, as in figure 24. It's important to underline that the alignment process is extremely sensible to the weather and to the time during the day (i.e. outside temperature). In fact part of the supersonic wind tunnel (i.e. air tank and diffuser) is outside the building and variation in the ambient temperature are felt by the entire tunnel which expands or contracts in sensible way also for a few degree Celsius (the length of the tunnel is of the order of ten of meters). Another problem is the vibration of the laser table during the running of the tunnel: the vibration can cause some shift in the laser beam frequency. To reduce at the minimum this issue an anti-vibration pad is used below the table.

Figure 24: Alignment process for the FRS experiments; collimator and calibration plate

During the alignment process we need also to check the height and the shape of the laser sheet. The latter is commanded by the collimator for which we can modify the relative lenses positions. In Figure 25 we show the different form of the laser sheet for different position of the central lens of the collimator. We can see how the complete forward position gives the best result in terms of constant sheet height: from the left side to the right side we have no difference in the sheet shape while in the completely backward position we have a reduction of the laser sheet height from the left to the right side of the test section. In the same figure is

possible to see the injector shape, formed by two ramps: in between of them the fuel can be injected in the air flow. In our case we inject helium and air because of safety reason, as we will explain better later.

The next step of the preparation phase is the calibration of the camera, by using the dedicated program by LaVision (see Figure 26). During this process the software recognizes the calibration plate geometry (i.e. holes and rows) and associates to each pixel a point in the space.
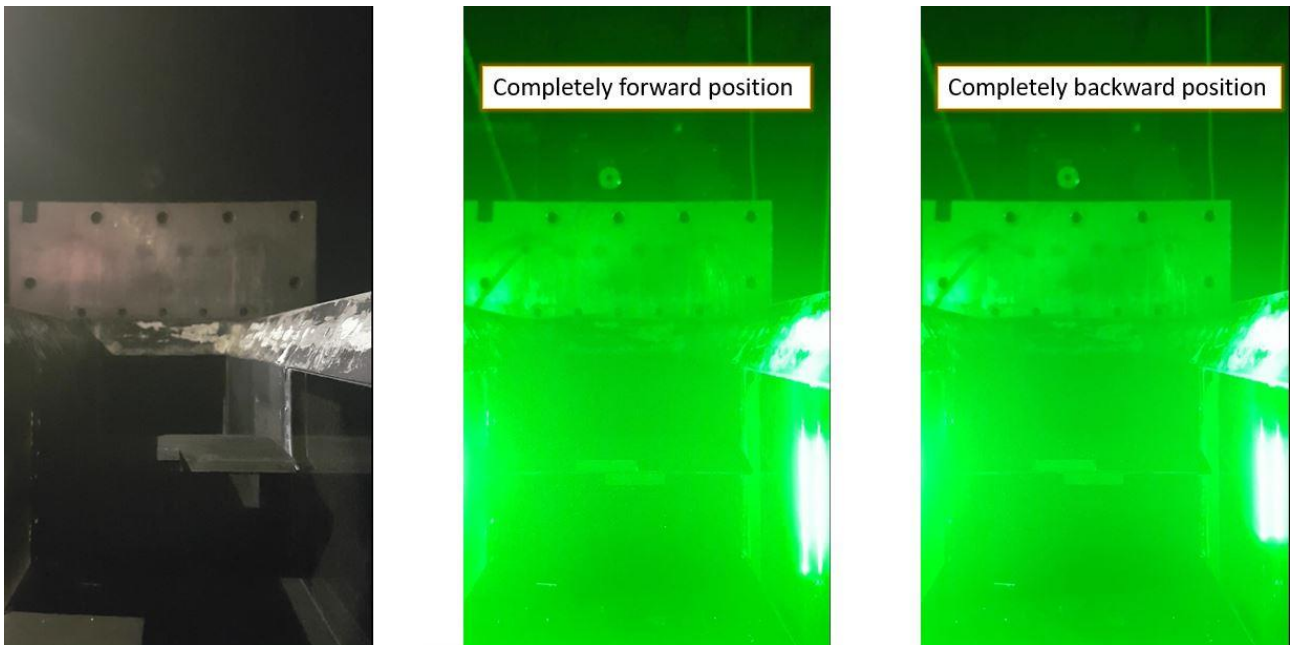

Figure 25: Effect of central lens position of the collimator on the laser sheet shape
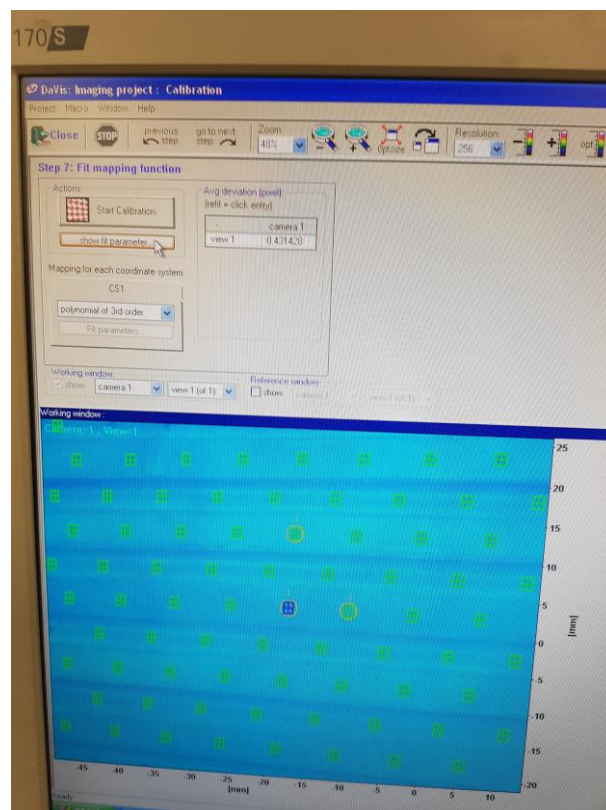

Figure 26: Calibration process using dedicated LaVision software

The compressor (see Figure 2, right) provides the needed pressure to run the supersonic wind tunnel. To do so the plenum is filled at 320 psi (i.e. 21.7 atm) before the run. At this point we can check the pressure at which we inject Helium and Air and, by modifying it, we can modify the mass flow rate of Helium and Air. As a matter of fact, during the run, we inject (through the injector) the Helium and then the Air (or viceversa) in such a way that they have almost the same number density (i.e. confrontable Rayleigh signal): by subtracting the two Rayleigh scattering from the two gases we can obtain information about the flow field at that station downstream the injector [5]. The geometry of the injector is shown better in Figure 27. There are two ramps (one that is visible in the picture and the other that is below) which create vortices in such a way to mix the air (coming from behind) and the fuel injected from in between the two ramps (in our case we use Helium and Air again to check the vortices structure without combustion).
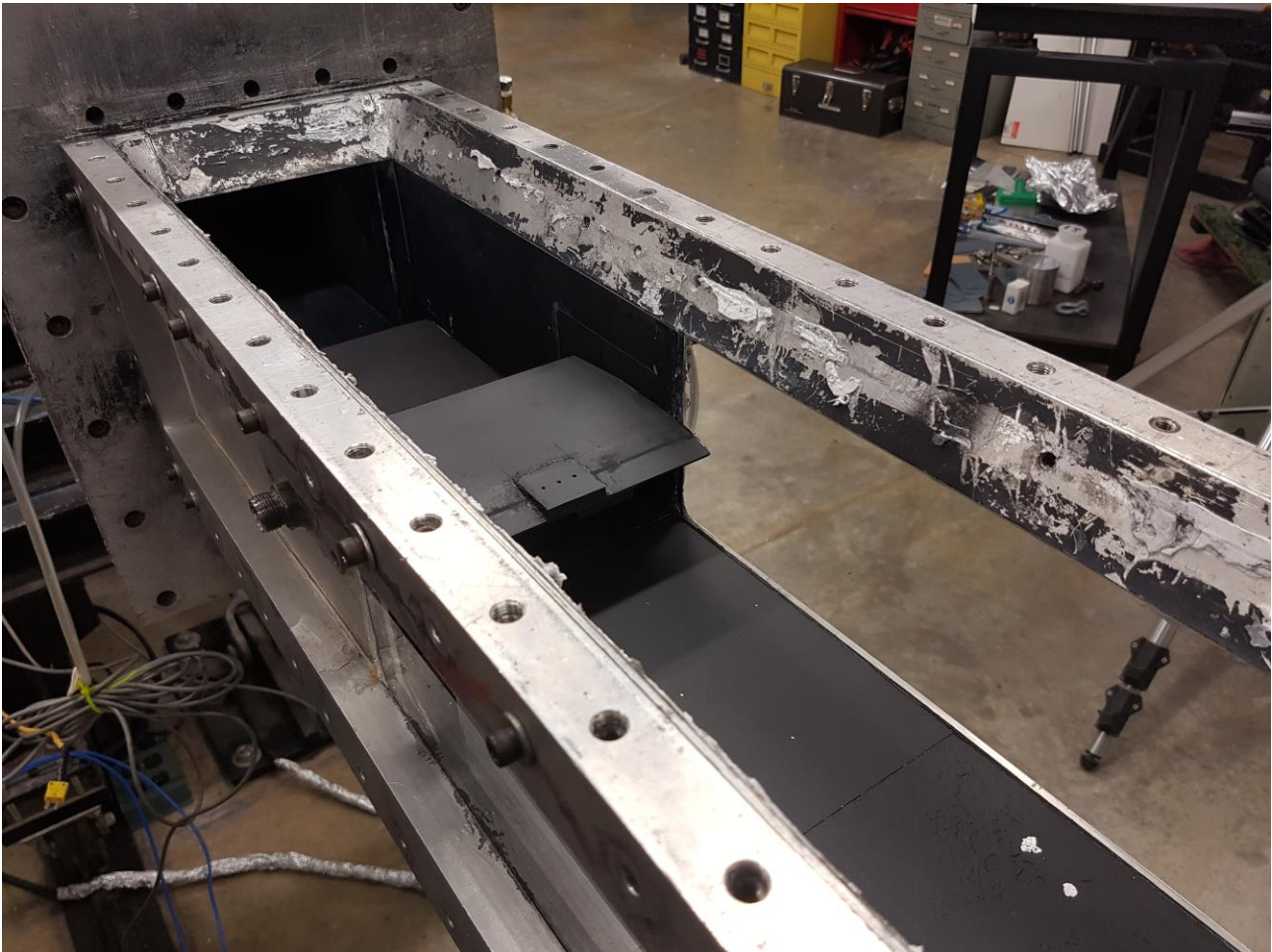

Figure 27: Scramjet Injector developed by UTA and installed to test inside the supersonic wind tunnel test section

At this point what it is left is to measure the energy of the laser beam, which is different day by day (but always around 0.4 J) and that depends on the conditions in that moment.

The last but not least step before the experiment is the checking of the background light. What we do is to turn on the laser and the camera and change the input voltage of the seeder (that in practice control the frequency of the laser light): in this way we check if the laser light is at exactly the frequency for which the iodine filter has the lowest transmission. In this way we can register with the camera, ideally, only the Rayleigh scattering from the flow without the actual laser light. In fact, as we have explained before, the Rayleigh scattering is shifted in frequency with respect to the laser beam itself due to the Doppler effect, since the flow is moving at a certain (high) velocity.

Everything is now ready for the experiment (see Figure 28). The air flow inside the tunnel is flowing from the right to the left (at a Mach of 2.5). In the picture it's possible to see, from the left to the right, the controller for the iodine cell temperature, the camera, the molecular filter, the test section, the system for injecting the Helium/Air through the injector (black tube which goes inside the test section), the collimator, the laser and the seeder (in the top right part).

Figure 28: Setup ready for the FSR experiments

The experiment world is a strange world in which everything can happen as the Murphy law says: for example, lower ramp of the injector flew away during the first run (see Figure 29). However, everything was going well after having replaced the ramp.

In Figure 30 we can see the ongoing picture of the experiment: it's possible to see the laser sheet that is constant inside the test section, but which is reducing its height after some meters (the collimator is not a perfect instrument).

Finally, in Figure 31 we present two instantaneous images taken from the experiments. The vortices structure is clearly visible in these pictures and they corresponds to the dark blue region with a double S shape. These images must be post-processed and, in order to get convergence, we need more than one hundred good photographs for both Helium and Air injection. From the comparison between the two converged averaged images we can get information about the molar fraction of the Helium. In this Figure we can see also some spot of light: these are due to the external small particles in the flow that cause a higher Rayleigh signal because of their higher scattering cross section.
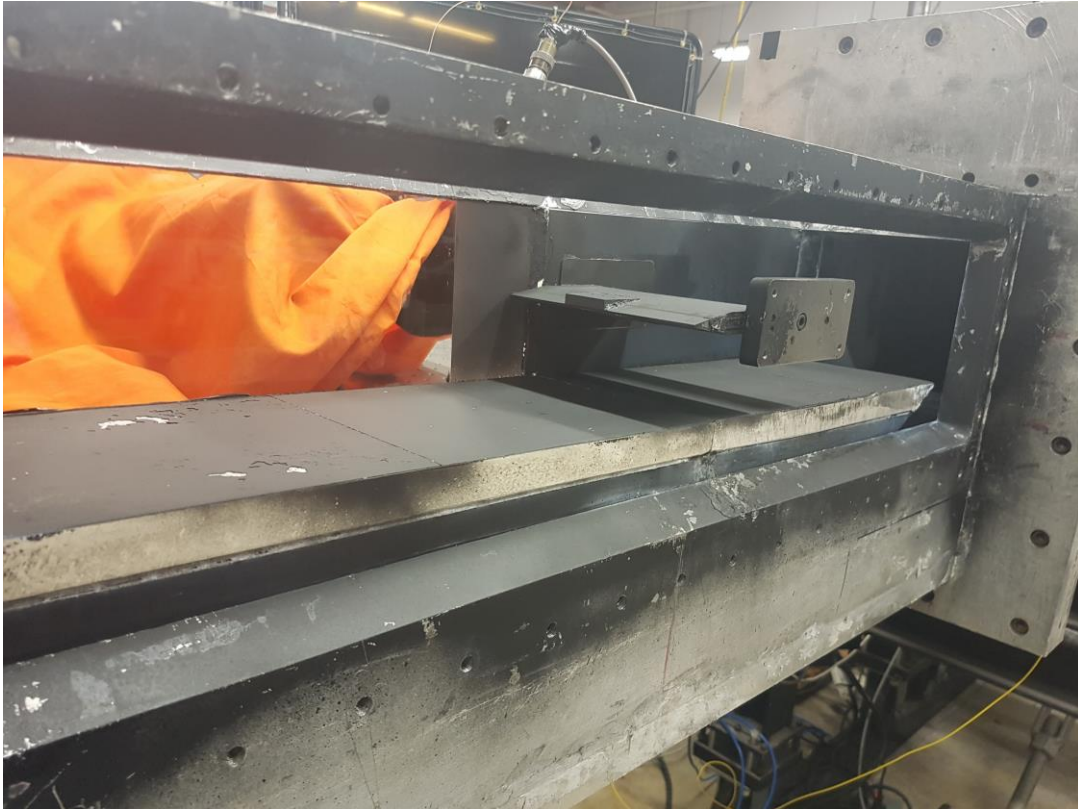
Figure 29: The lower ramp of the injector flew away during the first run
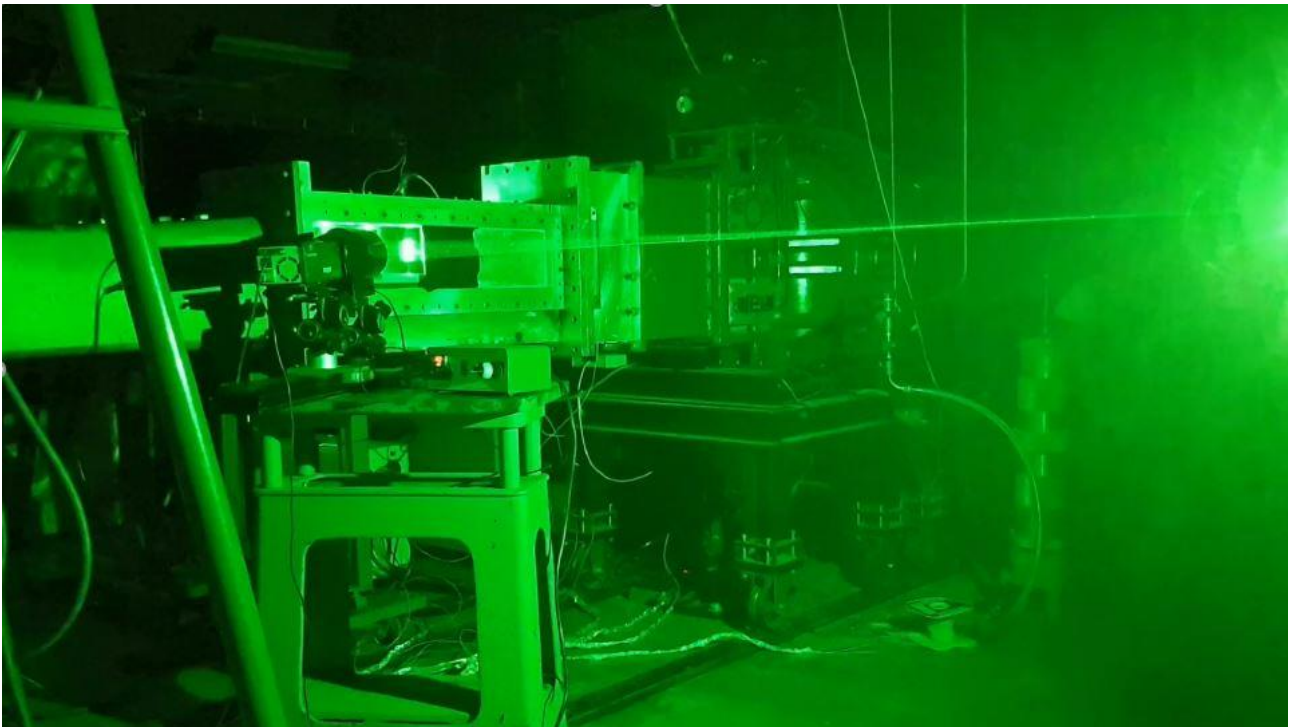

Figure 30: FRS experiment in progress, laser sheet visible with the camera and the molecular filter
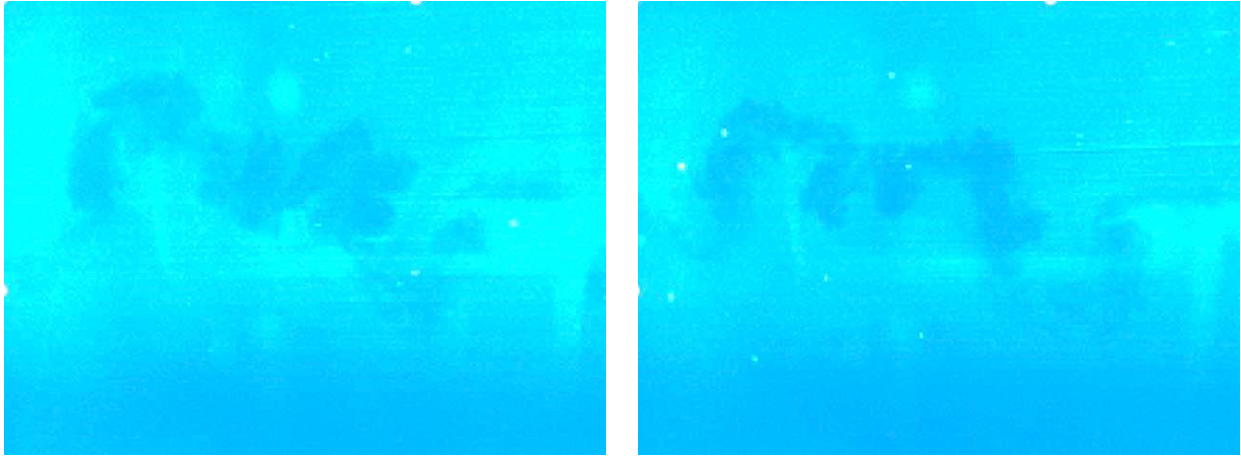
Figure 31: Instantaneous images from the FRS experiments, it's clearly visible the double S shape of the vortices in dark blue

In Figure 32 we present the solution of this process, in which we can read on the color scale the molar fraction of the Helium. There we can see the centers of the four vortices, in which the molar fraction of the Helium is higher (in red). The high concentration of Helium detected in the bottom left corner is due to background light not perfectly removed by the molecular filter. The averaged image showed needed other images to achieve the convergence. In general, we need around 10 good tunnel runs to get convergence, i.e. to detect the shape of the vortices at a certain station downstream the injector.
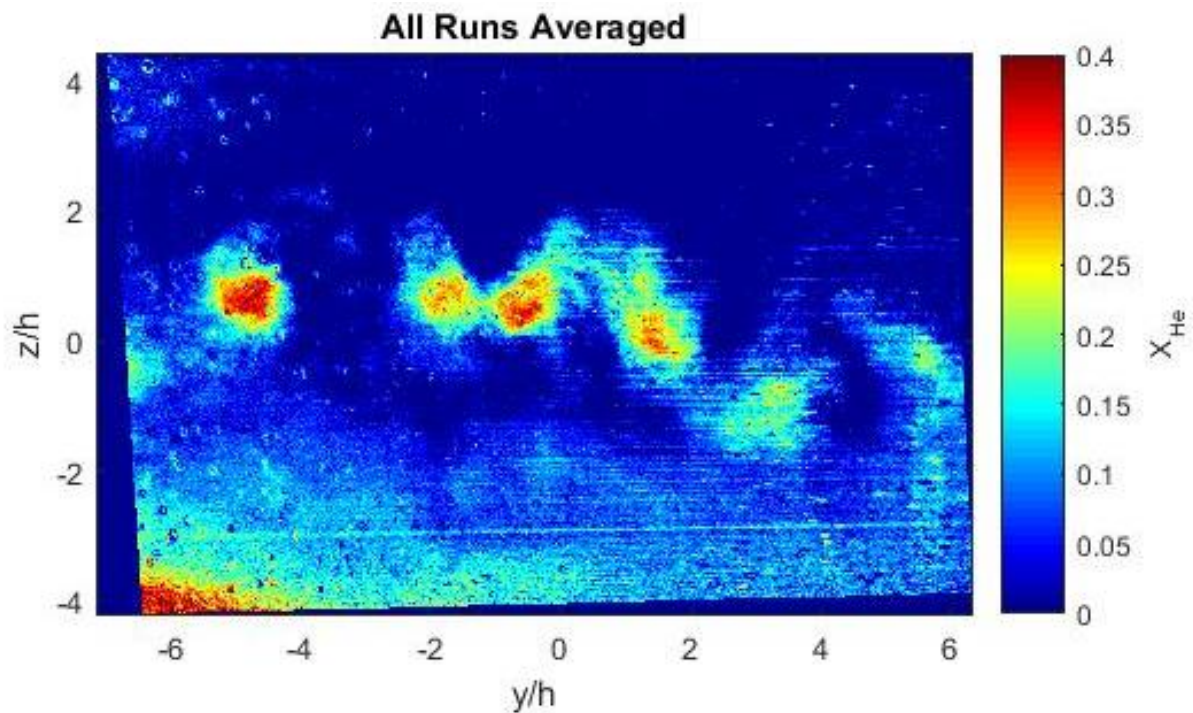

Figure 32: Average image of all the runs showing the Helium molar fraction, notice the four vortices centers

3.   Design of an emergency flange

3.1.   Problem definition

The new Hypersonic Plasma Wind Tunnel, which is under manufacturing process, has the classic structure of a Hypersonic Wind Tunnel (showed in Figure 3) and it requires a very expensive vacuum pump system (around one half millions of dollars) to allow the flow to be accelerated to hypersonic velocity inside the test chamber. The hot flow, generating by the arc heater, is still at very high temperature at the end of the diffuser and it is cool down by the heat exchanger before entering in contact with the vacuum system.
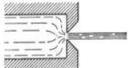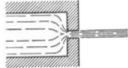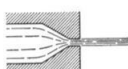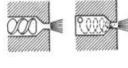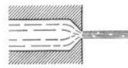
At this point we can ask ourselves: what happens if the heat exchanger is not able to cool down the flow from thousands of Celsius degrees to a few tens? What happens is that the hot flow will destroy the vacuum system and, together with it, hundreds of thousands of dollars. The heat exchanger was designed in order to provide very good cool down capability but, in this case, the prudence is never too much: we may want to introduce another safety factor.

The idea is to design a new flange that we can insert in-between the diffuser and the heat exchanger: through this flange we can inject some cold flow in order to mix this flow with the hot flow coming from the test chamber in order to cool down the overall temperature of the mixing before reaching the vacuum system.

This kind of flange is intended to be an emergency flange, in the sense that there should be a control loop that must activate the injection of the cold flow when the temperature of the air at the vacuum system is increasing too much. Of course, if the design performances of the heat exchanger are observed, there would be no need to introduce cold flow from this flange.

The first idea that we had was to use water as cold flow: water has in fact a very high specific heat and heat of vaporization. The idea is to use a flange with injectors that atomize the water in order to have a quick heat exchange in case of emergency but there should be also a regular cooling system that cools the flange in normal operation conditions because there would be heat exchange from the hot flow to the walls of the flange even if the heat exchanger works properly. The flange that we want to use is a standard ANSI B16.5 CLASS 150, which has compatible dimensions of the diffuser exit and the heat exchanger entrance.

To get the mass flow rate across the injectors we may refer to the equation in Figure 33 from [18].

Mass flow rate across one injector (incompressible, liquid)

$$\dot{m} = A_{inj} C_d \sqrt{2 \Delta p_{inj} \rho}$$

A_{inj} : Area of injection

C_d : Discharge coefficient

Δp_{inj} : pressure drop across the orifice

ρ : density of the fluid

Orifice Type	Diagram	Diameter (mm)	Discharge Coefficient
Sharp-edged orifice		Above 2.5 / Below 2.5	0.61 / 0.65 approx.
Short-tube with rounded entrance $L/D > 3.0$		1.00 / 1.57 / 1.00 (with $L/D \sim 1.0$)	0.88 / 0.90 / 0.70
Short tube with conical entrance		0.50 / 1.00 / 1.57 / 2.54 / 3.18	0.7 / 0.82 / 0.76 / 0.84–0.80 / 0.84–0.78
Short tube with spiral effect		1.0–6.4	0.2–0.55
Sharp-edged cone		1.00 / 1.57	0.70–0.69 / 0.72

Figure 33: Mass flow rate across one injector (left) and properties of the classical orifices (right) from [18]

The discharge coefficient introduced in the equation takes into account the compressibility effect of the flow: in the same Figure 33 (right) we have the discharge coefficients for different types of injectors geometry. In the first design proposal it happens that we usually don't know the injectors geometry yet, so we chose a geometry with a certain discharge coefficient and later we will return on this selection doing an iterative design process. Another important process to be taken into account is the cavitation effect (Figure 34) for which we may have locally a drop in the pressure with the immediate vaporization of the liquid which causes a reduction of the injectors area (i.e. vena contracta) and so a reduced mass flow rate.
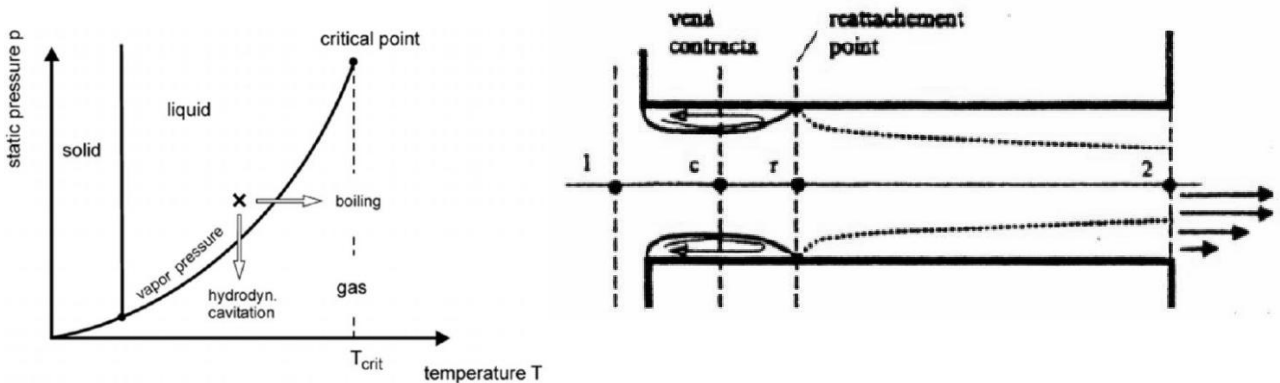

*Figure 34: Scheme of the cavitation problem in the injectors from [18]*

What we have to consider more are also the requirements for obtaining a stable atomization, as in Figure 35. There we can see the different types of jet behavior as functions of the characteristic Ohnesorge and the Weber dimensionless number.

$$We = \frac{\rho_{gas} d_{inj} (v_{liq} - v_{gas})^2}{\sigma} \qquad \text{Ratio between drag and surface tension } \sigma$$

$$Oh = \frac{\mu_{liq}}{\rho_{liq} d_{inj} \sigma} \qquad \text{Ratio between viscous effect and surface tension } \sigma$$

We << 1

We = 1

We > 1
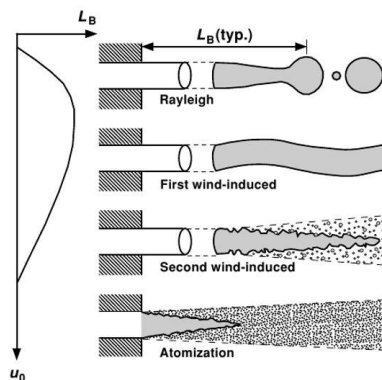
Size dependent from boundary conditions (experiments needed)

We > 10-40 and Oh > 2-4

Stable atomization is obtained

Figure 35: Requirements for a stable atomization process, from [18]

Having clarified the different problems that we have to solve, we can now proceed with an injector design proposal. We need the flow properties inside the diffuser, the temperature of the flow that we want at the end of the mixing and the mass flow rate of the injected water. We can calculate the number and dimension of the holes and the ΔP required for atomization. Before passing to the injectors geometry, we have to calculate the needed mass flow rate of the injected water. To do so we take a simple control volume, as it is

showed in Figure 36, for which we have hot flow coming from the diffuser, cold injected water and mixing flow that is going to the vacuum system.
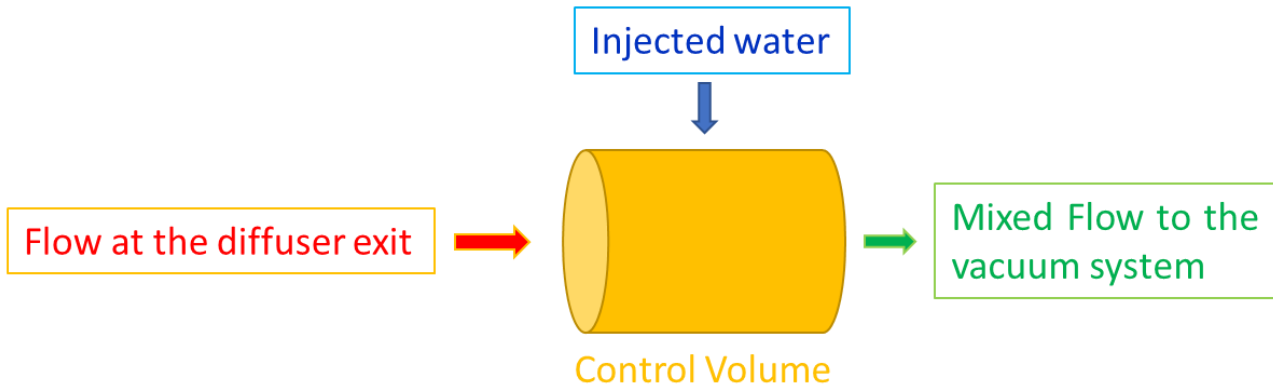

Figure 36: Control Volume for the calculation of the needed mass flow rate of injected water

To do the calculations we require some data about the flow at the diffuser exit, taken from [19] and showed in Figure 37, and we have to do some assumptions:

- The mixed flow is in equilibrium at the final temperature (good assumption since the flow velocity is low)
- The air Temperature at the diffuser exit is 3600 K (maximum in Figure 37)
- The pressure is 33 mbar = 3300 Pa (see Figure 37)
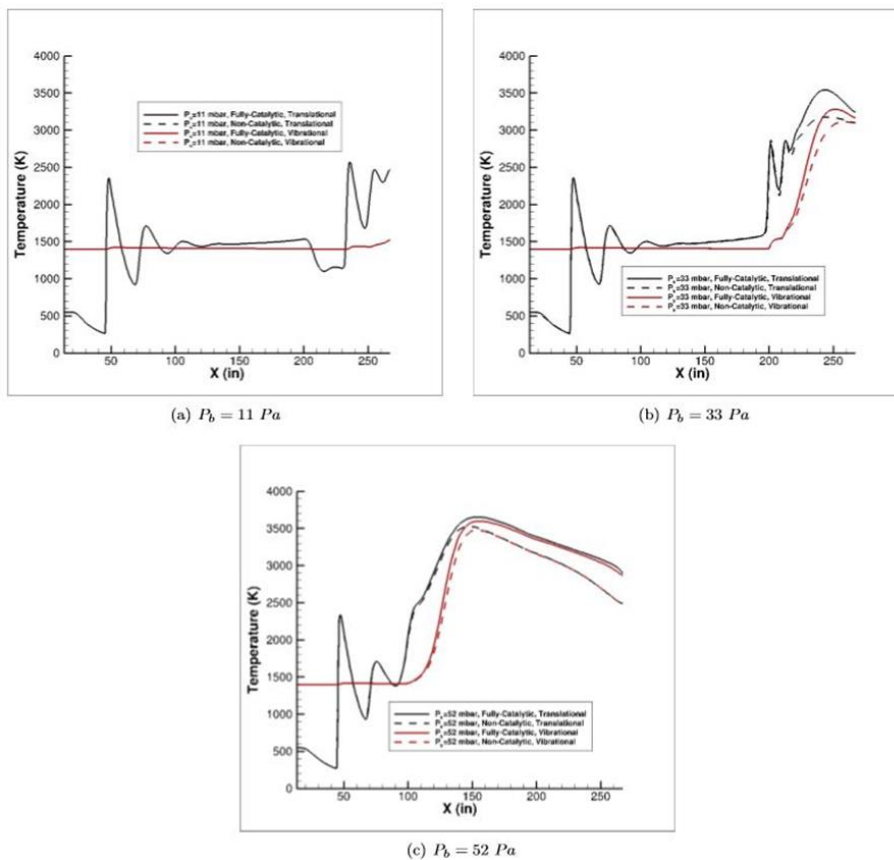- Air composed by 76.7% N2, 23.3% O2 (mass fraction)

Figure 37: Centerline distribution of the temperatures along the diffuser for different back pressures conditions, [19]

To calculate the equilibrium condition of the flow we have used the NASA CEA application [20]. What we get is showed in Table 1, where we show the final temperature for different water mass flow rate. The water initial temperature is assumed to be 298.15 K.

Water/Air mass ratio	0.5	1	1.5	2	2.5	3	3.5
Mixed flow T [K]	2376.5	1759.2	1205.2	825.63	546.4	331.8	295.8

Table 1: Final temperature of the mixed flow for different Water/Air mass flow rate ratio

From this Table it's evident that, if we want a low Temperature compatible with the vacuum system we have to select a ratio of 3.5, as in Table 2 where we can see the needed water mass flow rate.

	Temperature [K]	Mass flow rate [kg/s]
Air at the diffuser exit	3600 (conservative choice)	0.1087 (calculated at the nozzle exit)
Injected water	298.15	0.38
Mixed flow	295.8	0.489

Table 2: Optimal mass flow rate of injected water and final temperature of the mixed flow

At this point we can assume a ΔP of 10 atm (actual gauge pressure for the cooling system) and we can calculate the velocity of the injected water (assume C_d=0.7) as in equation 19.

$$v_{liq} = C_d \sqrt{\frac{2\,\Delta P}{\rho}} = 0.7 \sqrt{\frac{2*10^6}{1000}} = 31.30 \; m/s \qquad (19)$$

Since $\dot{m} = \rho v A$, we can calculate a total required Area of 1.21 x 10^{-5} m^2 and assuming a diameter of the orifices of 1 mm (common choice in liquid injectors) which means to have a single injector Area of 7.854 x 10^{-7} m^2 we have 16 injectors.

Another important issue that we have to consider is the Flow-System geometry upstream of the orifices which can strongly impact on the pressure distribution (and hence on the mass flow rate) across the injectors (Figure 38): a deflector plate is often used to improve the pressure distribution.
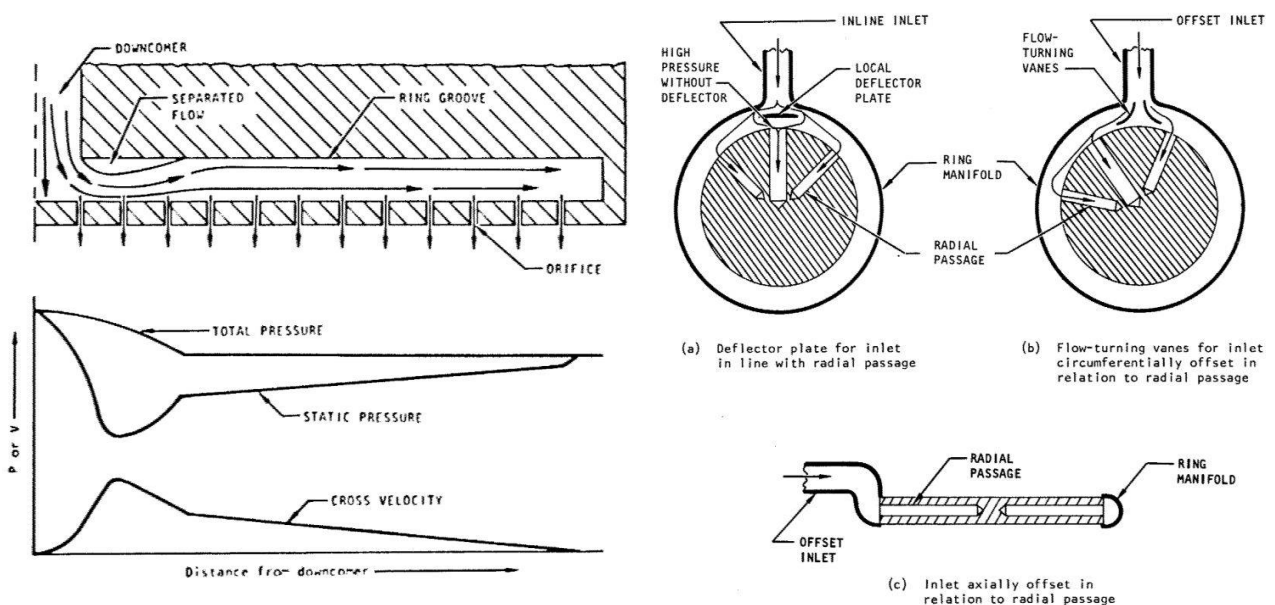

Figure 38: Variation of pressure and velocity in a constant-area ring grove (left) improved pressure distribution in annular manifolds (right) from [18]

In order to check the needed water mass flow rate, we can do a by-hand calculation doing a enthalpy balance. We have the following data:

- Latent Heat of Water is 2257.92 KJ/kg (conservative choice)
- Total maximum plenum (stagnation) temperature of air is 6331 K at 4.65 bar
- The air sensible Enthaply of the air flow is 7730.76kJ/kg. (calculated by CEA).

The mass flow rate ratio to have that all the air sensible enthalpy goes to the vaporization process of the water is easily given by equation 20.

$$\frac{Water\ \dot{m}}{Air\ \dot{m}} = \frac{Air\ sensible\ Enthalpy}{Water\ Latent\ Heat} = \frac{7730.76\ KJ/kg}{2257.92\ KJ/kg} = 3.4238 \qquad (20)$$

The result is near to the 3.5 that we had obtained before using the NASA CEA to calculate the equilibrium conditions.

The above calculations however are not very precise and are overestimating the needed mass flow rate. As a matter of fact, the enthalpy of the flow has been calculated based on the total temperature of the flow but, during the flowing inside the diffuser, part of the enthalpy is exchanged with the diffuser walls (which are cooled down by a regular cooling system). In fact, if we take the enthalpy content of the flow at the diffuser exit taken form [19] we would have less enthalpy if compared to the one used in equation 20 (see Figure 39).

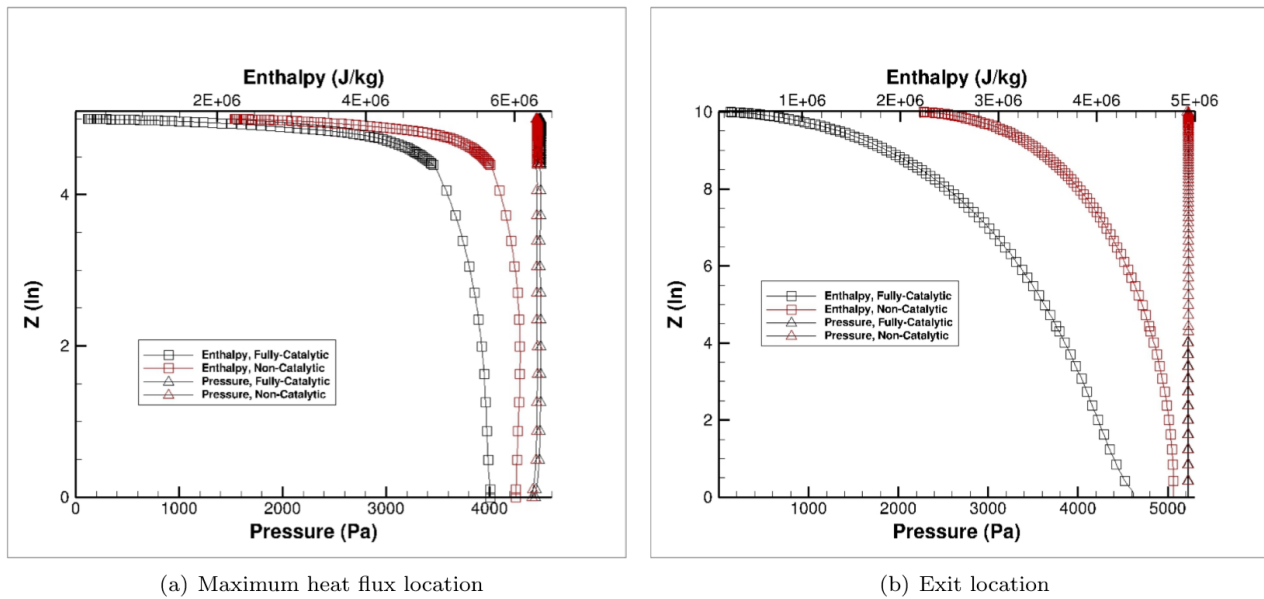(a) Maximum heat flux location

(b) Exit location

Figure 39: Enthalpy and pressure profiles at the diffuser exit and maximum heat flux locations for a back pressure of 52mbar, [19]

If we take now as the maximum absolute enthalpy (chemical and the sensible parts) at the exit of the diffuser the one showed in Figure 39, we would have a value of 5000 KJ/kg (lower than the 7730 KJ/kg used before). Therefore, the needed mass flow rate will be, as in equation 21:

$$\frac{Water\ \dot{m}}{Air\ \dot{m}} = \frac{Air\ sensible\ Enthalpy}{Water\ Latent\ Heat} = \frac{5000\ KJ/kg}{2257.92\ KJ/kg} = 2.215 \qquad (21)$$

At this point, if we apply a safety factor of 1.5 on the needed mass flow rate we would have a ratio water/air of 3.323 (water mass flow rate of 0.3612 kg/s). With the same conditions as before, this means that we need a total required Area of 1.154×10^{-5} m^2 and assuming a diameter of the orifices of 2 mm which means to have a single injector Area of $3,142 \times 10^{-6}$ m^2 we have 4 injectors.

We can now check the atomization process by evaluating the characteristic adimensional numbers as in equation 22 and 23 (taking the flow properties from [19] and [21]).

$$We = \frac{0.035 \, x \, 0.002 \, x \, 31.3^2}{0.073} = 0.94 \tag{22}$$

$$Oh = \frac{0.001}{1000 \, x \, 0.002 \, x \, 0.073} = 0.00685 \tag{23}$$

With that low value of Oh number, the critical We number is 12, much higher than the actual value [22]. The low pressure and, hence, the low density of the gas at the diffuser exit causes an aerodynamic drag force which is not sufficient for atomize the water flow since water has a high superficial tension. We may think to some possible solutions as:

- Increase the diameter of the injectors in order to increase the Weber number (bigger bubbles)

- Increase the velocity of the injected water: but we have the limit on the ΔP

- Increase the relative velocity between the liquid and the gas

The air flow at the diffuser end has still a velocity of 120 m/s (P_b = 0.052 bar). Since we cannot inject the water perfectly in the upstream direction, let's consider a certain injection angle θ. The projection of the air velocity would be v=120 x sin (θ) and, to have We = 12 we need an angle θ for example of 42.17° (relative velocity of 111,86 m/s).

3.2. Water injection in vacuum: ice formation issue

At this point is important to check if the atomization process is really a fundamental process to mix our flows. Let's check the water phase diagram showed in Figure 40. The flow pressure at the diffuser exit varies from 1100 Pa to 5200 Pa; for this range of pressure and, for a water initial temperature of 25 °C we may have vapour at the equilibrium for the lower part of the pressure range. Since we are close to the boiling curve the atomization appears to be not so important because the water will vaporize due to the low pressure (see Table 3).

Pressure [Pa]	Boiling Point [°C]
2000	17.51
3000	24.10
4000	28.98
5000	32.90
6000	36.18

Table 3: Water boiling point for different pressures, from [21]

But are we sure that the water will vaporize when it reaches the low pressure at the diffuser exit? The experience says that, in reality, the quick vaporization process can lower too much the temperature of the water locally and it can bring to the possible formation of ice that can block the injectors and do not allow the mixing of the flow with the hot air coming from the diffuser. Great attention has been posed to

understand this problem and to solve this issue during the internship because, of course, we want to be sure that we are able to cool down the hot flow temperature with the injected water.
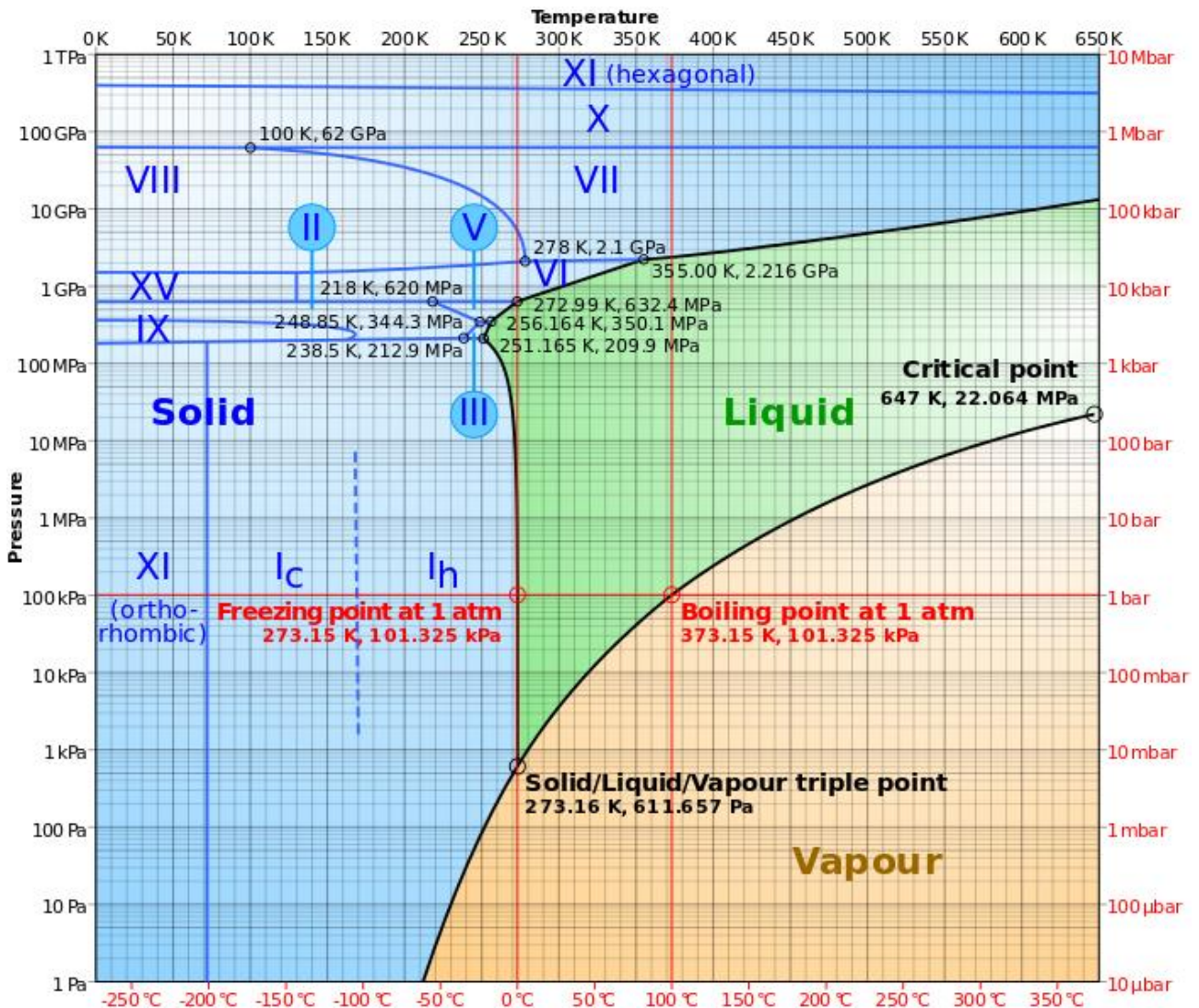

Figure 40: Water phase diagram from [23]

As a matter of fact, there are a lot of experiments which have been done and that show how, if we decrease the pressure, the water is vaporizing, and part of the water becomes ice. Data strictly linked to this problem can be found in the work done at the at the German Aerospace Center (DLR) where a possible solution for handling extreme aerothermodynamic heat loads has been investigated [24]. These scientists wanted to use the transpiration cooling to cool down the vehicles during the re-entry phase in the atmosphere. During their test in a hypersonic wind tunnel they were indagating the possibility to inject water from inside the model to the outside: the water vaporizes on the surface of the model (since there is the plasma flow impacting on it) and this vaporization process subtract the energy from the model lowering its temperature.

During these tests, an interesting phenomenon was observed; a huge ice beard was formed on the model (Figure 41). This was not expected to happen, because temperatures in the flow surrounding the model can reach a few thousand degrees. At a pressure of 6 mbar, the so called triple point is reached. Below this pressure, water can only exist in the solid or gaseous phase. The pressure in the reservoir of the model will be equal to the stagnation pressure at the model (17 mbar). Here, the water is in the liquid phase. When the water reaches the surface at points of low pressure (<6 mbar), it undergoes a phase change. Due to the high surrounding temperature, it is expected that vaporization takes place. However, vaporization requires a lot

of energy. Thus, when too much water reaches the surface some of the water cannot be vaporized. The water which does vaporize extracts energy from its surroundings, causing the temperature of the liquid water to drop to the freezing temperature, and thus causing an ice beard to form (see Figure 42).
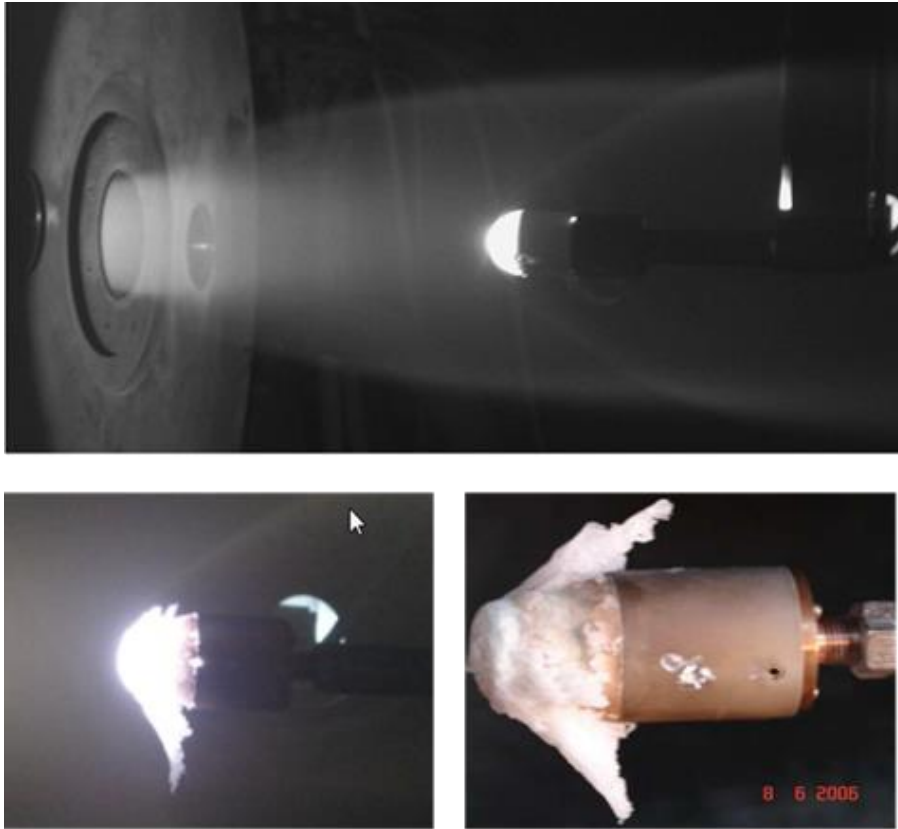

Figure 41: Ice Beard in Hypersonic, High Temperature Flow from [24]

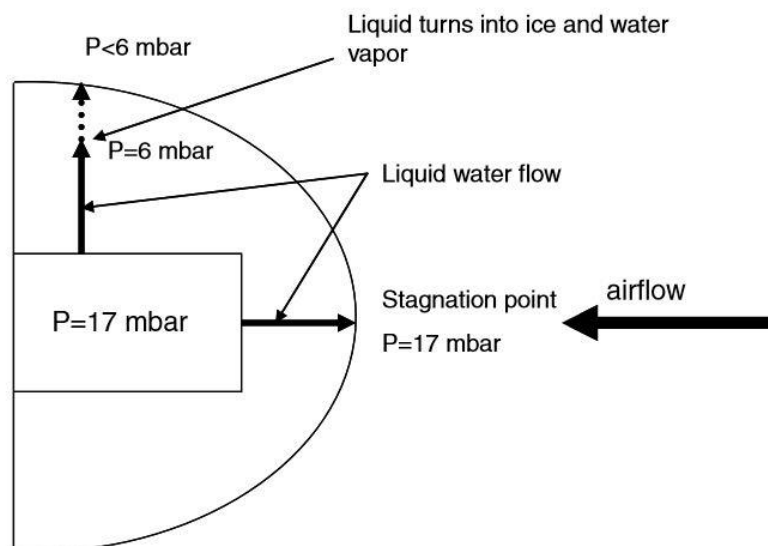*Figure 42: Schematic explanation of ice formation on the cooled model, from [24]*

In Figure 42 we have a schematic of model which indicated the pressure values. The german scientists noticed how, when the model is completely soaked with water, the stagnation point region is cooled to the lowest temperatures. The explanation probably is that in the stagnation point, where pressure is the highest, liquid

water can exists at the surface of the model and, the material cools down to the boiling temperature of the water while at regions of low pressure (<6 mbar) no liquid water can exist.

But which is the physical explanation of that process? During the vaporization process the water is losing the molecules which move faster, and it has no enough time to exchange heat with the ambient: It's temperature will decrease, and it can freeze.

How can we determine if in our case we will have ice formation? Let' go back again to the water phase diagram. In our case, we have liquid water at 10 atm and 25 °C. Reducing the pressure we'll reach the boiling curve. At this point some of water will vaporize and the temperature of the rest of the water will decrease but, at this point, we are no more on the boiling curve. We have to reduce again the pressure to reach again the boiling curve and to form some steam: the temperature of the water will decrease again. At the pressure of 1100 Pa (lower pressure) we would have the remained water at 8.47°C which do not boil anymore (see Figure 43). The point is that the formation of ice is possible only if the ambient pressure is lower than the Triple Point pressure (611.7 Pa) but in our case the minimum pressure is only 1100: we are safe.
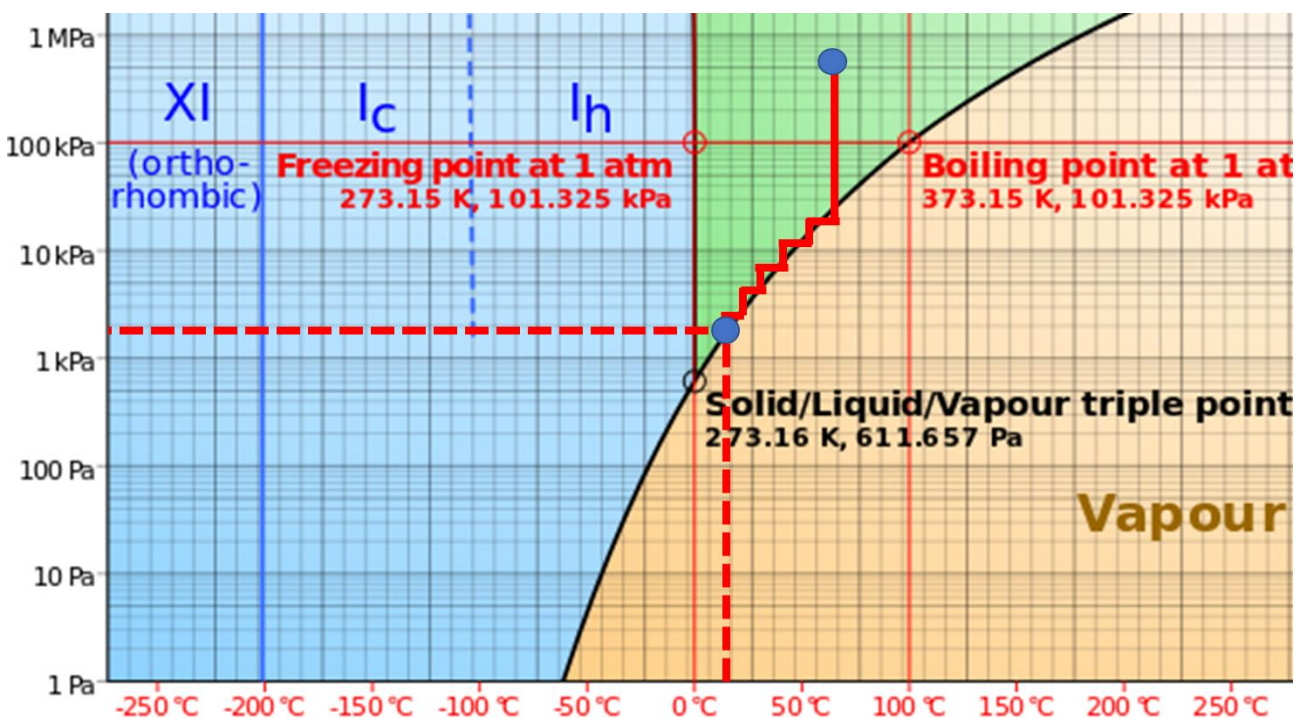

Figure 43: Explanation of the water vapour/ice formation when we lower the pressure, initial and final conditions for our case are indicated by the blue points

To calculate the quantity of formed steam we need the following data/assumptions:

- The mass of water does not exchange heat with the ambient
- The initial temperature of water is 298 K
- The ambient pressure is 1100 Pa (higher than the triple point pressure of 611.7 Pa)
- Specific heat c_p of Water is 4186 J/kg
- Average heat of evaporation is 2400 KJ/kg

The equation that we need is the simple enthalpy balance from the liquid water and the formed vapour, as in equation 24, where x is the quantity of steam formed (see Figure 44).

$$x * (Heat\ of\ evaporation) = (1 - x) * c_p \Delta T \tag{24}$$

ΔT is known from the boiling curve and from the initial and final conditions ($\Delta T = 25°C - 8.47 °C$). At a pressure of 1100 Pa, the final conditions would be 2.8% of steam and 97.2% of liquid water which is not boiling, at a temperature slightly under 8.47 °C (which is the boiling temperature at that pressure): the ice problem is solved.
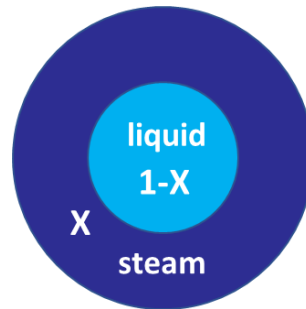

Figure 44: Scheme of the liquid water drops and of the formed steam

Even if we have solved our problem, we want to understand what happens in the German case for the sake of completeness. They have a huge ice formation with a water mass flow rate of 0.5 g/s and also a low ice formation with a water mass flow rate of 0.2 g/s. Having the information about the impinging hot flow from [24] we can calculate the quantity of water mass flow rate which can be vaporized with this amount of enthalpy. The heat flux was not measured during the tests, it was determined numerically by using the DLR program HOTSOSE which uses the equilibrium gas model to account for real gas effects. For a catalytc wall, the heat transfer is independent on the recombination parameter. For both equilibrium flow and frozen flow the heat transfer rate will be the same. The equilibrium gas model therefore was used to determine a total heat flow of 578 W. With this amount of power we would be able to vaporize a quantity of:

$$\dot{m} = \frac{578\ W}{2400\ kJ/kg} = 0.24\ g/s \tag{25}$$

The required mass flow rate is still higher than the effective one: this difference would be explained with the blocking effect of the steam on the model surface. Increasing the enthalpy of the flow a blocking effect of 30% was observed. We can calculate the heat flux on a hemisphere with the formula suggested by Anderson in [25]. The so calculated heat flow is in good agreement with the one reported by Van Foreest. If we apply this correction we would be able to vaporize a water mass flow rate of:

$$\dot{m} = \frac{578\ W\ x\ 70\%}{2400\ kJ/kg} = 0.16\ g/s \tag{26}$$

Which explains the formation of ice with 0.2 g/s: with the heat flux from the hot air we are not able to vaporize all the water and the vaporization process takes part of the energy from the liquid phase itself which therefore freezes.

We can calculate the quantity of ice formed in this case by using the foolowing data taken from [23] and [24]:

- The mass of water receives 406 W from the flow
- The enthalpy given is 2030 KJ/kg
- The initial temperature of water is 298 K
- The test chamber pressure is 55.61 Pa (lower than the triple point pressure of 611.7 Pa)
- Specific heat c_p of Water is 4186 J/kg
- Average heat of evaporation is 2460 KJ/kg
- Average heat of fusion is 333.5 KJ/kg

We have written a Matlab program which allow us to implement the equations of the enthalpy balance between the different phases in order to calculate the equilibrium condition. What we have to insert are the initial pressure and temperature of the liquid water, the (lower) final pressure and the enthalpy given to the water. The results for the German case are shown in figure 45 from the Matlab code: we would have only steam for the 85.52% and the rest is ice at a temperature of 246.05K. No liquid water can exist since we are at a pressure lower than the triple point. In Figure 46 we present the transformation of the water on the phase diagram.

```
Command Window                                                                  ⊛
  The starting point should be from equilibrium conditions for liquid water
  Type the initial pressure of the water in Pa: 101013
  Type the initial temperature of the water in K: 298
  Type the final Pressure of the water in Pa: 51
  Type the Enthalpy given to the water (>=0) in J/kg: 2030000
  The steam formed until P3 is 83.23 %
  The steam formed after P3 is 2.00 %
  The total steam formed is 85.52 % of water while the rest is ice at a Temperature of 246.05 K
fx >>
```

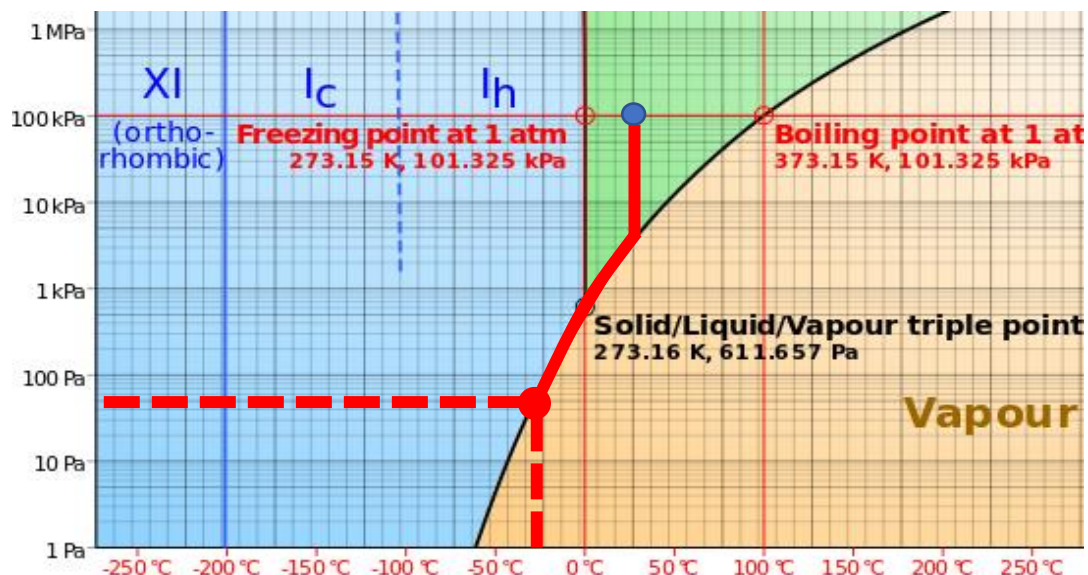*Figure 45: Equilibrium condition for the German case [24] calculated with our Matlab code*

Figure 46: Transformation of the liquid water into ice and steam for the German case

3.3. Jet characteristics

Having solved the ice problem, we can now focus our attention on the characteristics of the water jet: namely the penetration of the jet into the air cross flow and the atomization process. As a matter of fact we want to check if the water jet is able to penetrate the air cross flow and if mixing between the two flow happens before reaching the heat exchanger tubes.

There are many studies in literature on the behavior of a jet column injected transversely in a cross flow, both for subsonic [26] and supersonic case [27]. As a matter of fact, at the end of the diffuser we could have a supersonic or a subsonic flow, depending on the back pressure that we set (i.e. on the operation conditions of the vacuum system) [19]. In Figure 47 we present the typical behavior of a jet column in a subsonic flow

from [26]. Here we can see clearly the column breakup with the formation of the droplets: we want to check if the jet is able to reach the axis of the diffuser, i.e. to cool down the whole flow.

From our literature review it turned out that the principal adimensional parameter for the studying of the column behavior is the momentum ratio q between the cross flow and the injected liquid.
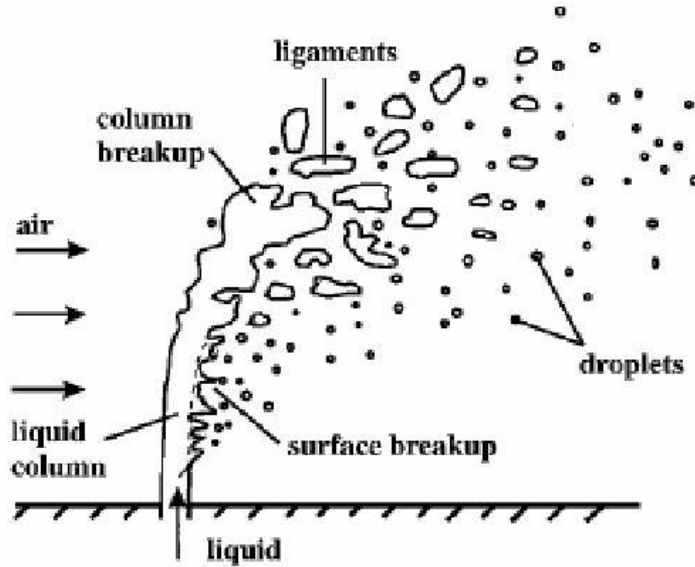

Figure 47: Behavior of a typical jet column in subsonic cross flow from [26]

In the following Table 4 we have the data about the density and velocity of the air cross flow at the end of the diffuser and the injected water from our flange.

Properties	Air	Water
Density	0.007 kg/m^3	1000 kg/m^3
Velocity	120 m/s	31.3 m/s

Table 4: Properties of the air cross flow at the diffuser exit in subsonic case (i.e. back pressure of 52 Pa) and of the water jet

From the air properties (taken from [19]) and from the water jet properties, we can calculate the momentum ratio q, as follows:

$$Momentum\ ratio\ q = \frac{\rho_{water}u^2_{water}}{\rho_{air}u^2_{air}} = 9719 \tag{27}$$

The penetration of the jet is independent of U_{air} and We while it is dependent upon q and D (i.e. diameter of the injectors) and, in particular, penetration increases with q and D. Correlations found in literature were observed to have three different functional forms, power-law, exponential and logarithmic forms (see Figure 48, left). The use of all three models reveals that best results are achieved with the logarithmic model, as in equation 28, where y is the penetration height and z is the coordinate along the downstream direction [26].

$$\frac{y}{D} = 1.55q^{0.53}\ln\left(1+1.66\frac{z}{D}\right) \tag{28}$$

It's easy now to calculate the deviation of the water column when the flow reaches the axis of the diffuser (i.e. the symmetry axis of the flange). With a q = 9719 and a D of 2 mm (point A in Figure 48, right) we reach the center of the flange with a deviation downstream of the jet of 0.46 mm. If we decrease the diameter to

a value of 0.5 mm (B) we have, at the centerline, a deviation downstream of the jet of 0.785 mm. Only with a diameter of 0.1 mm (C) we have, at the centerline, a deviation downstream of the jet of 36.9 mm.
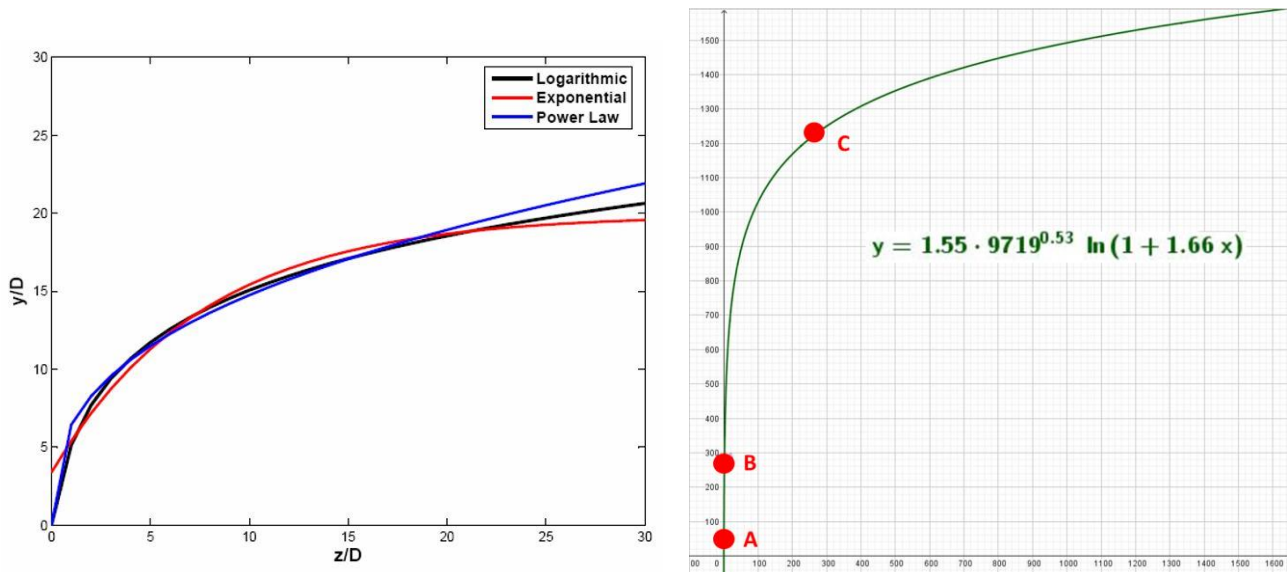

Figure 48: Comparison of computed correlations from [26] (left) and computed correlation for our case (right)

The penetration is not a problem (at least for the subsonic case) and we can choose our injector diameter without taking into account this problem because the momentum ration q is very high (e.g. usual numbers are of the order of tens).

Another important feature is to detect the jet mode breakup, which depends on the q and We values, and which are often divided in three modes (see Figure 49). The process of droplet formation from ligaments is known as Column Breakup and is observed for low values of q and We. Surface Breakup is the mechanism of droplet shearing-off from the walls of the jet and is observed for high values of either q or We. For a typical jet, both of these mechanisms might be active, hence the breakup mode will be determined by the dominant mechanism. However, as we increase either q or We, the extent of surface breakup increases slowly, so that a zone is reached where no clear dominance of either mechanism is seen. This zone has been labeled as Mixed Breakup Mode, that is a transition between the two modes defined earlier. The shift in the breakup mode with an increase in the We is due to an increase in the crossflow dynamic pressure, which increases the droplet shearing mechanism, strengthening the surface breakup. On the other hand, an increase in q increases the penetration, exposing a larger column length to the crossflow, thereby increasing surface breakup. This also leads us to believe that We should have a stronger effect of the modes as compared to q [26].
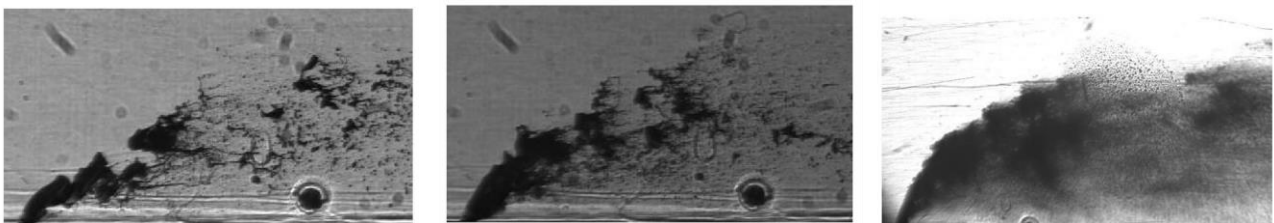

Figure 49: Column breakup mode (left), Mixed breakup mode (center) and Surface breakup mode (right) from [26]

We can detect our breakup mode from Figure 50 where we present the different kind of modes in relation to the values of the momentum ratio and the Weber number. It turns out that we are in the top left part of the diagram where the breakup of the jet is very difficult since the low pressure and, hence, the low density

of the gas at the diffuser exit causes an aerodynamic drag force which is not sufficient for atomize the water flow since water has a very high superficial tension.
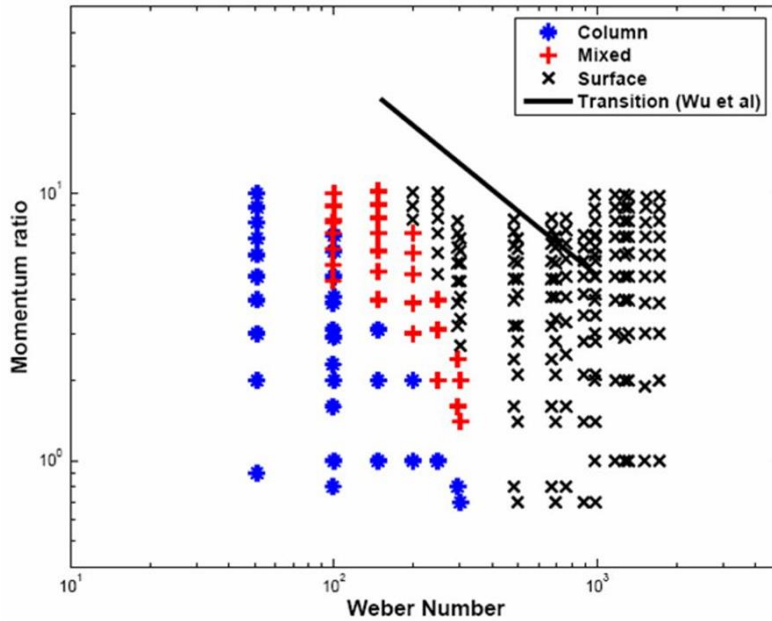

Fig. 7.2 Breakup Modes in We-q plane with the transition line from Wu et al[36]

Figure 50: Breakup Modes in We-q plane from [26], our case is in the top left of the plane

For what regarding the supersonic case we have to take again the properties of the cross-air flow from [19], that are showed in Figure 51 (the black line refers to the supersonic case for which the back pressure is the lowest). The useful quantities are showed in Table 6.
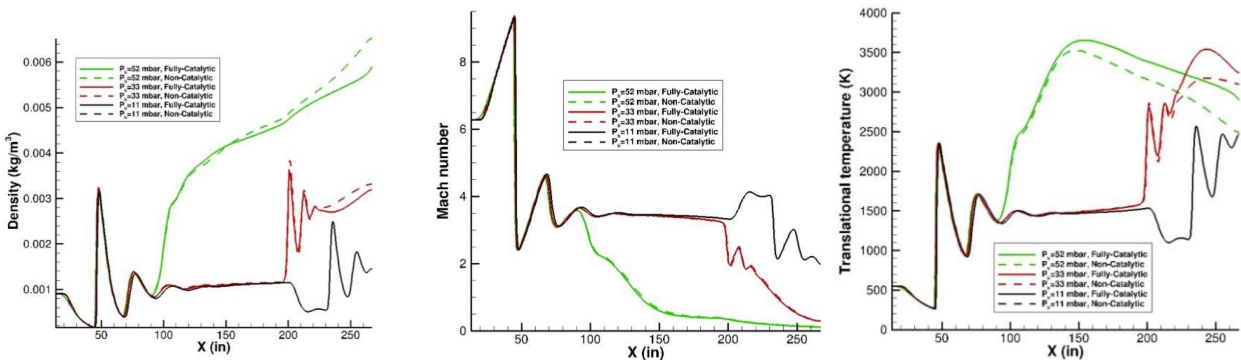

Figure 51: Density, Mach number and Temperature along the diffuser axis from [19], in black the supersonic case

Properties	Air	Water
Density	0.001 kg/m^3	1000 kg/m^3
Velocity	2004.5 m/s	31.3 m/s

Table 5: Properties of the air cross flow at the diffuser exit in supersonic case (i.e. back pressure of 11 Pa) and of the water jet

In this supersonic case, as we would have expected, the momentum ratio q is much lower than the subsonic case, as calculated in equation 29.

$$Momentum\ ratio\ q = \frac{\rho_{water} u_{water}^2}{\rho_{air} u_{air}^2} = 243.8 \tag{29}$$

Many studies have been devoted to formulate empirical correlations for the liquid jet's penetration height in supersonic airstream (Figure 52, left). The expressions for the penetration height are commonly described as functions of the momentum flux ratio, spatial distance from the orifice, and orifice diameter (Figure 52, right).
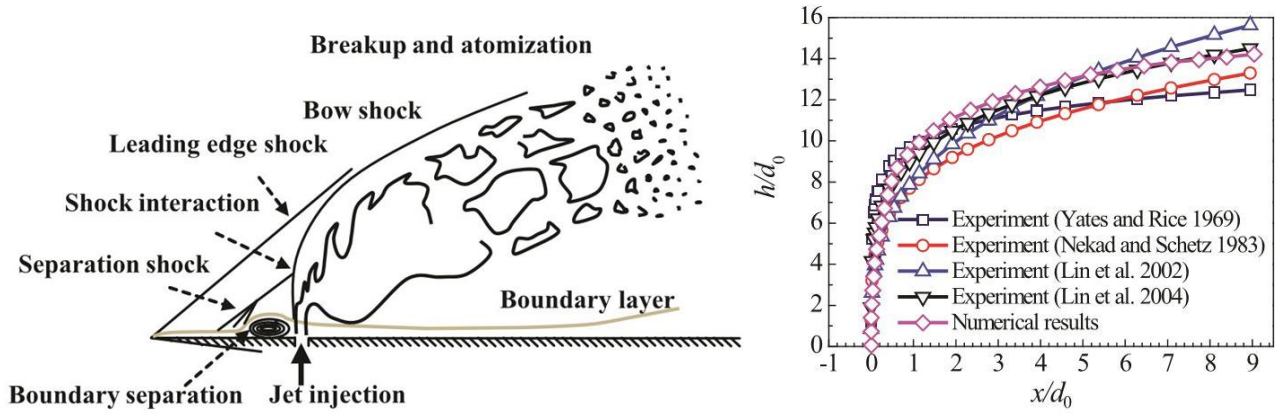

Figure 52: Schematic of liquid jet injection into supersonic flow (left) and comparison for correlations for supersonic cross flow (right) from [27]

If we take the most conservative of these correlations, showed in equation 30, we can calculate our penetration height.

$$\frac{h}{d_0} = 4.73(q)^{0.3}\left(\frac{x}{d_0}\right)^{0.3} \tag{30}$$

The results both for subsonic and supersonic case, with the column trajectory have been calculated and both the two cases allow the flow to reach the diffuser axis before reaching the heat exchanger. At the end, instead of having 4 injectors with D = 2 mm, the high momentum ratio allows us to reduce the diameter of the injectors without affecting the penetration height in order to have a better distribution of injected water: we may have 16 injectors with a diameter of 1 mm. In the subsonic case we have a deviation of 0.54 mm while in the supersonic one we have a deviation of 251.75 mm but we are fine since the heat exchanger tube are at 500 mm from the flange.

The suggested shape of the injection nozzle is, as in [26], a flat-ended ¼" tubing (6.35 mm outer diameter) with the injection hole in the center of the endwall. A taper is provided just prior to injection to smoothen the flow. The injection diameter is of 1 mm with L/D value of 1.5 (Figure 53, left).

At this point further improvements have been considered after being involved in the manufacturing process. In particular we may have 20 Injectors with a diameter of 1 mm straight holes in order to simplify the manufacturing process. Then we may put the injectors in between the main holes of the flange in order to allow an easier manufacturing process (the holes will be done from outside and then a sealant material will be used to fill the holes). Finally let's consider a certain angle of injection θ different from 90° in order to change the penetration height and to guarantee a more uniform water distribution (see Figure 53, right). Following this change in the design, we studied the effect of the angle of injection on the penetration height of the column both in subsonic and supersonic flow conditions. What we used are equation 31 and 32 taken from [28] and [29] and corresponding to the penetration height respectively in subsonic and supersonic air cross flow.

$$\frac{x}{d} = \frac{1}{\pi}\frac{4.4}{\bar{q}\sin^2\theta}\left(1 - \frac{V_j\cos\theta}{u_\infty}\right)^2\left(\frac{y}{d}\right)^2 + \frac{\cos\theta}{\sin\theta}\left(\frac{y}{d}\right) \tag{31}$$

$$\bar{h} = 1.32\,(\bar{q})^{1/2} \cdot \ell n\,(1 + 6\bar{x}_h) \cdot \sin\,(2/3\theta) \tag{32}$$
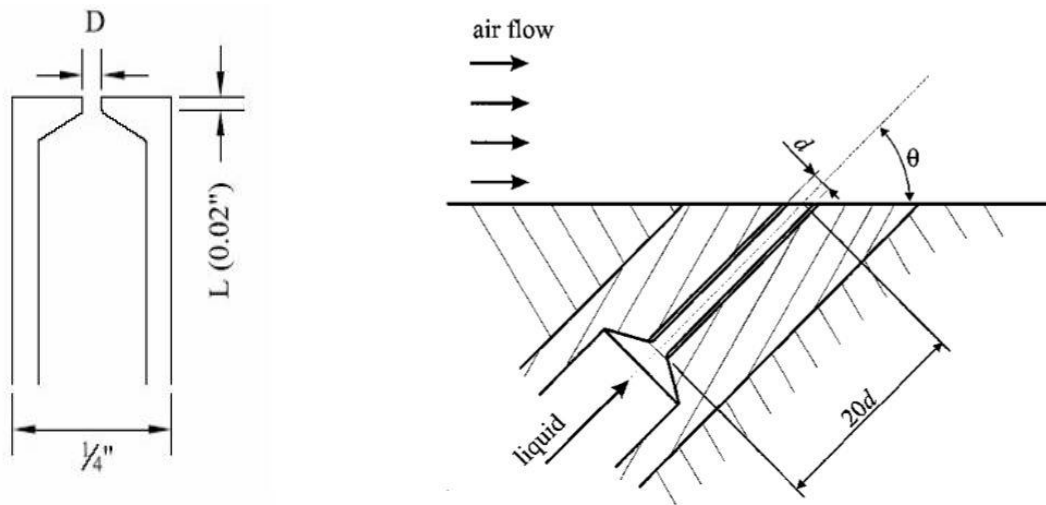

Figure 53: Schematic of selected Injection Nozzle (left) and schematic of the improved situation with a certain angle of injection

Three angles were considered: the normal injection as before which corresponds to a θ of 90°, an downstream injection with a θ of 45°, and an upstream injection with a θ of 135 °. In the subsonic case the flow is practically not deviated from the air flow as we can see from Figure 54.

Figure 54: Column jet trajectory in subsonic air stream for downstream injection (left), normal injection (center) and upstream injection (right), in red there is the diffuser axis, measures are expressed in millimeters.

For the supersonic case, we have to consider that effective diameter of the supersonic flow is almost 1/3 of the diffuser exit diameter (172 mm): the water jet has therefore to penetrate for 86 mm to reach the diffuser axis (Figure 55).

Figure 55: CFD analysis of the diffuser for 11 mbar back pressure (supersonic condition at the end of the diffuser) [19]

From the calculations it' easy to understand that the maximum penetration takes place with an angle θ of 135°, which corresponds to an upstream injection. The column jet trajectory for the upstream (135°) and the normal injection (90°) are shown in Figure 56. With this upstream injection we can reach a penetration of 165 mm at the heat exchanger tubes which is quite above the required value of 86 mm.

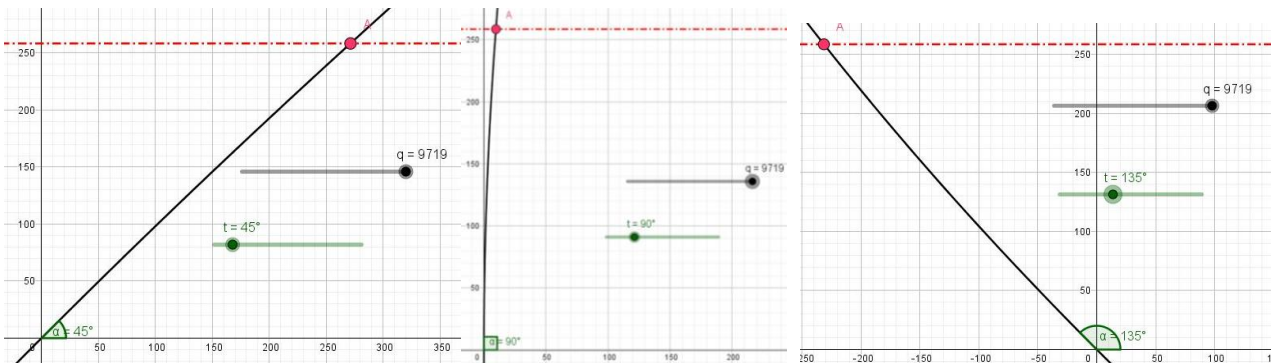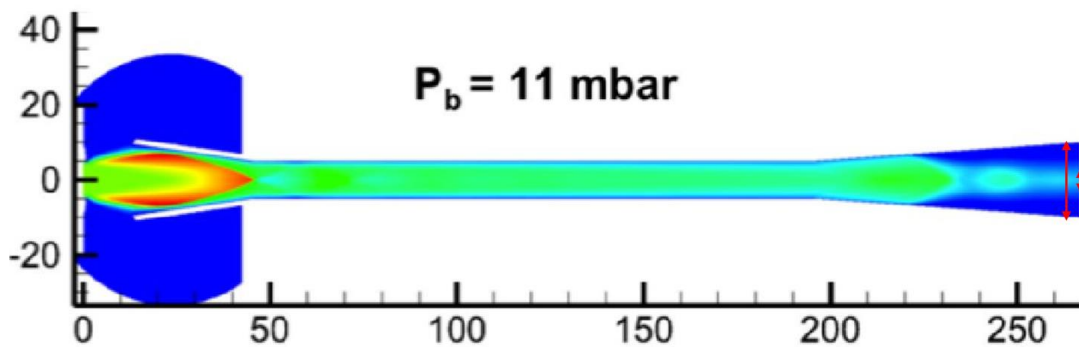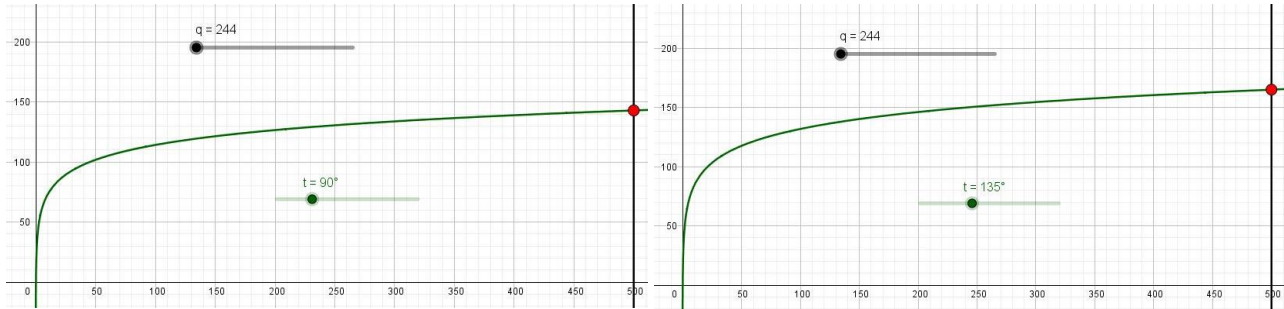*Figure 56: Column jet trajectory in subsonic air stream for normal injection (left) and upstream injection (right), in black the position of the heat exchanger tubes, measures are expressed in millimeters.*

From the above we can assure, with this alternating injection at 90° and 135° a more uniform mixing between the water and the air cross flow also in the supersonic case. At this point we have to check the break point of the column jet in the subsonic case, because the jet can easily go through the air cross flow without being broken by the flow, due to the low Weber number. From our literature review, it turns out that The column breakup process may be divided into two distinct regimes: aerodynamic ($T_b<1$) and non-aerodynamic ($T_b>1$) (see Figure 57). For aerodynamic breakup, the aerodynamic forces associated with the gaseous crossflow accelerate the column in the freestream direction and induce unstable surface waves that ultimately lead to column fracture. For non-aerodynamic breakup, liquid turbulence and liquid inertial forces generate instabilities within the liquid itself and cause large-scale column deformations, which ultimately lead to column fracture [28].

Breakup regime parameter:

$$T_b = \frac{3}{2} \frac{V_j}{u_\infty - V_j \cos\theta} \sqrt{\frac{\rho_j}{\rho_\infty}} We_{fd}^{-\frac{1}{3}}$$

Column fracture height:

$$\frac{y_b}{d} = 2.6 \frac{V_j \sin\theta}{u_\infty - V_j \cos\theta} \sqrt{\frac{\rho_j}{\rho_\infty}}, \qquad T_b < 1$$

$$\frac{y_b}{d} = 1.7 We_{fd}^{\frac{1}{3}} \sin\theta, \qquad T_b > 1$$

Column fracture distance:

$$\frac{x_b}{d} = 9.3 + 2.6 \frac{V_j \cos\theta}{u_\infty - V_j \cos\theta} \sqrt{\frac{\rho_j}{\rho_\infty}}, \qquad T_b < 1$$

$$\frac{x_b}{d} = \frac{9.3}{T_b^2} + 1.7 We_{fd}^{\frac{1}{3}} \cos\theta, \qquad T_b > 1$$

Figure 57: Breakup regime parameter and Column fracture height and distance correlations from [28]

In our case we can calculate a "fluid" Weber number as following from equation 33:

$$We_{fd} = \frac{\rho_j du_j^2}{\sigma} = 13606 \tag{33}$$

For this value we get a breakup parameter of 6.19 for the 90° case and of 5.23 for 135°. These two values are bigger than one and therefore we are in the case of non-aerodynamic breakup mode, as we expected since the dynamic pressure of the air cross flow is quite low. With these numbers we can calculate a column fracture height of 40 mm for the 90° case and of 28.69 mm for 135°: in both cases we can assure a good mixing of the water with the incoming air cross flow.

3.4.   Regular cooling system

The next step in the design process it to compute the required dimensions of the pipes for the regular cooling systems. As a matter of fact, as we have anticipated, the flange requires to be cooled down even if we are not injecting water since the air hot flow is exchanging some heat with the flange walls. To proceed further in our design we need some data/assumptions:

- The flange exchanges heat only with the cooling water
- The maximum Wall Heat Flux at the diffuser exit is 9 W/cm^2 (from Figure 58)
- Minimum specific heat c_p of Water is 4175 J/kg [23]
- The maximum ΔT of the water is 20 K (average actual ΔT is 32 K for the difuser exit segments) [19]
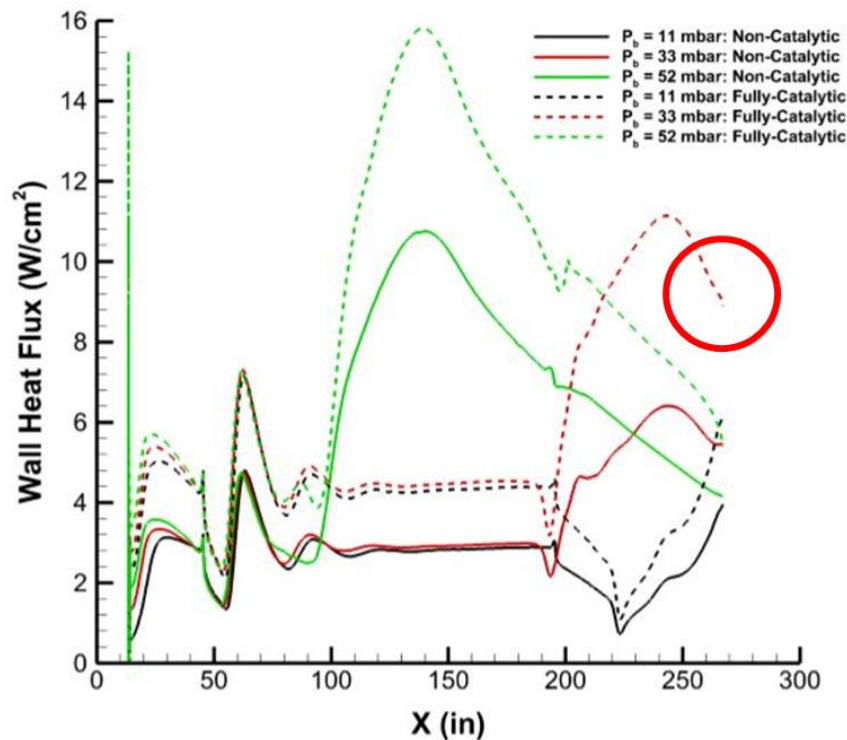
Figure 58: Diffuser Wall Heat Flux Distributions from [19]

Assuming to use one flange ANSI B16.5 CLASS 150 with an internal diameter of 20.35 inches and a thickness of 1.69 inches we have an internal Area of 697.05 cm^2 which means having a flux on the flanges of 6273.5 W. By using the simple enthalpy balance in equation 34 we can calculate a needed mass flow rate. We get a water mass flow rate of 0.075 kg/s and, with a safety factor of 2, we need a mass flow rate of 0.1503 kg/s (for the other flanges of the facility we have a mass flow rate of 0.158 kg/s) [19].

$$Q = \dot{m}c_p\Delta T = 6273,5 = \dot{m} * 4175 * 20 \tag{34}$$

Therefore, we have that the needed water mass flow rate is of 0.1503 kg/s, the total pressure is 9 atm with ΔP of 20 kPa [19] and we can assume a discharge coefficient of 0.61 (C_d used for the actual diffuser cooling system). We can calculate the velocity of the cooling water flow as in equation 35:

$$vliq = Cd\sqrt{\frac{2\ \Delta P}{\rho}} = 0.61\sqrt{\frac{2*20*10^3}{1000}} = 3.858\ m/s \tag{35}$$

Since $\dot{m} = \rho v A$, we can calculate a total required Area of 3.896 x 10^{-5} m^2 which means having a single pipe with a diameter of 7.05 mm or 2 pipes with a diameter of 4.98 mm each. The required dimensions appear to be very small if compared to the other cooling flanges: let's adopt the channel geometry of the flange III-F-01.

3.5.   Design Proposal

At this point we are ready to show the design proposal that we have designed, a summary of the considered data is provided below:

- We use a standard ANSI B16.5 CLASS 150 flange with an internal diameter of 20.35 inches and a thickness of 1.69 inches
- The needed injected water mass flow rate is of 0.3612 kg/s
- We have 20 injectors with a diameter of 1 mm, with an alternating path 90° and 135°, in between the main holes of the flange
- The needed water mass flow rate for regular cooling is of 0.1503 kg/s
- The dimensions of the regular cooling channel are adapted to put a bigger o-ring channel
- Material used is 6061-T6

What we have to check before designing the minimum material thickness of the flange for the pressure design. As a matter of fact, between the two pipes (one for water injection and one for regular cooling system) we may have, in normal operation, a difference of pressure of 10 atm. The data used are:

- Young's Modulus is 69 GPa
- The fatigue limit for 500M completely reversed cycles is 97 MPa
- The maximum ΔP is 10 atm
- The ring of division is assumed to be a rectangular plate of 19,05 mm x 1795,42 mm

The formula for calculating the required thickness for rectangular plate is showed in equation 36 (see section on pressure window design for further references):

$$t = l \cdot w \cdot \sqrt{\frac{P \cdot K \cdot SF}{2 \cdot M \cdot (l^2 + w^2)}} \tag{36}$$

The minimum thickness of the division ring is about 3 mm with a safety factor of 4 and we will have a maximum stress of σ_m= 21.57 MPa and a maximum displacement of y_m= 0.002 mm.

We can check now the dimensions of the pipes for both the regular cooling system and for the injections of water using a very low discharge coefficient of 0.5 for safety reason. For the water injection system, the water mass flow rate is of 0.3612 kg/s, the ΔP is 10 atm and hence the velocity of the injected water is 22.36 m/s. Since $\dot{m} = \rho v A$, we can calculate a total required Area of 1.62 * 10^{-5} m^2 which means having a single pipe

with a diameter of 4.54 mm or 20 injectors with a diameter of 1 mm each as in our design. The injectors will have an alternate path: one at 90° and one at 135° to guarantee a more uniform distribution.

For the regular cooling system, the water mass flow rate is of 0.1503 kg/s, the Total Pressure is 9 atm with ΔP of 20 kPa and hence the velocity of the cooling water flow is 3.16 m/s. Since $\dot{m} = \rho v A$, we can calculate a total required Area of 4.76 x 10^{-5} m^2 which means having a single pipe with a diameter of 7.79 mm but, in our design, we have two pipes and for each of them the equivalent diameter is of almost 12 mm. In the end the dimensions of the proposed design appear to be good and large enough also considering a discharge coefficient of 0.5. In the following figures we present the rendering for the proposal design of the flange done by using the Dassault Systems CATIA V5R20 CAD software [30].
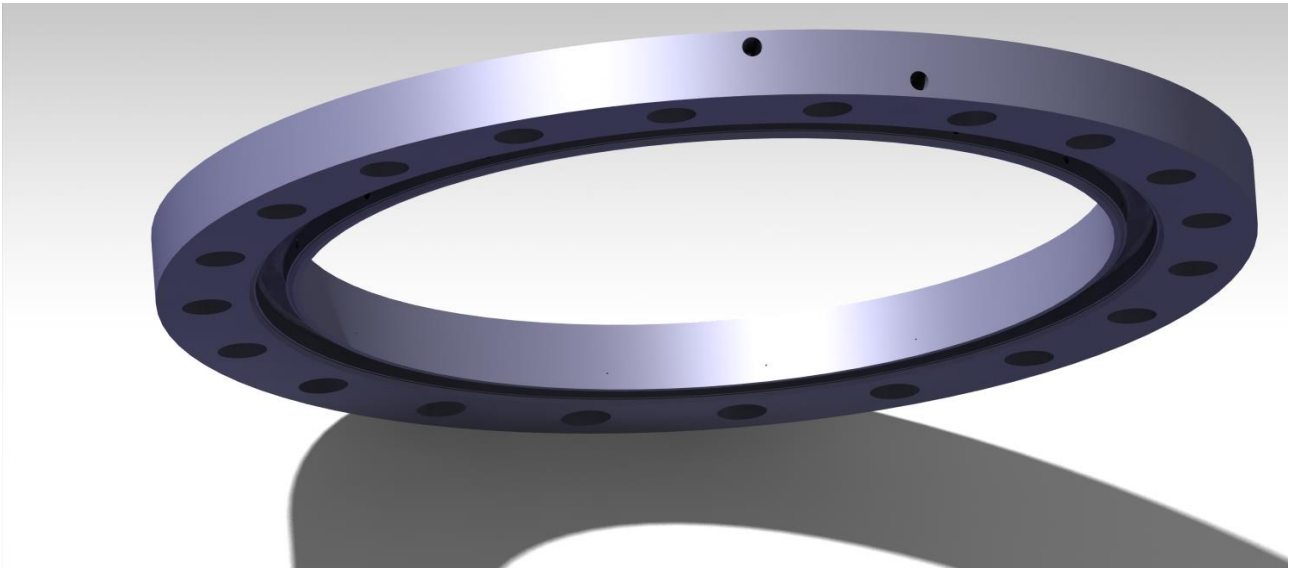

Figure 59: Design Proposal for the emergency flange (3D CATIA rendering): notice the two holes for the regular cooling system and for the injection of water
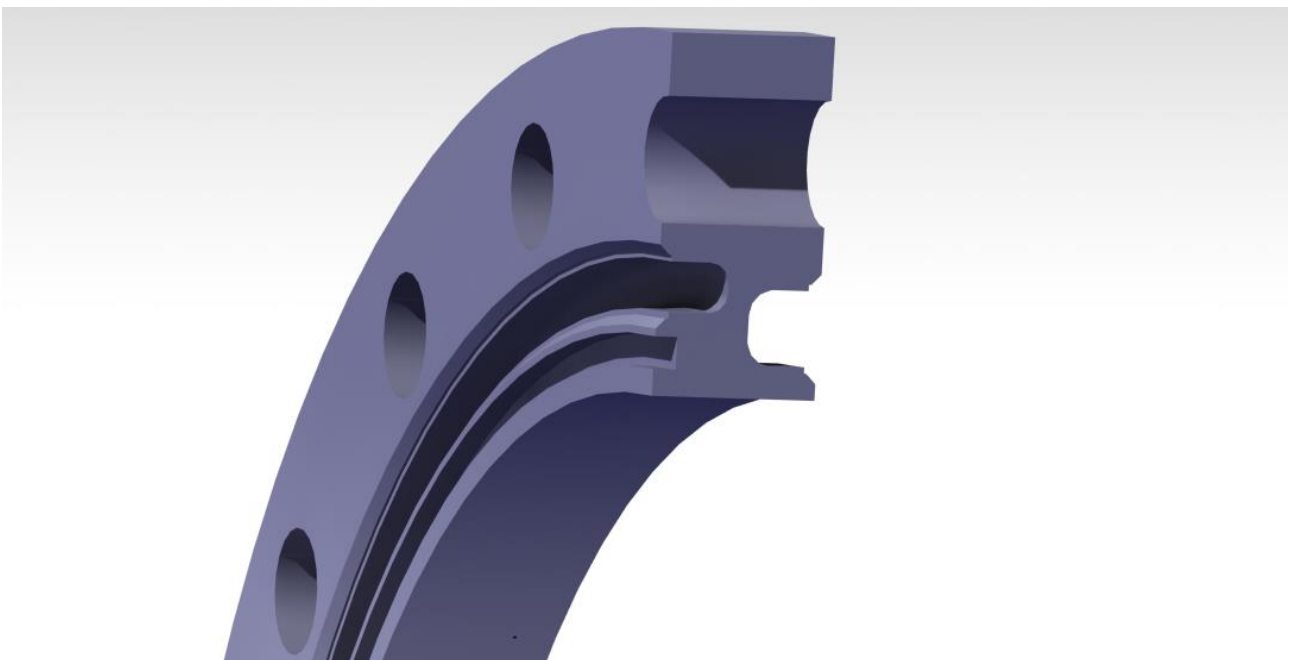

Figure 60: Design Proposal for the emergency flange (3D CATIA rendering): regular cooling systems channel and o-ring at the heat exchanger side
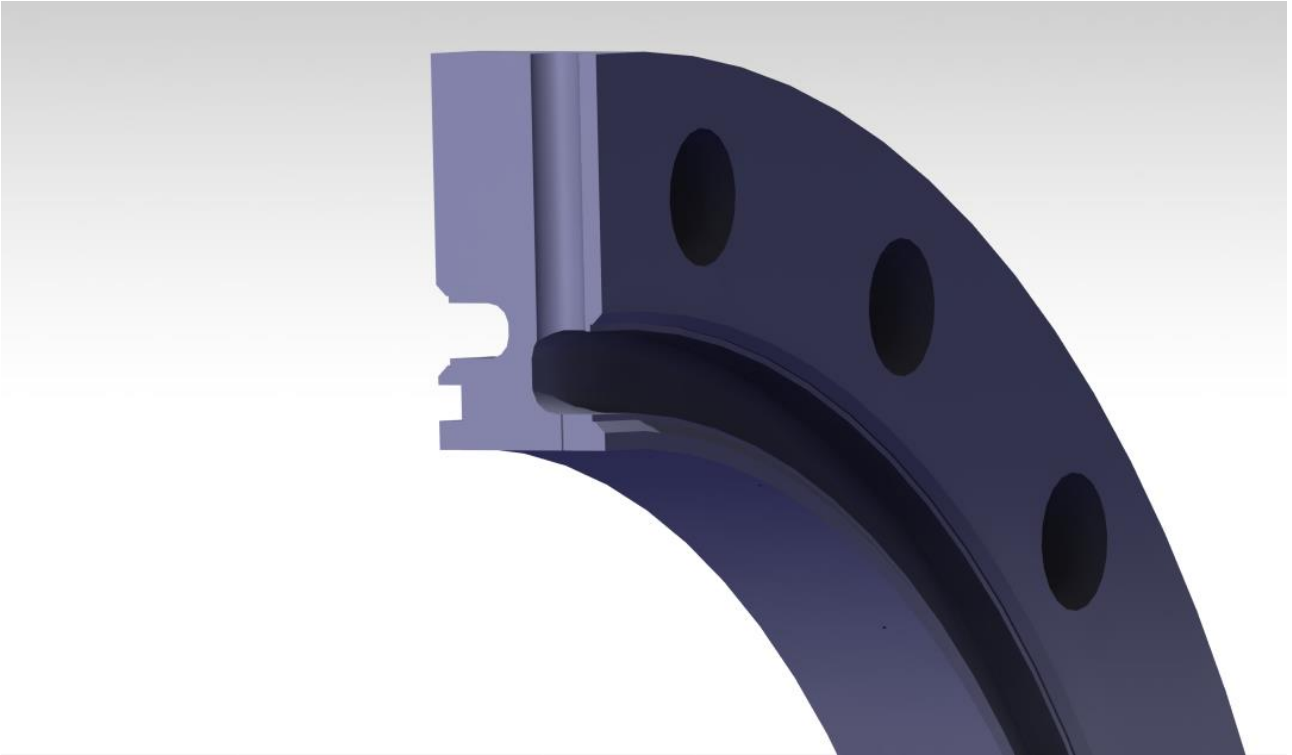
Figure 61: Design Proposal for the emergency flange (3D CATIA rendering): channel for water of at the diffuser side, notice the injection nozzle with ϑ of 90°
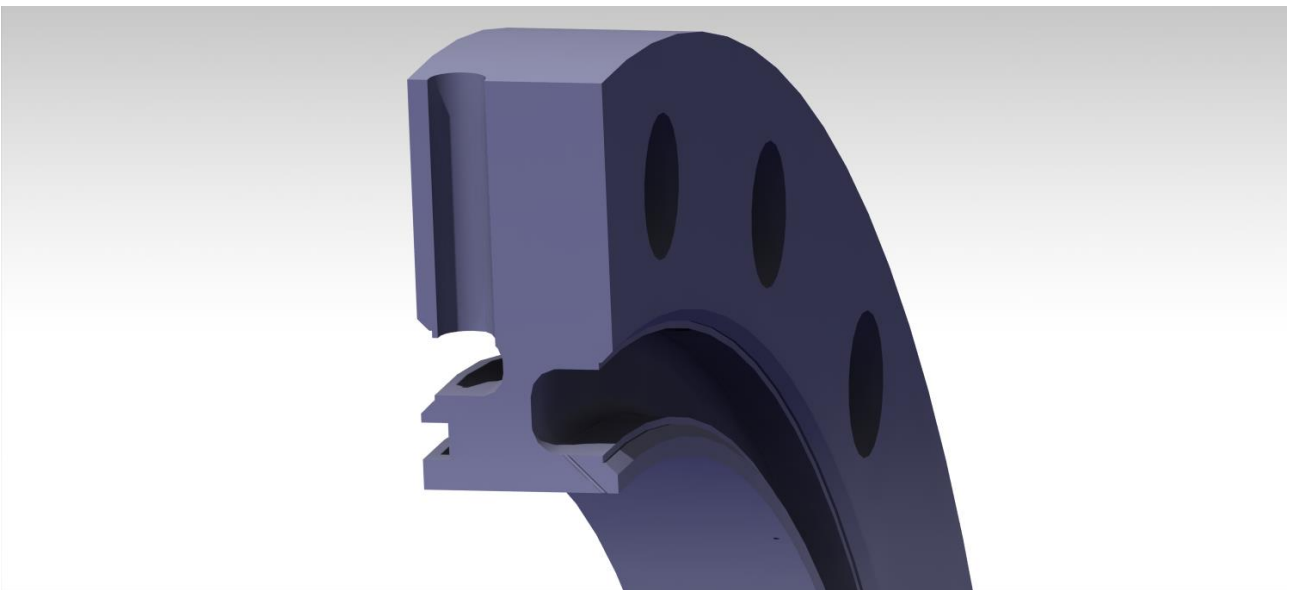
Figure 62: Design Proposal for the emergency flange (3D CATIA rendering): channel for water of at the diffuser side, notice the injection nozzle with ϑ of 135° (upstream injection) and the hole for the cooling water flow

The two channels must be sealed by two aluminum crowns which have to be welded on the channels. In Figure 63 we present a 2D drawing of the flange. The two aluminum crowns have a simple geometry complementary to the channels ones.
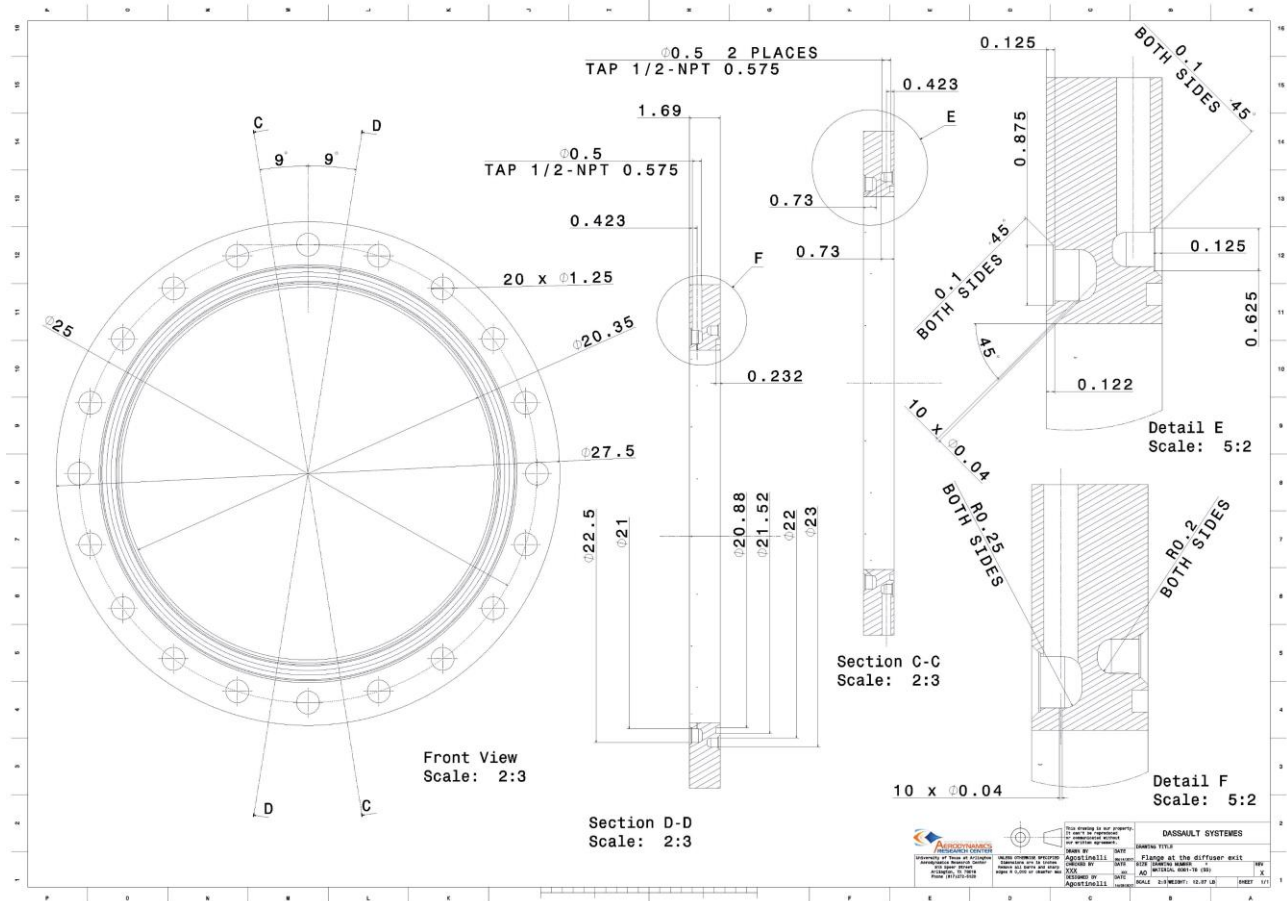
Figure 63: Design Proposal for the emergency flange (2D CATIA technical drawing)

3.6. FEM Analysis

The last task of this design is the FEM analysis of the flange. As a matter of fact, this is a really important task because we have to be sure that our design can withstands the pressure loads without rupture or without being excessively deformed. The structural analysis was carried out by using the Finite Element analysis component provided by CATIA [30].

The material properties used in the analysis are the standard ones provided by CATIA for a general aluminum and that well approximate the 6061 T6 material that we want to use:

- Young modulus: 70 GPa
- Poisson modulus: 0.346
- Density = 2710 kg/m^3
- Elastic limit = 95 MPa

Besides these properties, we have to select the constraints and the loads on the structure. In particular, for what regarding the constraints we have that the main holes faces are fixed (not allowed to rotate or move). For what regarding the loads, we have a pressure load of 10^6 Pa on the faces of the channel for the flange regular cooling (due to cooling water flow) and a pressure load of 10^5 Pa on the external faces of the flange (due to atmospheric pressure since inside the diffuser we have almost vacuum). This situation is showed in Figure 64, 65 and 66.
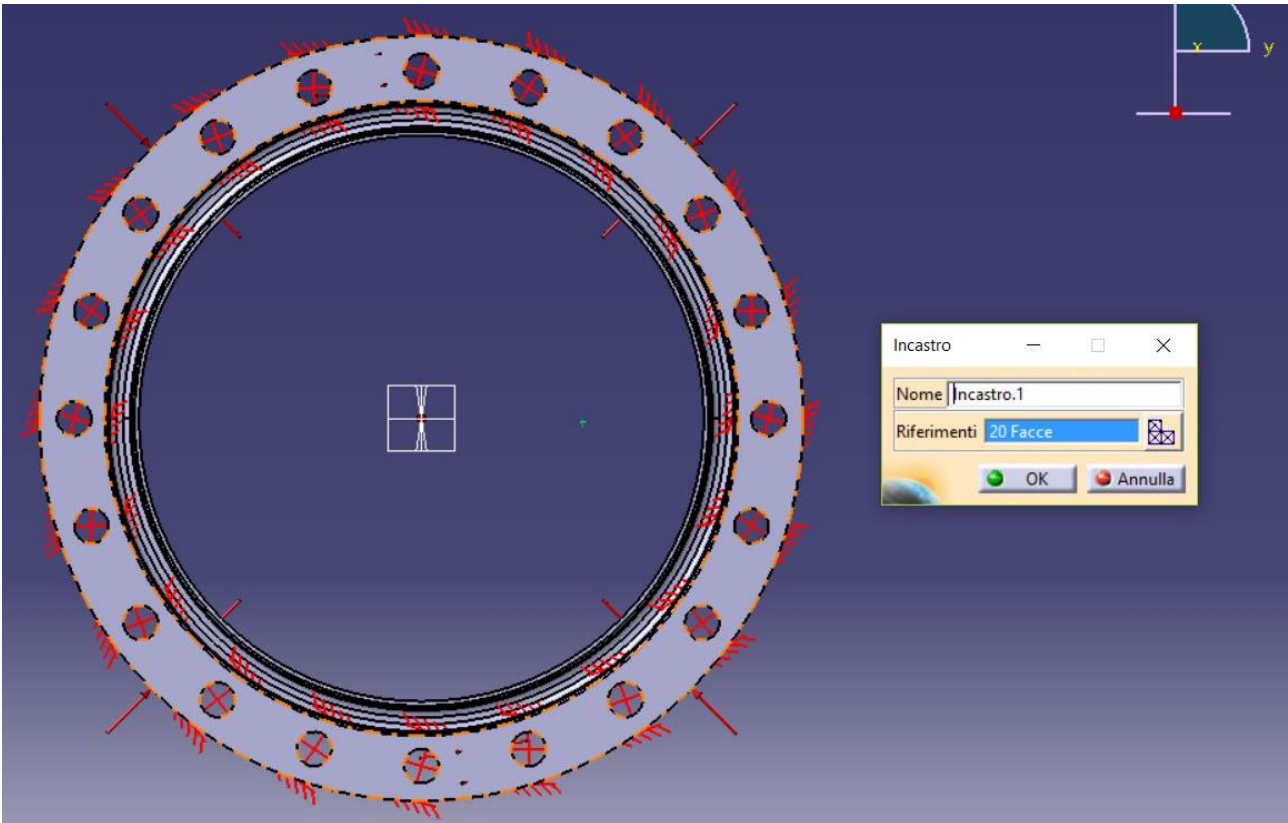
Figure 64: Constraints for the FEM analysis of the flange, main holes faces are fixed (not allowed to rotate or move)
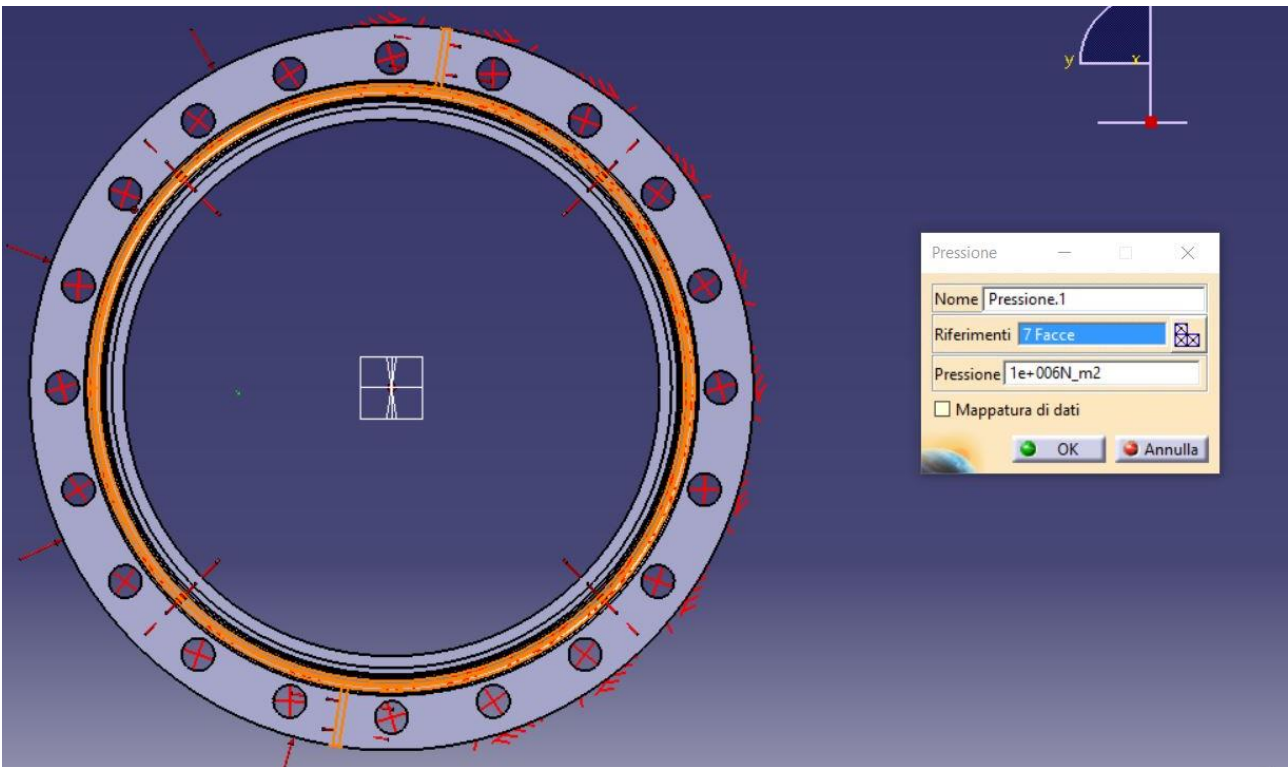
Figure 65: Loads for the FEM analysis of the flange, pressure load of 10^6 Pa on the faces of the channel for the flange regular cooling
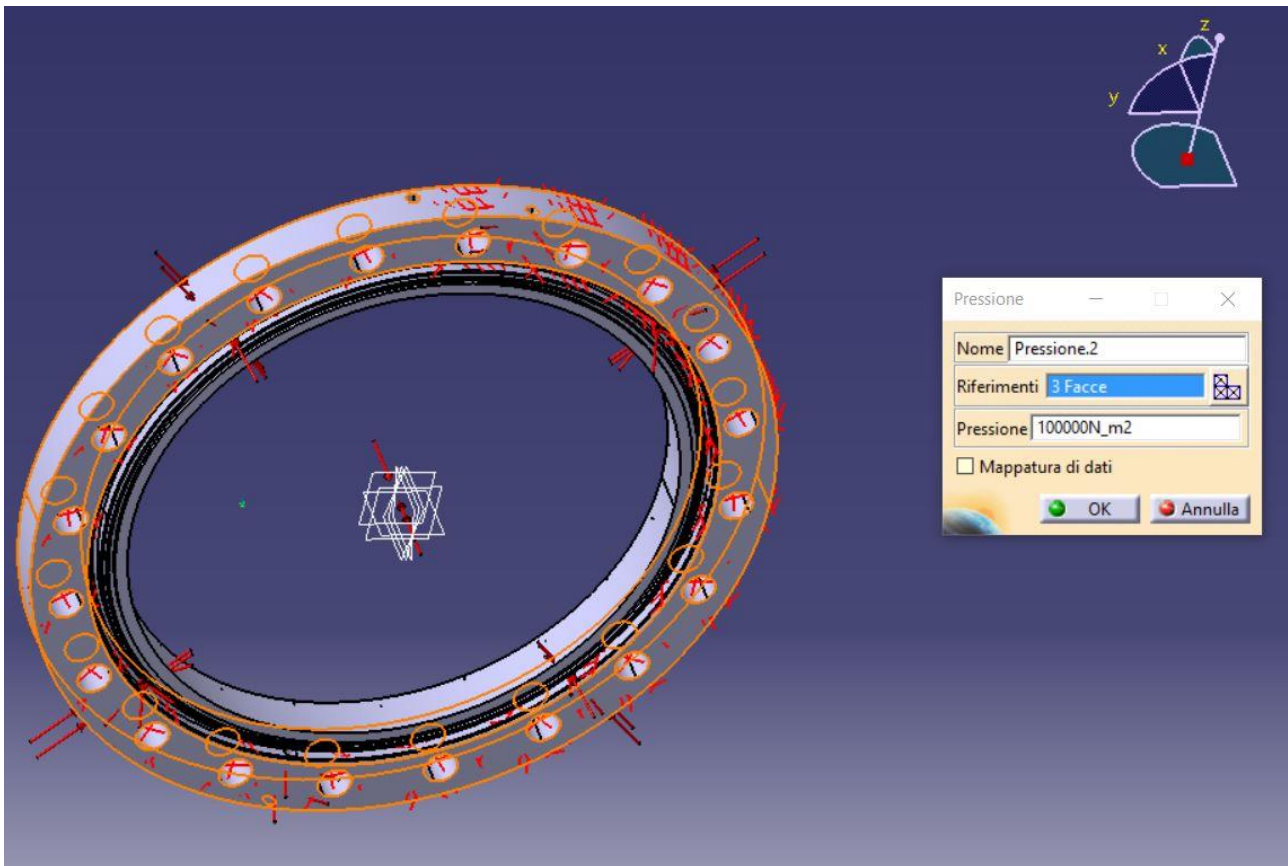
Figure 66: Loads for the FEM analysis of the flange, pressure load of 10^5 Pa on the external faces of the flange

The first mesh used was quite coarse in order to understand the type of deformation which can happens. The calculated deformation with an amplification factor of 2000 is showed in Figure 67.
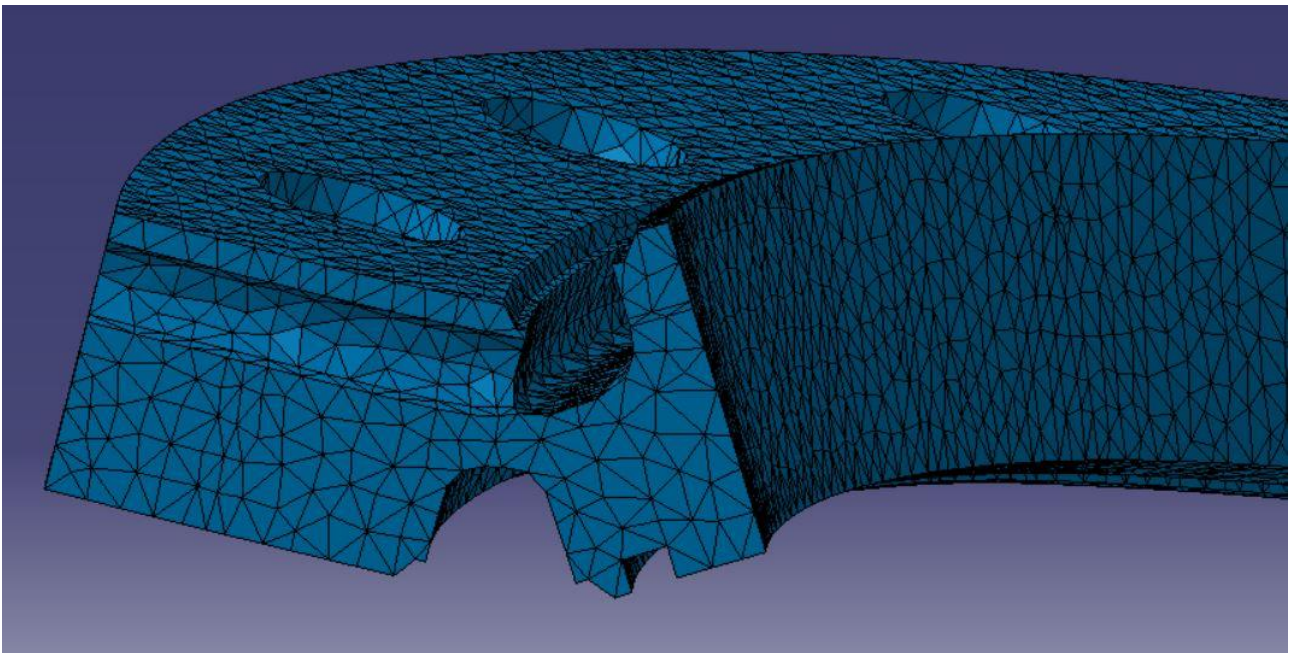
Figure 67: FEM analysis of the flange, deformation with an amplification factor of 2000, coarse mesh

The number of cells is then gradually increased until convergence and independence of the results on the mesh parameters was achieved.

In Table 6 we show the results that we obtained with the different meshes used.

Mesh	Dimension of cells	Number of cells	Max. displacement	Max. stress
Mesh 1	0.2 in	264032	0.00038 in	9.29 MPa
Mesh 2	0.1 in	1430425	0.00051 in	14.4 MPa
Mesh 3	0.08 in	2301021	0.00055 in	15.4 MPa
Mesh 4	0.07 in	2775397	0.00056 in	16 MPa

Table 6: Results of the FEM analysis of the flange for coarse to fine mesh.

At the end, the variation of mesh 4 respect mesh 3 is, for the maximum stress, a +3,9 %, while for the maximum displacement, it is a +1.8%. Independence from mesh is therefore achieved: the maximum stress (16 MPa) is well below the maximum allowed one (95 MPa) and also the maximum displacement is very low and equal to 0.00056 inches (i.e. 0.014 mm).

In the following Figures 68, 69 and 70 we present the results for the finest mesh (number 4) that we have used.

At the end of our discussion we can assert that the design proposal can largely sustain the pressure loads to the atmospheric pressure and due to the high pressurized water flow for the regular cooling systems. Furthermore, we have seen during our previous discussion, that the design of the pipes is correct in terms of dimensions and that also the injection of water is properly accomplished by the injection nozzles thanks to their well-defined position, orientation, dimensions and shape.
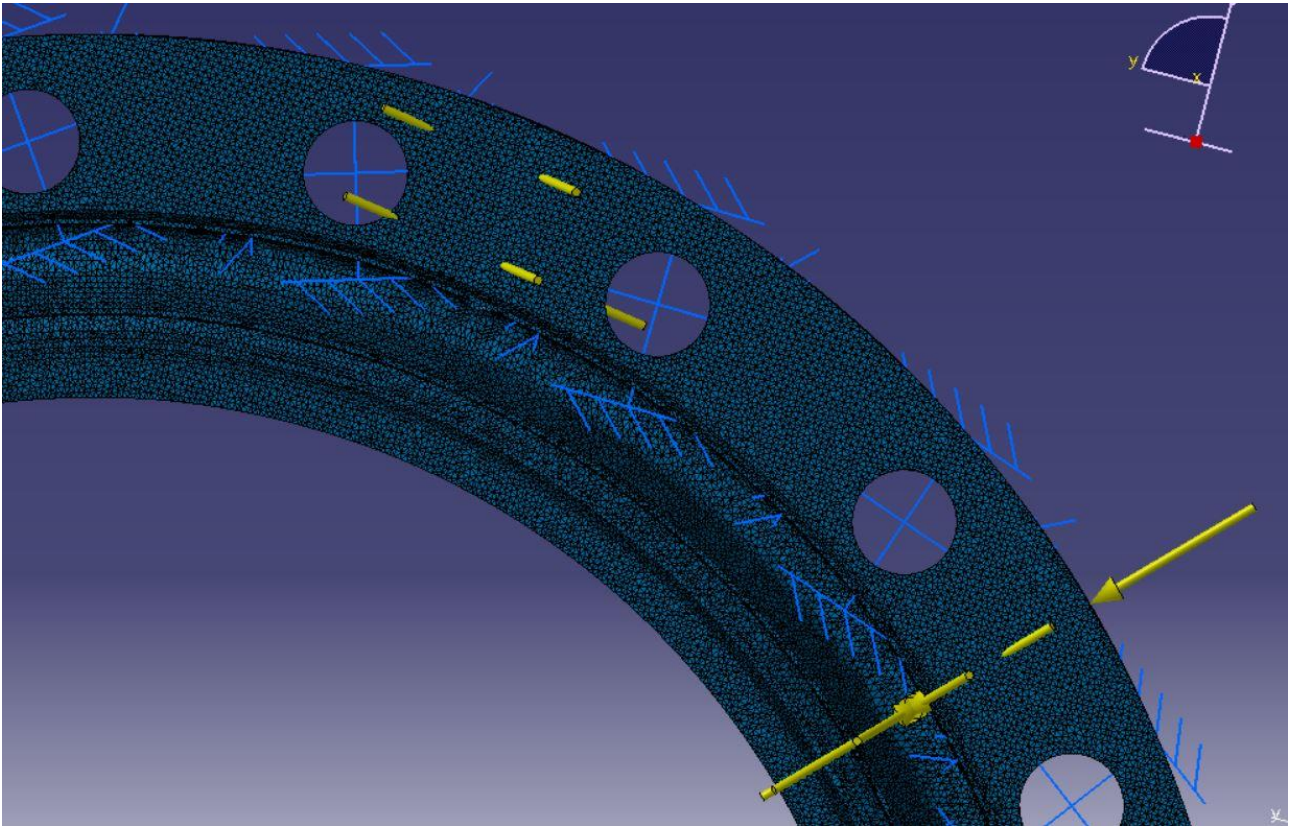

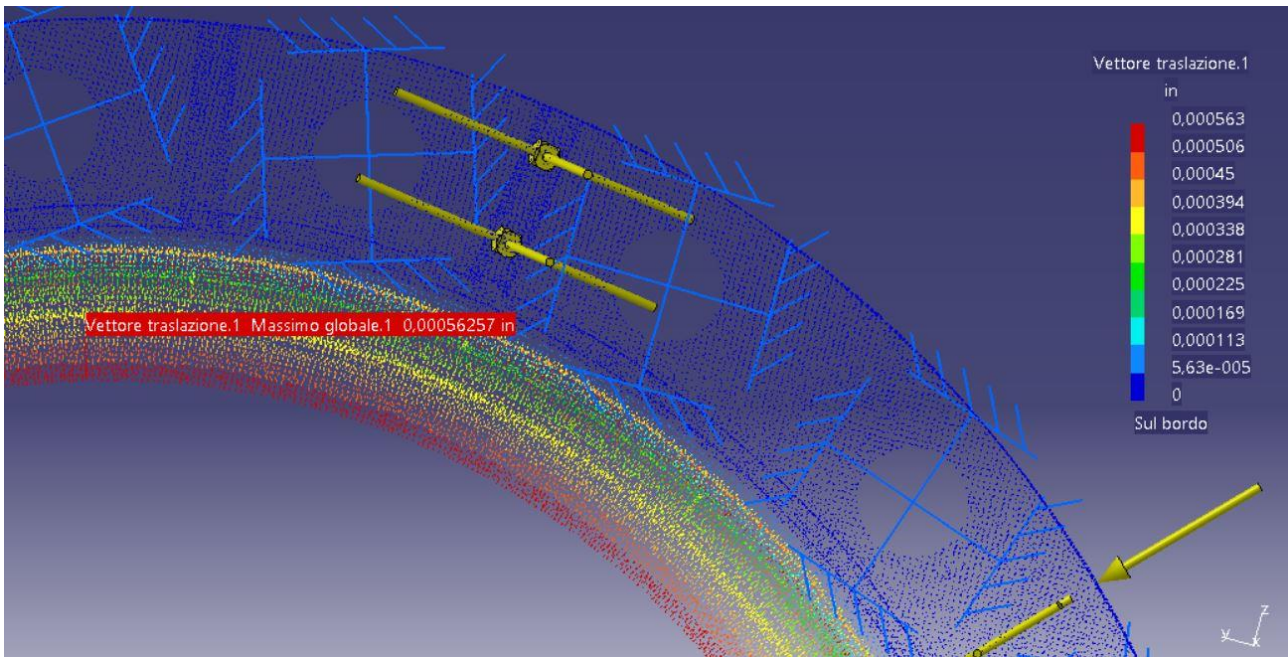*Figure 68: FEM analysis of the flange, fine mesh 4*

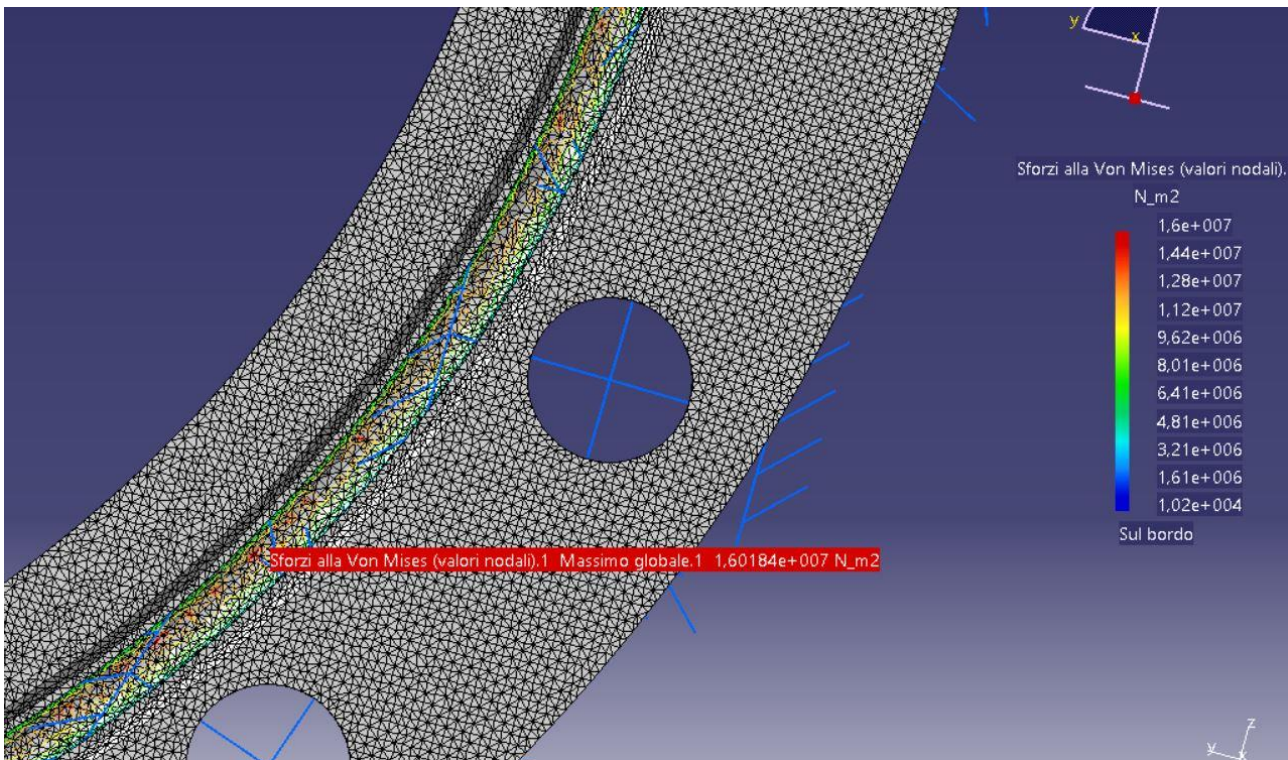*Figure 69: FEM analysis of the flange, magnitude of the displacements, mesh 4*

Figure 70: FEM analysis of the flange, Von Mises stresses, mesh 4

4.   Design of the test chamber windows

4.1.   Definition of the Requirements

The task proposed is to design the test chamber windows for the new Hypersonic Wind facility. The test chamber in fact, which was already under construction during my internship, includes only a blank flange to guarantee vacuum conditions inside the test chamber but no windows had already been designed. This blind flange of which I have only the total dimensions has to be substituted by the windows: in total we have three windows for the Plasma Wind Tunnel test chamber (Figure 1).

The design of this flange passes through a first selection of the material which we want to use and that we have to select in base of their optical, mechanical and thermal properties. Moreover we have to decide the dimensions of the windows and to check if the whole assembly can withstands the pressure loads: as a matter of fact we have almost vacuum inside the test chamber and the atmospheric pressure on the other side.

The first point is however to define the requirements of the windows in terms of optical, mechanical and thermal properties. In particular, the basic idea is to have windows that would allow to do laser experiments, infrared and ultraviolet measurements and also that, at least at the beginning, allow to simply see the flow. We can summarize these properties as the following optical properties:

- Transparent to Visible Light
- Transparent to InfraRed
- Transparent and resistant to Laser (532 nm, 0.8 J for pulse, 20 Hz max)

For what regarding the thermal properties, we are looking for:

- Low thermal conductivity (i.e. for the safeteness of operators)
- Low thermal expansion
- Temperature of phase change (i.e. softening temperature) higher than the Temperature of the test chamber walls

We need also a window that fulfill some chemical requirements:

- Resistant to atomic-oxygen (e.g. the hot flow is highly dissociated)
- Compatible with the in-contact material

Once we have selected a certain type of glass we can go further and check the mechanical properties:

- Resistance to 1 atm of Gauge Pressure
- Certain degree of hardness

At this point we can calculate the required thickness of the glass that can withstands the pressure load for the area of the windows that we need; the question now is: are we satisfied? If the answer is no, we have to go back and select another type of glass which probably do not fulfill all the initial requirements but that probably has better mechanical properties. This discussion demonstrates that the design process is an iterative process in which all the different requirements must be fulfilled in a sort of least squares algorithm in order to find the optimum trade off.

4.2. Material selection

The selection of the material, for what we have explained before, is the most important (and difficult) task. We started with a study of all the type of glasses and of their properties [31]. The classification of glasses is usually done in a diagram in which we identify the refractive index (commonly defined at the Helium d line, 587.6 nm) and the Abbe number (i.e. the inverse of relative dispersion). An example of this chart is showed in Figure 71 from [31]. In this Figure we have different notations:

- $n_d > 1.60$, $v_d > 50$ or $n_d < 1.60$, $v_d > 55$ are called "crown" (K) glass; other glasses are called "flint" (F)
- "Light" or "dense" indicate the relative amounts of heavy metal oxides such as PbO or La2O3
- U or IR denote extended ultraviolet or infrared transmitting glasses
- LG- laser glass
- FR- Faraday rotator glass
- AO - acoustooptic glass
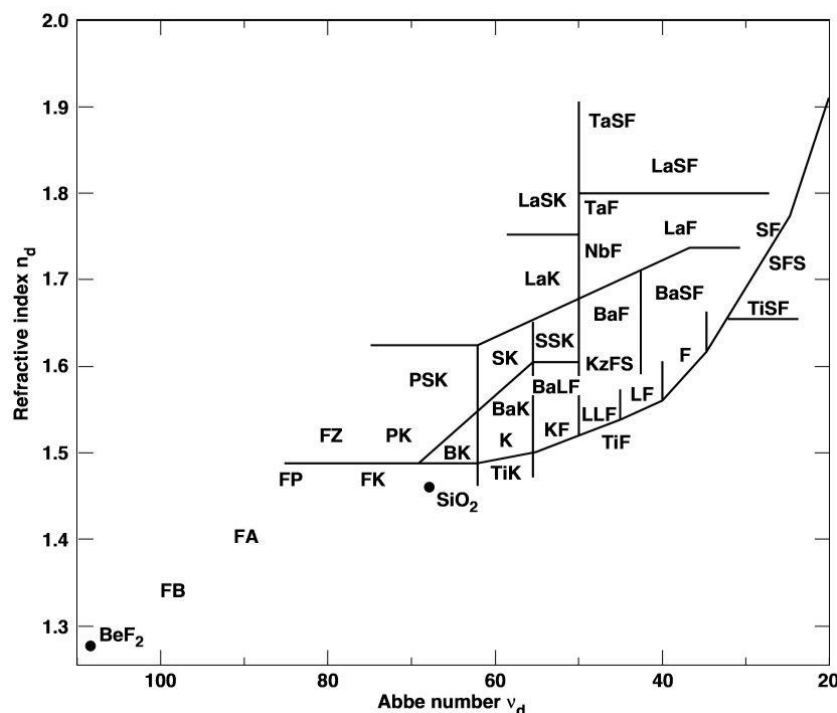
Figure 71: Classification of different types of glasses [71]

What we are interesting the most is however the so called optical density, strictly linked to the absorption coefficient and of the thickness of the glass, as in the following equation 37 where α is the absorption coefficient, l is the length, I/I_0 is the transmission and OD is the optical density:

$$\alpha l = \ln(I_0/I) = 2.303 OD \qquad (37)$$

The fact that glasses are dispersive means that their optical properties change with the frequency of the light. As a matter of fact, the optical density (i.e. the absorption coefficient) changes with the light frequency which passes through the glass and this causes a certain type of glass to be transparent to a certain band of light frequencies more than another band. In Figure 72 we present the transmission coefficient for representative optical glasses in the infrared (left) and ultraviolet (right) absorbed edge. It's evident that the transmission coefficient is a quantity which depends on the thickness of the samples: the thinner is the glass the more transparent it is. Therefore, we can select a certain glass only if we have already the required thickness, but the latter depends on the glass mechanical properties: here we have again the iteration process.

Figure 72: Infrared (left) and Ultraviolet (right) absorption edge of representative optical glasses, sample thickness of 2 mm [31]

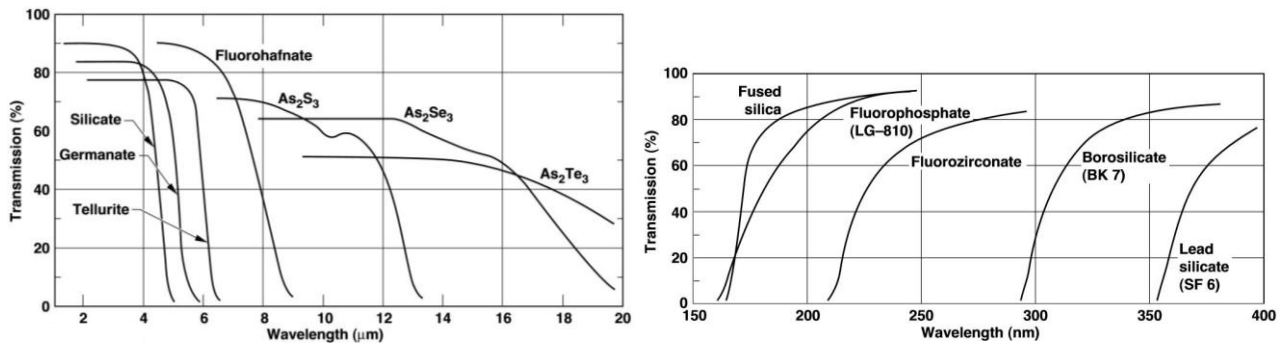We have looked for different types of glasses and products available in different dimensions and produced by different companies. In Table 7 we present some of the Laser Line Windows with a design wavelength (DWL) of 532 nm. In Table 8 we present also some Windows for UV - V - IR measurements.

In Table 7 we have indicated the name of the company, the name of the product and the reflection at the design wavelength (i.e. 532 nm). Moreover, we have indicated also the maximum diameter and thickness that is commercialized by the company: if a bigger window is required we may ask for a customized production. The important characteristic here is the damage threshold that the glass can withstand. The last column provides the prices for each product.

Company	Product	Reflection @ DWL	Max D	Thickness	Damage Threshold	Price Max
Edmund Optics	Laser V-Coat, λ/20 Fused Silica Window	~ 0%	50.0 mm	3.0 mm	10 J/cm^2 @ 10ns, 532nm	$ 285.00
Edmund Optics	λ/4 N-BK7 Window	< 0.25%	50.0 mm	4.0 mm	Low power	$ 67.70
EksmaOptics	UVFusedSilica, 532 nm 222-1503M	< 0.25 %	50.0 mm	12.0 mm	10 J/cm^2, 8 nsec pulse	$ 253.00
EksmaOptics	BK7, 532 nm 222-0503M	< 0.25 %	50.0 mm	12.0 mm	5 J/cm^2, 8 nsec pulse,	$ 163.00
NewPort	20QW20-2 Excimer Grade UV Fused Silica V-coat	< 0.25 %	50.0 mm	3.0 mm	10 J/cm², 10 ns pulses	$ 285.00

Table 7: Laser Line Windows products by different Companies, DWL of 532 nm

For the laser window we have chosen a UV Fused Silica glass for UV and Laserline applications. UV Grade Fused Silica is synthetic amorphous silicon dioxide of extremely high purity providing maximum transmission from 195 to 2100 nm. This non-crystalline, colorless silica glass combines a very low thermal expansion coefficient with good optical qualities, and excellent transmittance in the ultraviolet region. Transmission and homogeneity exceed those of crystalline quart without the problems of orientation and temperature instability inherent in the crystalline form. It will not fluoresce under UV light and is resistant to radiation. For high-energy applications, the extreme purity of fused silica eliminates microscopic defect sites that could lead to laser damage. This type of glass is therefore designed to work with high energy lasers: these optics are precision polished, select grade fused silica coated with hard refractory multilayers for very high damage threshold.

For the UV – V – IR measurements, we have selected three types of glasses: the Zinc Selenide, the Zinc Sulfide and the Sapphire Windows.

The Zinc Selenide is ideal for thermal imaging since it has low IR absorption and is transparent across a very wide 600 – 16000 nm spectral range. This is advantageous for thermal imaging where temperatures of remote objects are ascertained via their blackbody radiation spectrum. Long wavelength transparency is

crucial for imaging room temperature objects, which radiate at peak wavelength of approximately 1000 nm with very low intensity. At UTA they have already a glass of this type of circular shape and 6 inches of diameter; our design proposal will therefore take into account the existence of this type of glass that we want to use again.

The Zinc Sulfide has low absorption and scatter properties over its broad transmission range of 400 – 12000 nm. It is a chemically vapor deposited material which is commonly used in thermal imaging. With its excellent transmission properties in the visible and infrared, it is the material of choice for systems that have both visible and mid-wave or long-wave infrared sensors. Moreover, it is slightly harder and more chemically resistant than zinc selenide: our best choice is therefore this zinc sulfide.

Sapphire windows are highly tolerant of extreme temperature and pressure differences. These windows are in fact commonly used as viewports enable viewing inside of vacuum chambers or chambers containing high temperature plasma (as in our case). It has also a wide transmittance range, being transparent across a wide wavelength range from 170 to 5500 nm. This type of glass is the best choice if we want to design a very big window.

Company	Product	Range (nm)	Max D	Thickness	Info	Price Max
Edmund Optics	VIS-NIR Coated λ/10 Fused Silica Window	400 - 1000	50.0 mm	5.0 mm	5 J/cm^2 @ 532nm, 10ns	$ 164.00
Edmund Optics	NIR I Coated λ/10 Fused Silica Window	600 - 1050	50.0 mm	5.0 mm	7 J/cm^2 @ 1064nm, 10ns	$ 164.00
Edmund Optics	Uncoated λ/10 Fused Silica Window	200 - 2200	50.0 mm	6.0 mm		$ 175.00
Edmund Optics	VIS-NIR Coated λ/4 N-BK7 Window	400-1000	75.0 mm	4.0 mm	5 J/cm^2 @ 532nm, 10ns	$ 134.50
Edmund Optics	Uncoated, BOROFLOAT® Window	350 – 2000	200.0 mm	6.5 mm	High T resistant (Tg 530 C)	$ 67.50
Edmund Optics	Uncoated, Ge Window	2000 – 14000	75.0 mm	5.0 mm	T below 100°C	$ 825.00
Edmund Optics	Uncoated, Magnesium Fluoride Window	120-7000	50.0 mm	3.0 mm	resistant to chemical, mechanical shock	$ 540.00
Edmund Optics	Uncoated, Metalized Sapphire Window	200 - 5500	25.0 mm	2.3 mm	Edges: Chrome, Nickel, and Gold	$ 205.00
Edmund Optics	Uncoated, Sapphire Window (Al_2O_3)	200 - 5500	75.0 mm	2 mm	High T, P, or vacuum and corrosive env.	$ 650.00
Edmund Optics	Uncoated, Zinc Sulfide Cleartran Window	400 - 12000	76.2 mm	6.0 mm	Hard and chemically resistant	$ 1295.00
EksmaOptics	CaF2 Windows IR Grade 530-6756	200 - 8000	70.0 mm	Max 10.0 mm		$ 253.00
EksmaOptics	Sapphire (Al2O3) Windows 550-7503	150 - 6000	50.0 mm	3.0 mm	Chemically inert and insoluble	$ 182.00
EksmaOptics	Zinc Selenide (ZnSe) Windows 560-6766	600 – 22000	76.2 mm	6.4 mm	**Actually used for 1500-14000 IR**	$ 1095.00
NewPort	SAW32 Sapphire Window	150 – 5000	75.0 mm	2.0 mm	High T, P, or vacuum environments	$ 729.00
NewPort	MGW13 Magnesium Fluoride window	150 - 6500	50.0 mm	3.0 mm	high resistance to thermal shock	$ 649.00
NewPort	Zinc Selenide windows ZNW17AR.20	3000-12000	74.9 mm	6.0 mm	high resistance to thermal shock	$ 2039.00

Table 8: Windows glasses for UV - V - IR measurements by different Companies

Since we have already available at UTA Zinc Selenide glass for IR measurements we have to take care only of the Laser Window and of the Visible and Ultraviolet measurements. Our choice is therefore to use a UV Fused Silica glass for the laser application and a Sapphire Windows for the UV - V applications.

4.3.   Design Proposal

Our design proposal should take into account the required thickness of the windows, and so the mechanical properties of the selected materials. In order to design a pressure window several references have been investigated [32, 33, 34, 35]. All of them suggest to use some simple formula to calculate the required thickness (see Figure 73).
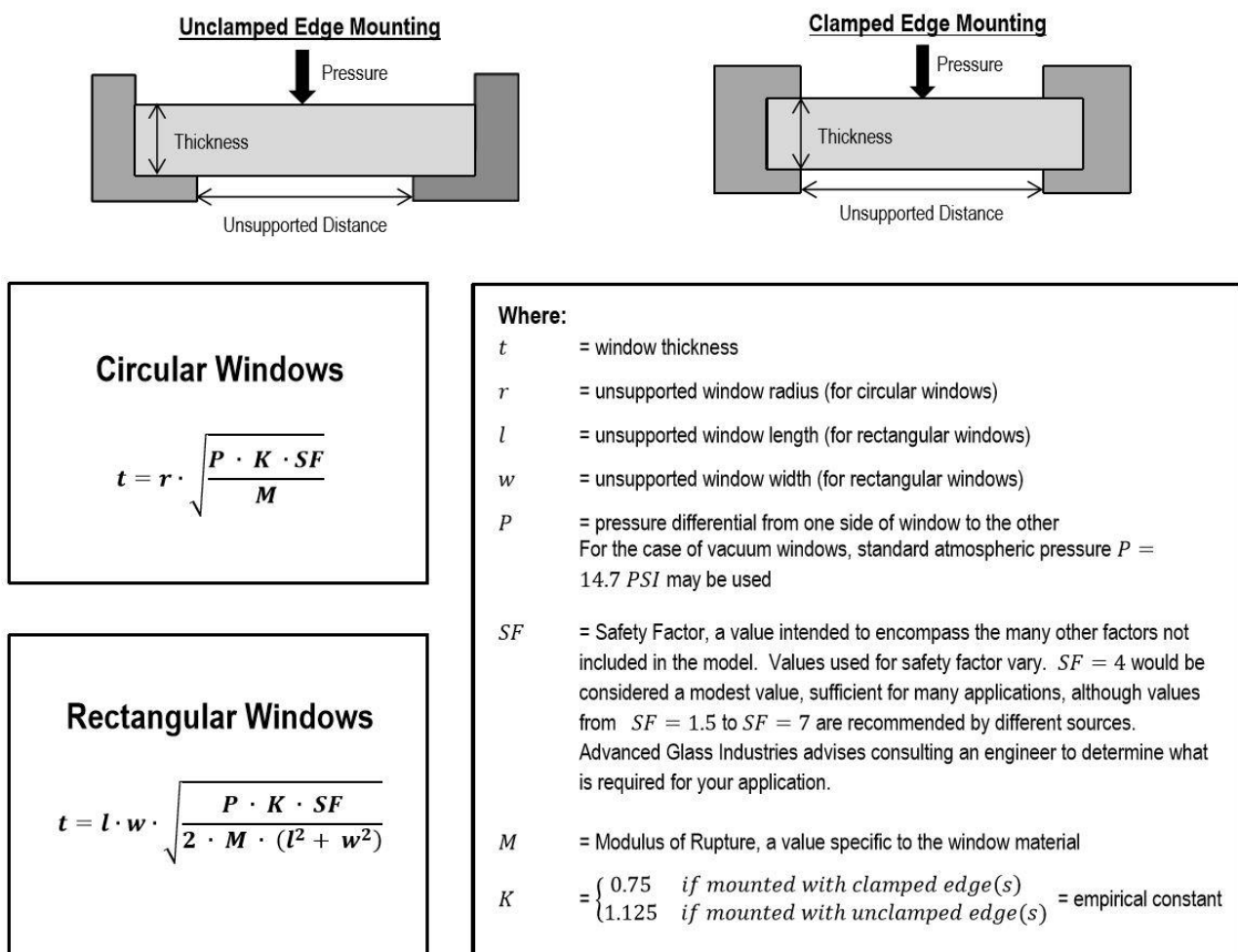

Unclamped Edge Mounting — Pressure — Thickness — Unsupported Distance

Clamped Edge Mounting — Pressure — Thickness — Unsupported Distance

Circular Windows

$$t = r \cdot \sqrt{\frac{P \cdot K \cdot SF}{M}}$$

Rectangular Windows

$$t = l \cdot w \cdot \sqrt{\frac{P \cdot K \cdot SF}{2 \cdot M \cdot (l^2 + w^2)}}$$

Where:

t = window thickness

r = unsupported window radius (for circular windows)

l = unsupported window length (for rectangular windows)

w = unsupported window width (for rectangular windows)

P = pressure differential from one side of window to the other
For the case of vacuum windows, standard atmospheric pressure $P = 14.7\ PSI$ may be used

SF = Safety Factor, a value intended to encompass the many other factors not included in the model. Values used for safety factor vary. $SF = 4$ would be considered a modest value, sufficient for many applications, although values from $SF = 1.5$ to $SF = 7$ are recommended by different sources. Advanced Glass Industries advises consulting an engineer to determine what is required for your application.

M = Modulus of Rupture, a value specific to the window material

K = $\begin{cases} 0.75 & if\ mounted\ with\ clamped\ edge(s) \\ 1.125 & if\ mounted\ with\ unclamped\ edge(s) \end{cases}$ = empirical constant

Figure 73: Formula for pressure windows design [32 to 35]

Of course, the thickness will depend on the dimensions of the windows, on the material (i.e. the modulus of rupture), on the type of constraint on the edges (e.g. clamped or unclamped edges) and of course on the pressure load. The apparent elastic limits of the materials that we have selected are in particular 45000 psi for the sapphire glass, 15000 psi for the Zinc Sulfide glass and 8000 psi for the silica glass and the zinc selenide glass. Notice the enormous difference between the sapphire glass and the other types: as we were expecting the sapphire glass has a biggest elastic limit.

We tried different type of windows disposition and dimensions but, in the end, the most appropriate choice turned out to have a circular window of 6 inches for laser application (and for using the already existing IR window), and a rectangular bigger window for a sapphire glass, which allows measurements in the V range.

Our first guess was therefore to design a big rectangular window of 15 x 10 inches and a circular one of 6 inches in diameter, as in Figure 74. An important design choice here and later is to design an asymmetric window in such a way that we can change the orientation of the flange to change the point of view.
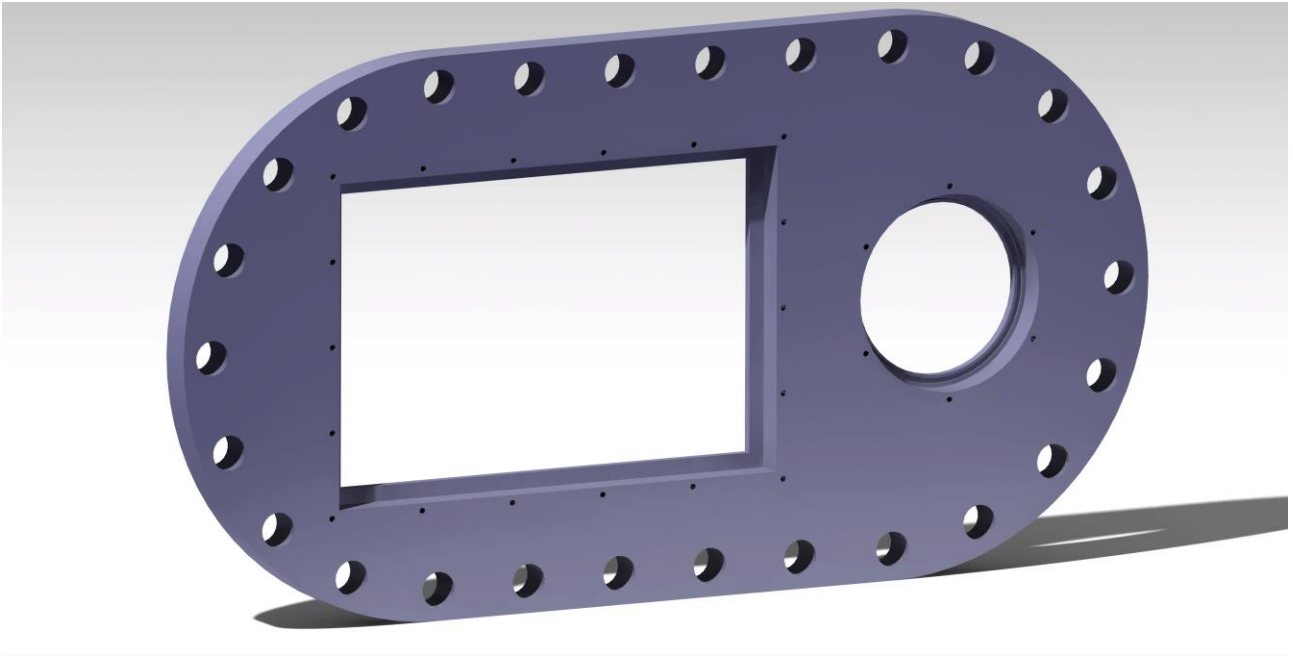

Figure 74: First guess for the window design (3D CATIA rendering), rectangular space for the sapphire glass and circular one for the laser one

To calculate the required dimension, we have calculated the required thickness for the selected glass using the formulas in Figure 73. We have used a safety factor of 4 and a pressure load of 14.7 psi (i.e. atmospheric pressure), and it turns out that we need a thickness of 5.73 mm for the sapphire glass and a thickness of 6.829 mm for the laser glass. A further improvement of our design is presented in Figure 75 in which we introduce some adapters to install larger and smaller windows.
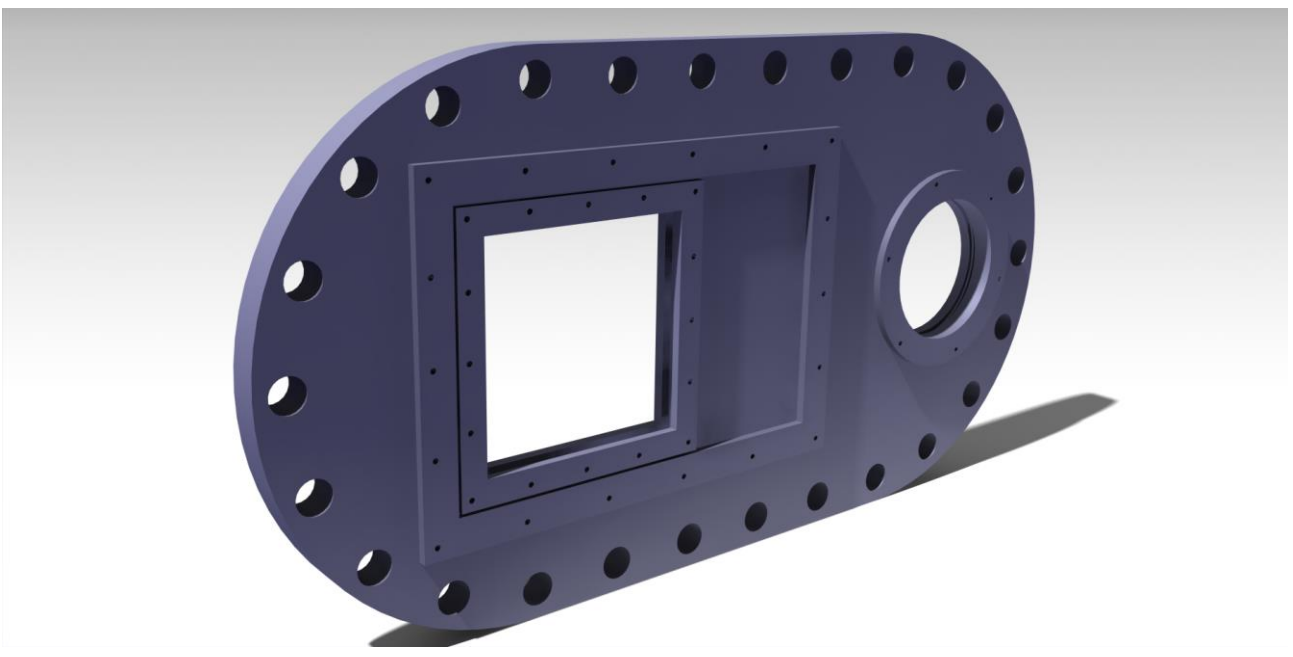

Figure 75: Second guess for the window design (3D CATIA rendering), rectangular space for the sapphire glass, circular one for the laser one and square one for a third possible choice

With this new guess we can install a rectangular window of 15 x 10 inches, a square window of 8 x 8 inches and a circular Window of 6 inches of diameter (see Figure 76). Moreover, following our initial asymmetric purpose we may have two orientations for the square window and also two thicknesses for the circular in order to install the laser window or the IR window (which has a different thickness).
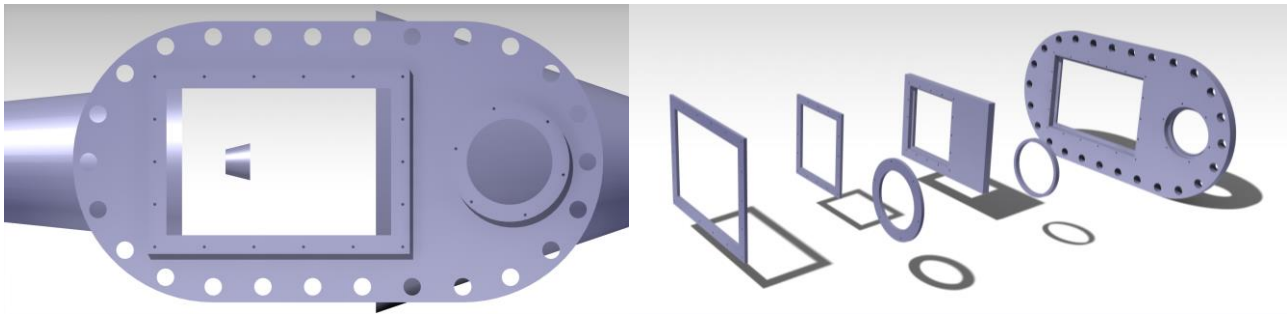

Figure 76: View of the test chamber from the large window (left) and exploded view of the flange window assembly

At the end, the thickness and hence the optical density (equation 37) are in good agreement with the requirements for our applications but the companies that we have contacted had some difficulties in producing this large sapphire window of 15 x 10 inches.

What we did therefore was to design a new proposal with only the circular and the square windows because an 8 inches window is enough to guarantee a perfect view of the test chamber (see Figure 77).
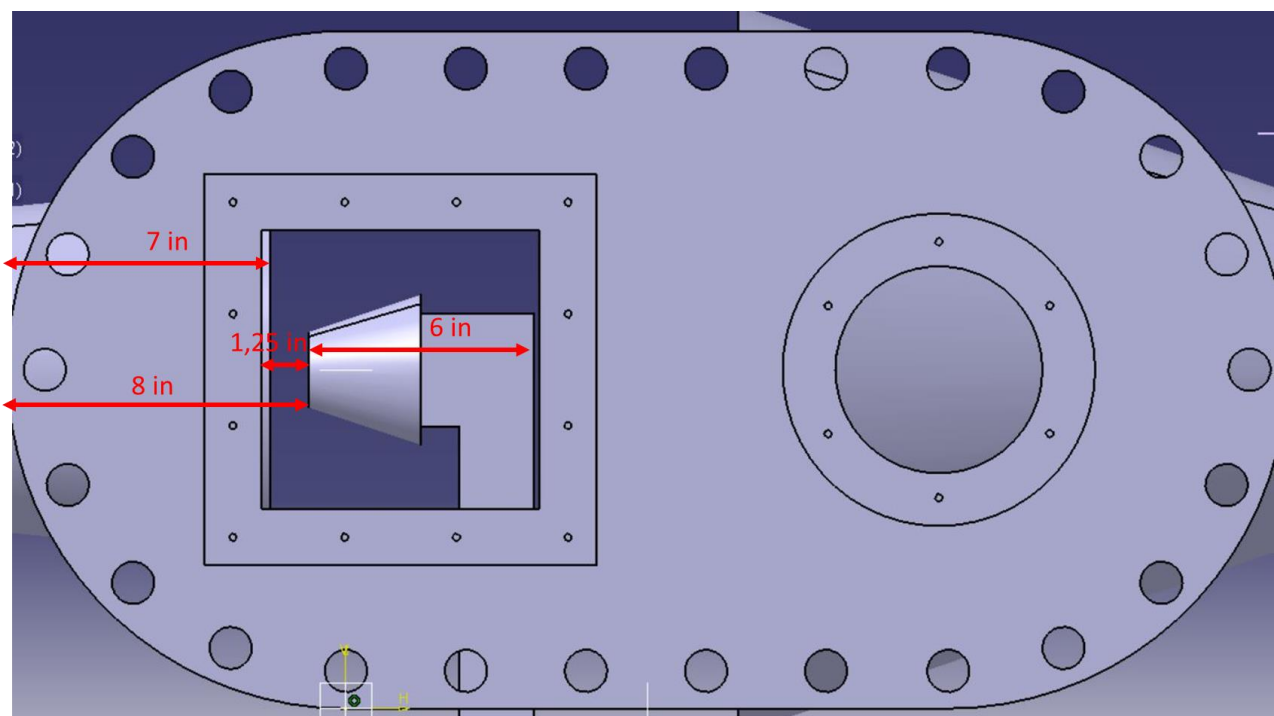

Figure 77: Final Window design proposal with important dimensions, square and circular glasses

In the following Figure 78 and 79 we present the 3D CATIA renderings for the final window design proposal which, as we said, includes a square window for the sapphire glass (UV – V measurements) and a circular window for the laser and IR measurements. Since for doing the last two measurements we need two types of glasses we have designed an adapter to increment the thickness of the laser glass (which is thinner if compare to the IR glass). Notice that the two glasses are properly positioned in order to allow a direct view on the model when we change the orientation of the flange.
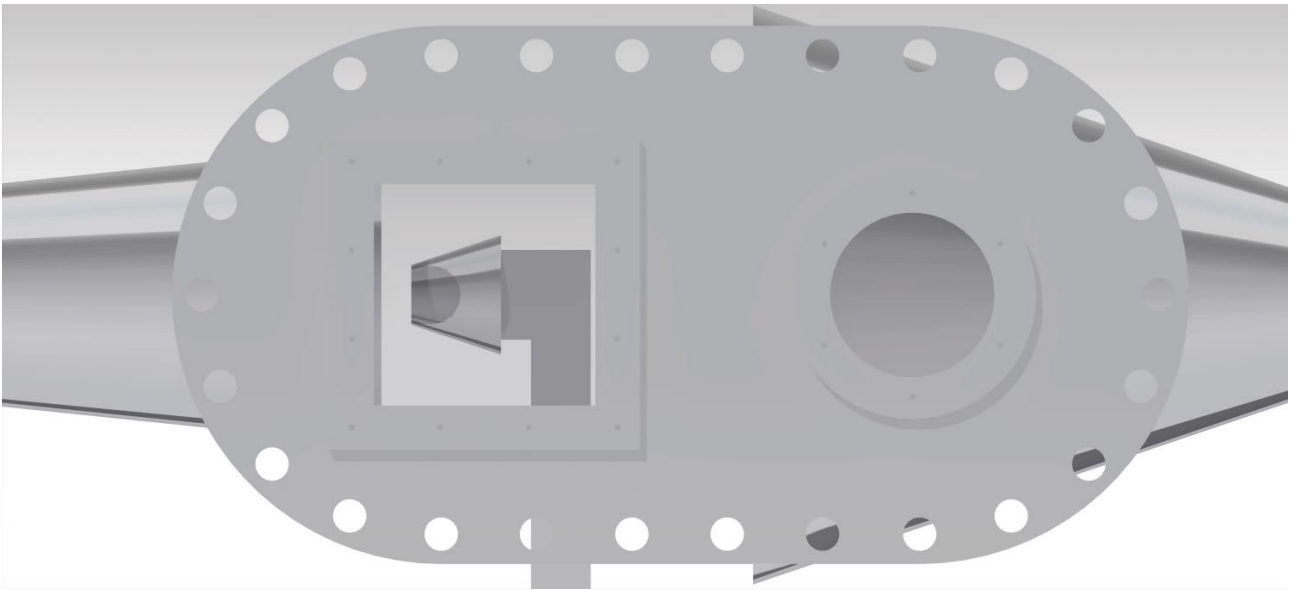
Figure 78: Final window flange design proposal, view of the test chamber from the square window
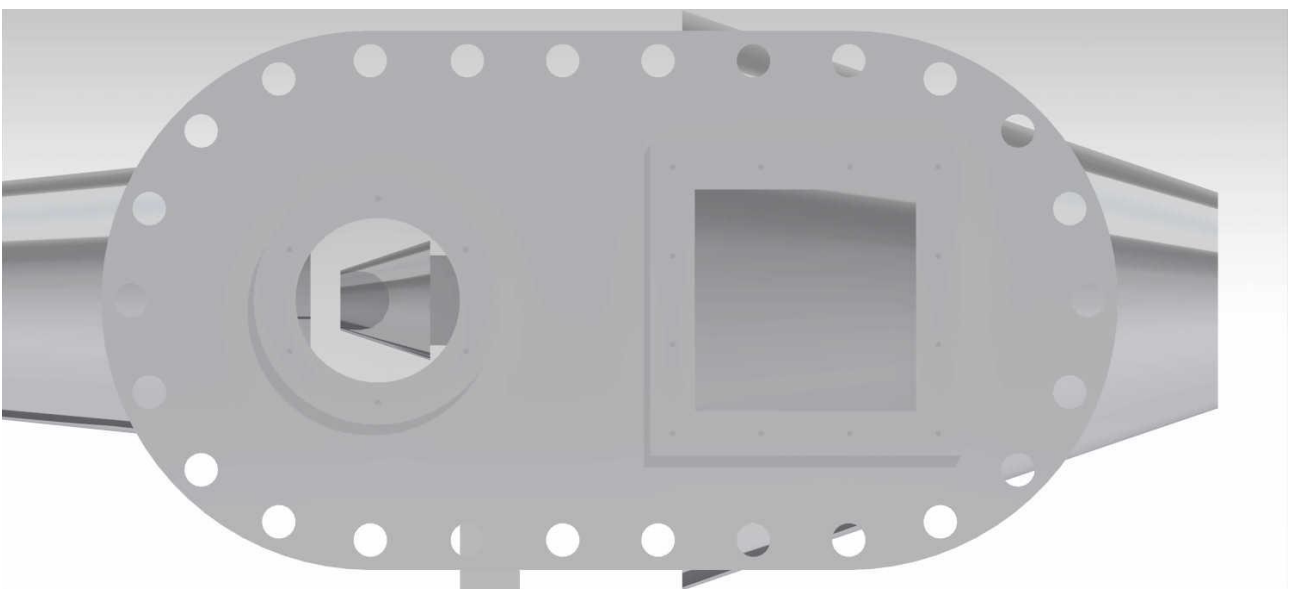

Figure 79: Final window flange design proposal, view of the test chamber from the circular window

4.4.   FEM Analysis

The last step is to make sure that our design proposal can withstand the pressure loads. For what regarding the glasses we have already calculated their thickness such that they can withstand the atmospheric pressure load. Now we have to assure that the metallic flange (6061 T6) can sustain this load without being deflected too much, since a large deflection of the metallic flange will introduce high stresses inside the glasses.

As we have done in the case of the flange for water injection, we have used the CATIA V5R20 software for the FEM analysis of the window flange. The first point is to define the constraints and the loads acting on the material. For what regarding the constraints, as in Figure 80, we have that the main holes faces are fixed (not

allowed to rotate or move). The loads that we considered are due to the pressure atmospheric load of 10^5 Pa (see Figure 81).
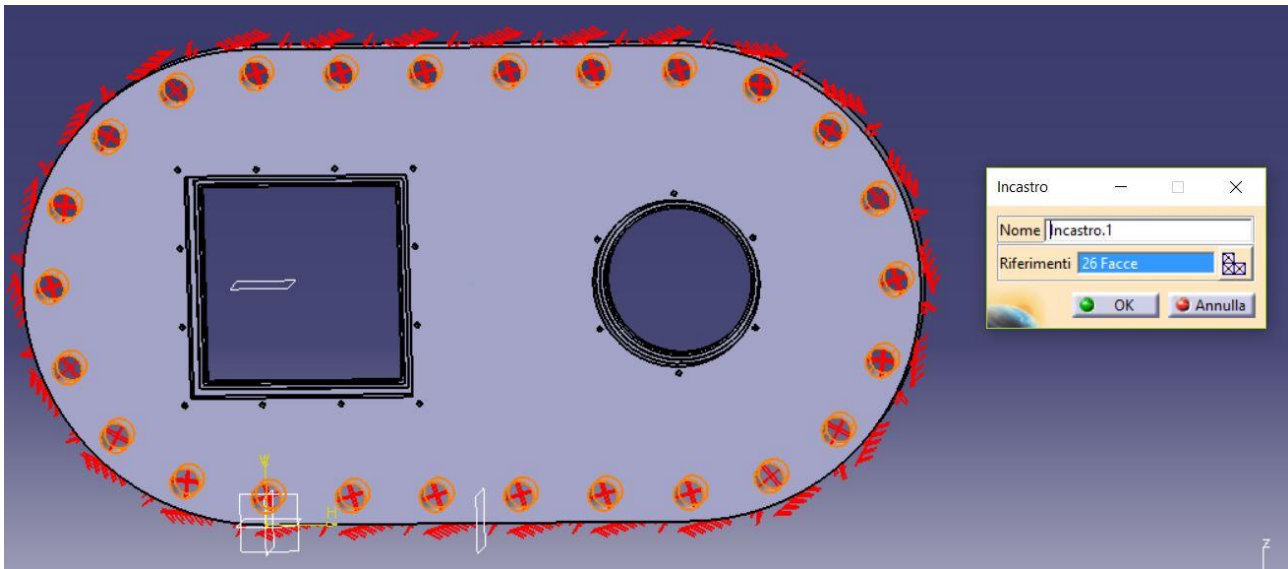

Figure 80: Constraints for the FEM analysis of the window, main holes faces are fixed (not allowed to rotate or move)
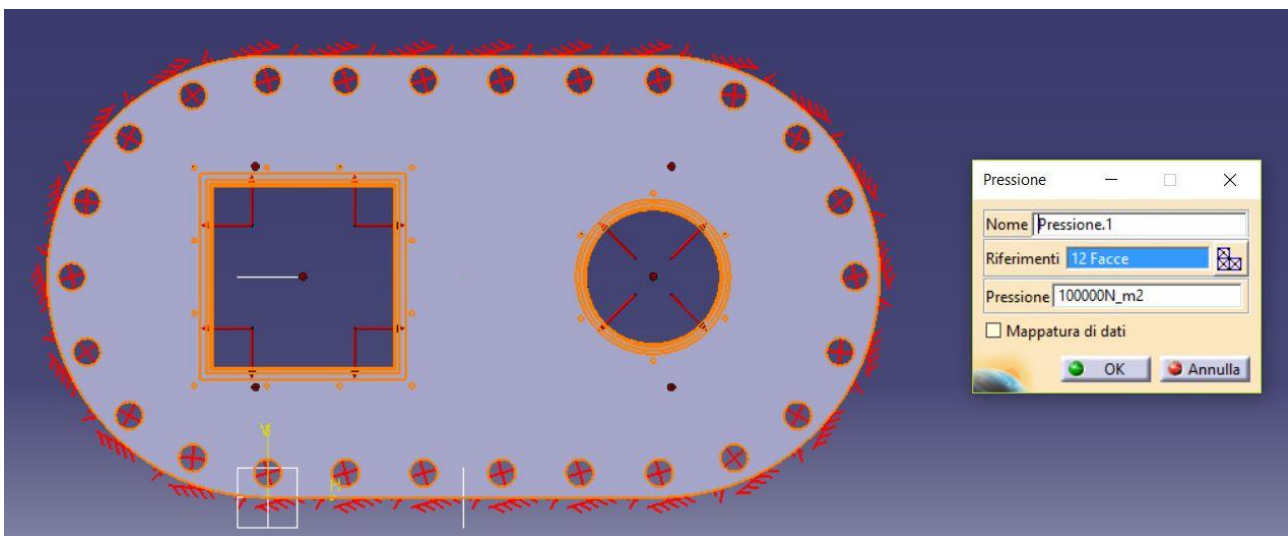

Figure 81: Loads for the FEM analysis of the window, pressure load of 10^5 Pa on the external faces of the flange

Once we have set up the analysis model we have to check if the results that we obtain are independent from the mesh. We started from a coarse mesh to a fine mesh until independence was achieved. The results in terms of maximum displacement and stress, for the finest mesh, are showed in Table 9.

Mesh	Dimension of cells	Number of cells	Max. displacement	Max. stress
Fine mesh	0.08 in	2635734	0.00144 in	14.1 MPa

Table 9: Results of the FEM analysis of the window for fine mesh

We present the fine mesh that we have used in Figure 82 while, in Figure 83 we present the results in terms of maximum stresses inside the aluminum flange. The maximum stress of course is well below the maximum allowable stress since the atmospheric pressure is not a critical load for a thick metal plate.
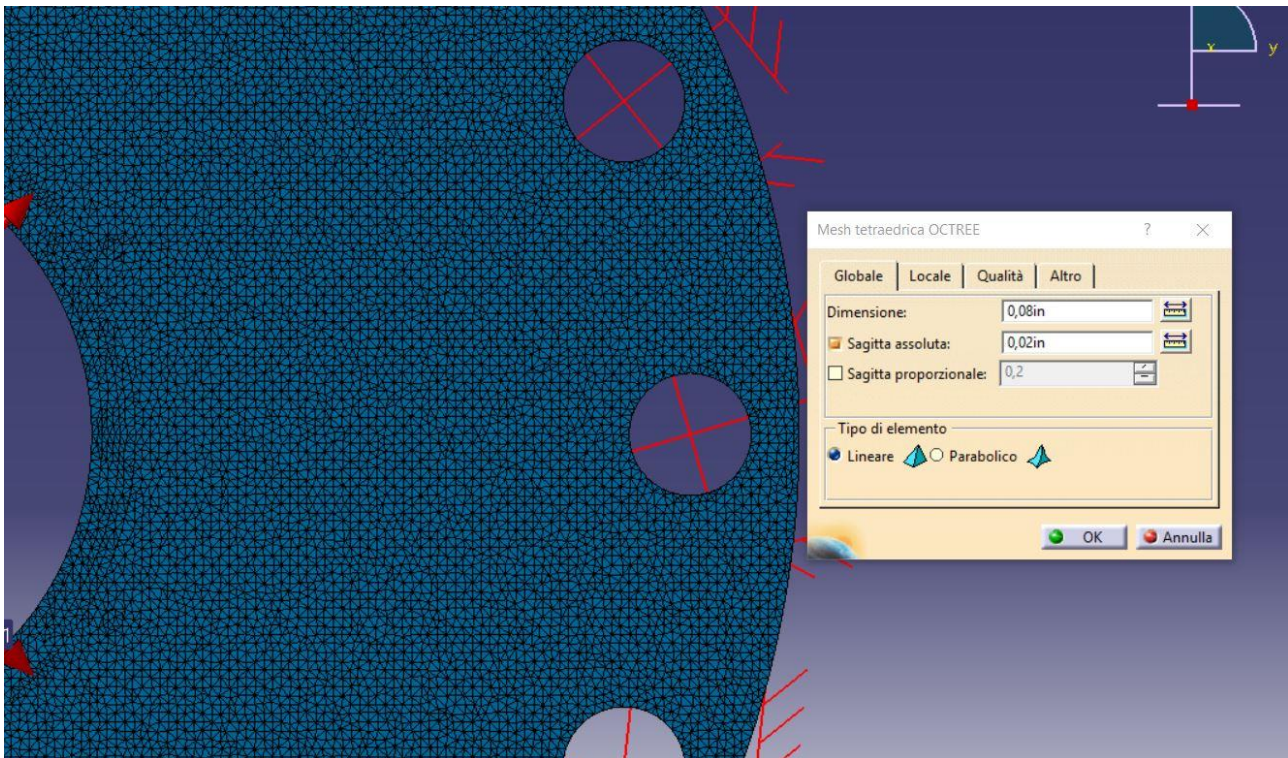
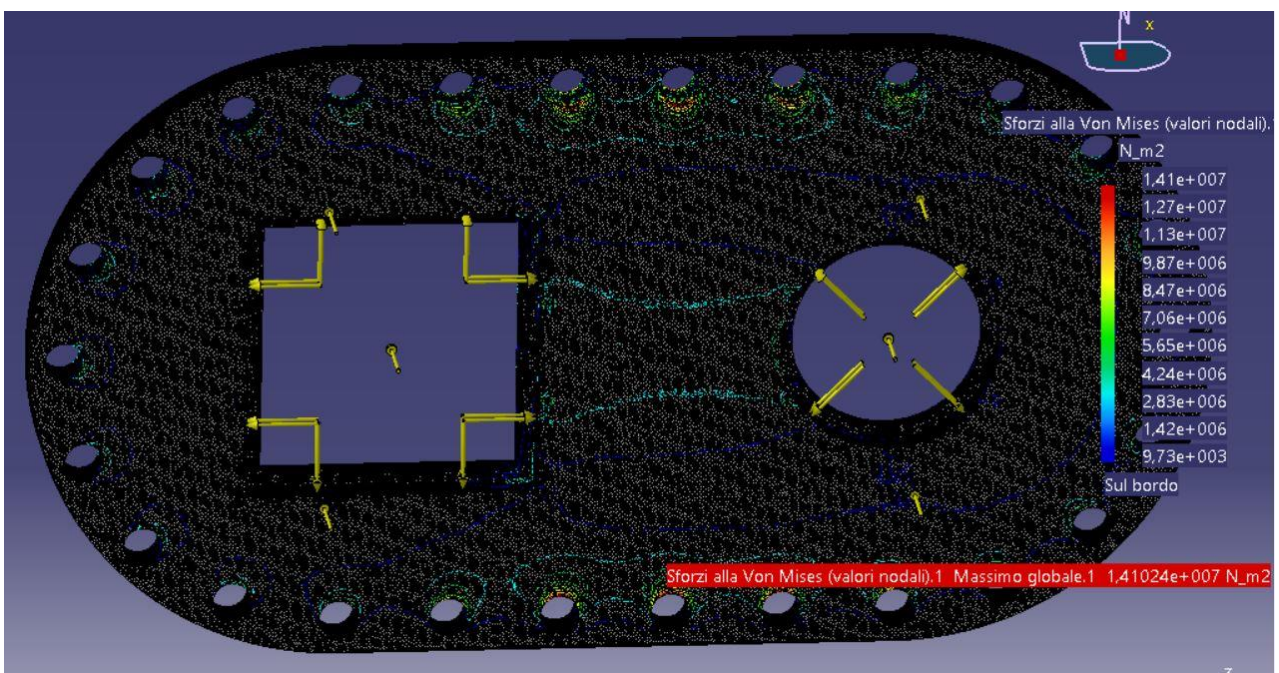*Figure 82: FEM analysis of the window, fine mesh*

Figure 83: FEM analysis of the window, Von Mises stresses, fine mesh

The problem could be the maximum displacement since it will induce large stresses inside the glasses. We present the results for the maximum displacement in Figure 84. The maximum displacement happens, as we expected, almost at the middle of the plate, nearer to the square window since we have a larger aperture with respect to the circular window. Anyway, the maximum displacement of 0.00144 inches (i.e. 0.036 mm) appears to be a reasonable value for the deflection.
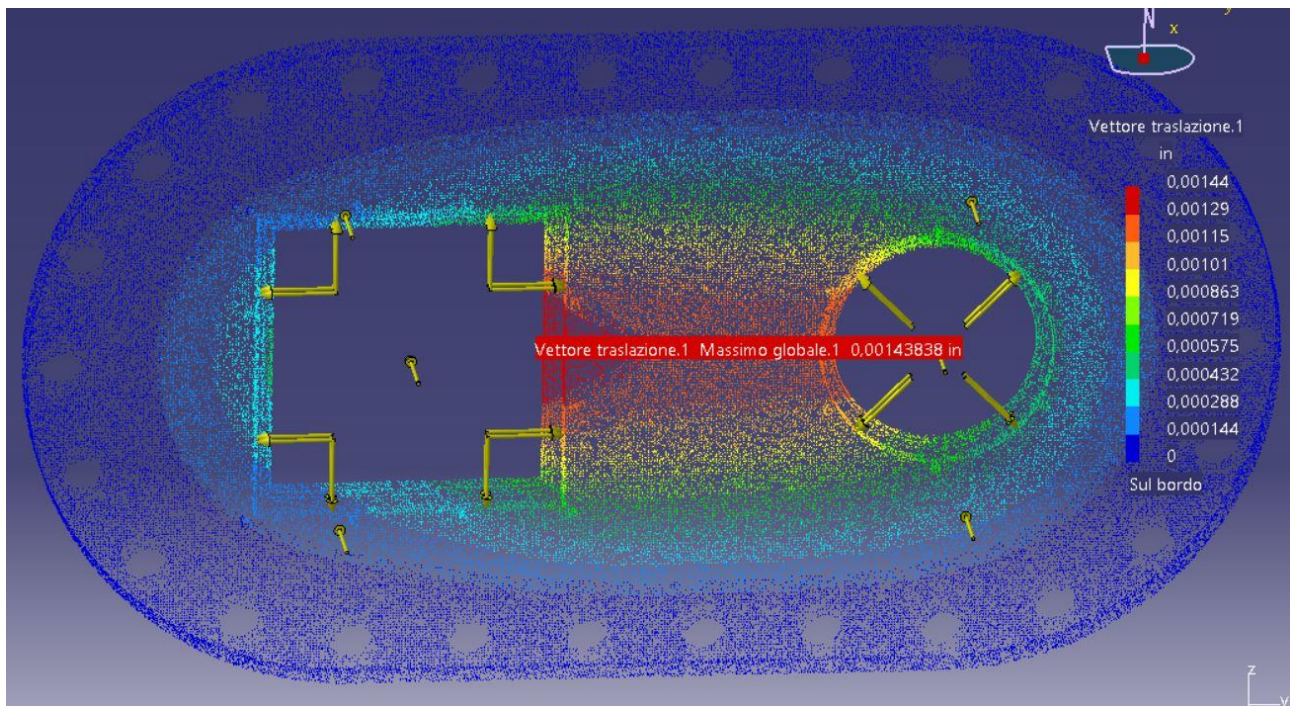
Figure 84: FEM analysis of the window, magnitude of the displacements, fine mesh

At the end our design proposal appears to be properly designed in terms of shape, orientation and dimensions of the square and circular windows: they allow to have a good view on the test chamber and on the model. The FEM analysis show how the aluminum plate is properly designed in order to withstand the pressure loads and to do not deflect too much in order to behave as perfect support for the glasses. However future analysis of the whole assembly, including the glasses, should be done to check the behavior of the glass in order to ultimate control that the assembly will withstand the loads.

Conclusions

During the internship at the Aerodynamics Research Center of The University of Texas at Arlington I was involved in three main topics, namely the studying and the application of the Filtered Rayleigh Scattering tool, the design of an emergency flange and the design of the test chamber windows for the new 1.6 MW Plasma Wind Tunnel facility under construction.

After the initial literature review of the Filtered Rayleigh Scattering tool and the studying of the LabView operation for the control of the facilities, I have been involved in the preparation and execution of the experiments for the studying of the mixing of the vortices downstream a scramjet injector. After the successfully execution of the experiments at two sections downstream the injector (i.e. 13h and 20h), I was involved in the postprocessing of the obtained data. In total we get a hundred of good photographs for both Helium and Air injection and from the comparison between the two converged averaged images we could get information about the molar fraction of the Helium. At the end it turned out that the experiments were properly executed, and the vortices structure is clearly visible from the obtained images.

The other task that I had was to design an emergency flange for the new Hypersonic Plasma Wind Tunnel to be placed after the diffuser and before the heat exchanger. In practice, if it happens that the heat exchanger does not work properly we want to lower the temperature of the flow before it reaches the delicate and expensive vacuum system. Our design proposal for the flange allows to inject the right quantity of cold water in order to mix it with the flow and lower in such a way its temperature. At the end of our design it turned out that that the design of the pipes is correct in terms of dimensions and that also the injection of water is properly accomplished by the injection nozzles thanks to their well-defined position, orientation, dimensions and shape. Moreover, the proposed flange can largely sustain the pressure loads due to the atmospheric pressure and due to the high pressurized water flow for the regular cooling systems.

The last objective that has been achieved is the design of the test chamber windows for the same hypersonic facility. A careful selection of the optical material is carried out in order to allow different kind of measurements (from ultraviolet to infrared and laser) in a very challenging environment due to the high mechanical stress and the chemical corrosive environment. At the end, our proposal appears to be properly designed in terms of shape, orientation and dimensions of the square and circular windows: they allow to have a perfect view on the test chamber and on the model. The FEM analysis show how the aluminum plate is properly designed in order to withstand the pressure loads and to do not deflect too much in order to behave as perfect support for the glasses.

In conclusion, we can assert that all the three tasks that I had during my internship at the University of Texas at Arlington were successfully accomplished: experiments using the Filtered Rayleigh Scattering were properly carried out and gave very good results, while the proposed design for the emergency flange and the test chamber windows demonstrated to be valid and capable to meet all the given requirements.

References

[1]   Aerodynamics Research Center: facilities.

[2]   UT Arlington: first university-based, large-scale, arc-heated hypersonic-testing facility.

[3]   Aerodynamics Research Center: Supersonic Wind Tunnel.

[4]   Aerodynamics Research Center: Equipment.

[5]   Ground, Cody, Dhananda Thumiah, and Luca Maddalena. "Design and application of filtered Rayleigh scattering experiments for mixing studies of new strut injectors for scramjets." *31st AIAA Aerodynamic Measurement Technology and Ground Testing Conference, Dallas, Texas, AIAA*. Vol. 2567. 2015.

[6]   Miles, Richard B., Walter R. Lempert, and Joseph N. Forkey. "Laser rayleigh scattering." *Measurement Science and Technology* 12.5 (2001): R33.

[7]   Boguszko, M., and G. S. Elliott. "Property measurement utilizing atomic/molecular filter-based diagnostics." *Progress in Aerospace Sciences* 41.2 (2005): 93-142.

[8]   Seasholtz, Richard G., and Alvin E. Buggele. *Study of injection of helium into supersonic air flow using Rayleigh scattering*. Vol. 107409. National Aeronautics and Space Administration, Lewis Research Center, 1997.

[9]   Adrian, Ronald J., and Jerry Westerweel. *Particle image velocimetry*. No. 30. Cambridge University Press, 2011.

[10] Kato, Satoru, et al. "Laser doppler velocimeter." U.S. Patent No. 5,587,785. 24 Dec. 1996.

[11] Heisenberg, Werner. *The physical principles of the quantum theory*. Courier Corporation, 1949.

[12] Hulst, Hendrik Christoffel, and Hendrik C. van de Hulst. *Light scattering by small particles*. Courier Corporation, 1957.

[13] Sutherland, William. "LII. The viscosity of gases and molecular force." *The London, Edinburgh, and Dublin Philosophical Magazine and Journal of Science* 36.223 (1893): 507-531.

[14] LabView tutorials

[15] Type T Thermocouple

[16] NI – USB 6009

[17] Omega PX603 Transducer

[18] Liquid Rocket Engine Injectors, SP-8089, NASA, 1976

[19] Brune, Andrew J., et al. "Numerical Analysis of an Actively-Cooled Low-Reynolds Number Hypersonic Diffuser." *21st AIAA International Space Planes and Hypersonics Technologies Conference*. 2017.

[20] NASA Chemical Equilibrium with Applications

[21] Steam characteristics

[22] Atomization process

[23] Water data page

[24] Van Foreest, Arnold, et al. "Transpiration cooling using liquid water." *Journal of Thermophysics and Heat Transfer* 23.4 (2009): 693.

[25] Anderson, John David. *Hypersonic and high temperature gas dynamics*. Aiaa, 2000.

[26] Tambe, Samir B., et al. "Liquid jets in subsonic crossflow." *AIAA paper* 731 (2005): 2005.

[27] Liu, Haixu, Yincheng Guo, and Wenyi Lin. "Numerical simulations of transverse liquid jet to a supersonic crossflow using a pure two-fluid model." *Advances in Mechanical Engineering* 8.1 (2016): 1687814016629341

[28] Fuller, Raymond P., et al. "Effects of Injection Angle on Atomization of Liquid Jets in Transverse Air Flow." *AIAA journal* 38.1 (2000).

[29] Baranovsky, S. I., and J. A. Schetz. "Effect of injection angle on liquid injection in supersonic flow." AIAA Journal 18.6 (1980): 625-629.

[30] Dassault systems products: CATIA V5R20

[31] Weber, Marvin J. *Handbook of optical materials*. Vol. 19. CRC press, 2002.

[32] Design rules for vacuum chambers (CERN)

[33] Ispoptics: design pressure windows

[34] Advancedglass: design pressure windows

[35] Crystran: design pressure windows